ABSTRACT

Title of Dissertation: Electrostatic Gas-Liquid Separation from High Speed Streams—Application to Advanced On-Line/On-Demand Separation Techniques

Mohamed Alshehhi, Doctor of Philosophy, 2009

Dissertation Directed By: Professor Michael Ohadi
Department of Mechanical Engineering

The separation of suspended droplets from gases has been one of the basic scientific and technical problems of the industrial era and this interest continues. Various industrial applications, such as refrigeration and HVAC systems, require control of fine droplets concentrations in moving gaseous mediums to maintain system functionality and efficiency. Separating of such fine droplets can be achieved using electrostatic charging as implemented in electrostatic precipitators (ESPs). They use electrostatic force to charge and collect solid particles.

The objective of the present work was to study the feasibility of using wire-tube electrostatic separator on the removal of fine water and oil droplets from air stream based on corona discharge ionization process. A parametric study was conducted to find key parameters affecting the separation process. This goal was approached by simulating the charging and separation phenomena numerically, and then verifying the modeling findings through experiments.

The numerical methodology simulated the highly complex interaction between droplets suspended in the flow and electrical field. Two test rigs were constructed, one for air-water separation and the other for air-oil separation. A wire-tube electrostatic separator was used as the test section for both test rigs. The separation performance was evaluated under different electric field and flow conditions. Finally, based on the results, a novel air-water separator prototype was designed, fabricated and tested.

The numerical modeling results qualitatively showed acceptable agreement with the experimental data in terms of the trend of grade efficiency based on droplets size. Both numerical modeling results and experimental data showed that with a proper separator design, high separation efficiency is achievable for water and oil droplets. Based on the experimental data, at flow velocity of 5 m/s and applied voltage of 7.0 kV, the maximum separation efficiency for water and oil was 99.999 % and 96.267 %, respectively. The pressure drop was as low as 100 Pa and maximum power consumption was 12.0 W.

ELECTROSTATIC GAS-LIQUID SEPARATION FROM HIGH SPEED STREAMS—APPLICATION TO ADVANCED ON-LINE/ON-DEMAND SEPARATION TECHNIQUES

By

Mohamed Alshehhi

Dissertation submitted to the Faculty of the Graduate School of the
University of Maryland, College Park, in partial fulfillment
of the requirements for the degree of
Doctor of Philosophy
2009

Advisory Committee:

Professor Michael Ohadi, Chair
Research Professor Serguei Dessiatoun
Professor Marino di Marzo
Professor Gregory Jackson
Professor Gary A. Pertmer
Associate Professor Bao Yang

DEDICATION

To my country, United Arab Emirates.

To my parents, my wife and my children for their sacrifices, support and unconditional love.

ACKNOWLEDGEMENTS

First and foremost, I would like to thank my advisor and mentor Dr. Michael Ohadi for his dedication, intellectual guidance, support, advices and also for bringing the best out of me which helped making this successful work.

I would like to thank my parents, my wife and my children for their unconditional love and support during the long, difficult, challenging and hard working years of my Ph.D. program.

I would like to thank Dr. Serguei Dessiatoun and Dr. Amir Shoushtari for their unlimited help and support throughout the course of this research project. Without them, this project would have never reached its final phase.

Throughout my years of study in the United States I made good friendship with Dr. Ebrahim Al-Hajri who I consider as brother. I value his friendship and appreciate his help and support to me during my study in the United States.

I am grateful to my many friends and colleagues at the Smart and Small Thermal Systems Laboratory for providing a stimulating, constructive and fun-filled environment to learn and grow. I am especially thankful to Vytenis Benetis, Sourav Chowdhury, Parisa Foroughi, Guohua Kuang, Arman Molki, Jianlin Wu, Lewis Gershen, Timothy McMillin, Thomas Baummer, Edvin Cetegen, Elnaz Kermani, Ratnesh Tiwari, and Paul Kalinowski.

Last but not least, I wish to express my deepest appreciation and thanks to Abu Dhabi National Oil Company (ADNOC) and the Petroleum Institute in (PI) in Abu Dhabi, UAE for their financial support to my education and to this project.

TABLE OF CONTENTS

LIST OF TABLES

LIST OF FIGURES

NOMENCLATURE

A	Area (m^2)
A_0	Any closed area that encloses emitter or collector electrodes (m^2)
C_1, C_2	Integration constants
C_c	Cunningham correction factor
C_D	Drag coefficient
$\overline{C}_i$	Ion mean thermal speed (m/s)
d_p	Particle diameter (m)
d_t	Tube diameter (m)
d_w	Wire diameter (m)
E	Electric field strength, or electric field intensity (V/m)
E_0	Initial electric field strength at emitter (V/m)
E_c^0	Critical field strength (V/m)
E_L	Limit field strength at particle surface (V/m)
e	Absolute value of electric charge, 1.6×10^{-19} (C)
F_D	Drag term (s^{-1})
$\mathbf{F}_e$	Electrostatic body force (N/m^2)
$\mathbf{F}_{EHD}$	Electrohydrodynamic body force (N/m^2)
g	Acceleration due gravity (m/s^2)
I	Current (A)
J	Current density (A/m^2)
k	Boltzmann constant, $1.3806503 \times 10^{-23}$ ($m^2/kg.s^2.K$)

K_E	Proportionality constant, 9.0×10^9 ($N.m^2/C^2$)
L	Separator length (m)
n	Number of Charge
n	Local unit vector normal to the surface
P_f	Pressure (Pa)
P_0	Atmospheric pressure (Pa)
q	Charge (C)
Q	Flow rate (m^3/s)
q_{diff}	Charge on a particle due to diffusion charging (C)
q_f	Free surface charge (C)
q_{fld}	Charge on a particle due to field charging (C)
$q_{fld,sat}$	Saturation charge on a particle due to field charging (C)
q_i	Induced Charge (C)
q_L	Limit charge on a solid particle (C)
q_p	Charge on a particle due to diffusion and field charging (C)
q_R	Limit charge on a droplet due to Rayleigh limit (C)
r	Displacement in radial direction (m)
Re	Reynolds number
Re_p	Relative Reynolds number
T_f	Fluid temperature (K)
T_0	Ambient temperature (K)
t	Particle resident time (s)
$\mathbf{u}_f$	Fluid velocity (m/s)

$\mathbf{u}_p$	Particle velocity (m/s)
Z_i	Ion mobility ($m^2/(V.s)$

Greek Letters

β	Electric permittivity ($C^2/N.m^2$)
β_0	Electric permittivity of a vacuum, 8.85×10^{-12} ($C^2/N.m^2$)
γ	Surface tension of a particle (N/m)
δ	Relative density
ε	Relative permittivity or dielectric constant
ε_p	Relative permittivity of a particle
ε_s	Relative permittivity of space
η	Total separation efficiency
η_G	Grade or fractional efficiency
λ	Molecular mean free path (m)
μ_f	Fluid dynamic viscosity ($N.s/m^2$)
μ_p	Particle dynamic viscosity ($N.s/m^2$)
ρ_f	Fluid density (kg/m^3)
ρ_i	Charge density of space (C/m^3)
$\rho_{i,e}$	Charge density at emitter (C/m^3)
ρ_p	Particle density (kg/m^3)
σ	Resulting aspect ratio
σ_i	Electric conductivity (S/m)
ϕ	Applied electric potential or voltage (V)

ϕ_0 Corona onset voltage (V)

ϕ_e Applied electric potential at emitter (V)

CHAPTER 1: INTRODUCTION

1.1. Background and Motivation

The separation of suspended fine liquid droplets from gas flows is of interest to many industrial applications and fields (White 1963). Some of these applications are the separation of oil droplets from refrigerant as in HVAC and refrigeration systems and the separation of water droplets from airflow as in aerospace applications. Other major applications that require separation processes include health and environmental safety area in the separation of radioactive aerosols from air and gas-liquid droplet separation in flare knock-out drums.

The failure of not separating the droplets from gas flows can affect the system's functionality and performance. For example, oil that leaks as fine droplets from compressors to gas flows in refrigeration system decreases functional efficiency. Heat exchangers cooling capacity will be lower and the systems pressure drop will be high once the contaminant gas flows through the system (Yun, et al. 2007).

Separation of sub micron liquid droplets from gas flows with conventional technologies and with high separation efficiency is very difficult and in most cases nearly impossible. Complete capture and removal of fine particles with conventional technologies such as cyclone and coalescence based separators is not possible. The droplets diameters usually are within the micron and submicron size (Temprite, Inc. 2007). Therefore, the existing technologies are often ineffective on separating such fine suspended liquid droplets from the gas flows.

This present work investigates the feasibility of using electrostatic force to remove fine droplets from an air flow. Two liquids were used in this study as droplets material, water and oil (synthetic lubricant). For all studies, droplets of only one liquid were injected and no mixture of oil and water droplets was studied. Water has high relative permittivity of 80 where oil relative permittivity is lower (2.0).

The work conducted in the current study included numerical modeling of the electrostatic separation and parametric studies to identify the role of key operational controlling parameters. This study highlighted the effect of applied voltage, flow velocity, flow temperature and separator length on the separation performance. Next, two test rigs were constructed to conduct a parametric study on the water and oil, so that the results can be compared against the modeling predictions. The test section in both test setups was the wire-tube separator. Finally, to address the application of the presented methodology in aerospace applications, a first generation air-water separator prototype was manufactured and tested under different water concentrations, representing typical conditions encountered in aerospace applications.

1.2. Dissertation Outline

This dissertation is divided into eight chapters. Chapter 2 reviews the fundamentals of ionization process based on corona discharge. Next it presents the operation mechanism of the electrostatic charging and collection of particles in an airflow, followed by highlighting the main governing equations representing the electrostatic charging process.

In Chapter 3, the existing technologies for droplet separation from gas flows were reviewed. Next, few experimental works that involve electrostatic separation of

liquid droplets are presented. Finally, literature review of numerical and analytical studies on the separation process are outlined.

Chapter 4 covers the numerical modeling study. It outlines the basic model assumptions, boundary conditions, numerical method and results for wire-tube electrostatic separator, with water as droplet material in this case. The model simulates how many droplets are captured out of the injected ones when selected parameters are changed.

Chapter 5 and Chapter 6 introduce the experimental rigs for water and oil (synthetic lubricant) separation, respectively. The test rigs were built to test the separation performance for water and oil from an airflow. The test section used for both rigs is the wire-tube separator. Test equipments, instruments and measurements devices are presented along with their features and calibration curves. Testing procedures are also outlined in detail. The performance of the separator is evaluated based on droplets concentration measured at the outlet out of the inlet concentration. At each studied case one of the varied parameters is changed.

Chapter 7 is dedicated to the first generation air-water separator design, fabrication and testing, with features specifically designed to address a typical aerospace separation unit for environmental control system applications. The separator was designed based on wire-tube geometry. Seven perforated tubes were used in the design. A porous media was used to enhance the drainage of collected water. The same air-water separation test rig in Chapter 5 was used for the first generation testing in Chapter 7.

Finally, Chapter 8 draws conclusions, summarizes the key findings, and proposes future research directions.

CHAPTER 2: FUNDAMENTALS OF ELECTROSTATIC PARTICLE CHARGING AND SEPARATION BASED ON CORONA DISCHARGE

This chapter discusses the fundamentals behind the electrostatic forces that cause corona discharge, and it highlights some parameters that affect corona discharge. Next, the chapter will review the physics behind the particle charging mechanism and the behavior of particles under an applied electrostatic field. Also, the mechanism of particle collection will be reviewed. Finally, the momentum balance equation of a particle in flow field and under an applied electrostatic force will be shown along with its non-dimensional form.

2.1. Concept and Basic Definitions

When an electrostatic field is applied between two points it can have an effect on the surrounding medium, whether gas or liquid. This phenomenon is studied as part of the field of electrohydrodynamics (EHD) (also known as electro-fluid-dynamics (EFD) and electrokinetics), which studies the motions of ionized particles or molecules in dielectric fields caused by their interactions with electric fields and surrounding fluid (Wikipedia 2008). The EHD phenomenon can be useful in many applications, including electrostatic fluid accelerators (ionic pumping) for heat transfer applications, electro-spraying, and electro-coating.

An electrostatic field can also have a significant charging effect on particles existing in the medium, such as solid or liquid particles in gases. The resultant

electrostatic force between the two points is fundamentally explained by Coulomb's law. This particle charging effect has been used widely in the separation of solid particles in electrostatic precipitators (ESPs). This review will highlight the fundamentals of the electrostatic forces that charge moving particles in gas flow due to corona discharge. Before proceeding to the governing equations, however, the basic operating process of the corona discharge phenomenon will be reviewed.

2.1.1. Corona Discharge

The main objective for utilization of corona discharge (or ionic wind) is as a means to ionize gas molecules. Although ions can be created in gas using other means, such as radioactive discharge, ultraviolet radiation, and flames, corona discharge has proved to be a technologically feasible and economically competitive way to perform this basic function (White 1963). Corona discharge in gases is produced when the electric field strength (**E**), also known as electric field intensity, overcomes the maximum limit that the gas can sustain, creating a uniform or non-uniform electric field. This electric field can be achieved in a gas between two electrodes when there are high potential gradients and one of the electrodes has a much smaller radius or curvature than the other one, making it a sharp object. Equation (2-1) shows the relation between applied electric potential, or voltage, (ϕ_e) and electric field strength.

$$\mathbf{E} = -\nabla \phi_e \qquad \textbf{(2-1)}$$

The classic geometries for creating corona discharge are the potential gradients between a concentric wire of small radius and a tube, and between a needle

and a plate, which were first tried by Gaugain (1862) and Nahrwold (1878), respectively. Usually, the needle and wire are charged and are referred to as the "emitter electrode," whereas the plate or tube is grounded and is referred to as the "collector electrode."

Much work has been published to explain the physics of corona discharge, such as the work of Hohlfeld (1824), Peek (1929) and Loeb (1965), who explains the details of corona discharge particularly explicitly. Research shows that in the process of corona discharge, the gas molecules close to the emitter electrode are ionized due to the high potential gradient in a neutral gas, which results in a plasma creation around the emitter. The ionized molecules or ions then transfer their charge to other molecules of lower potential that are farther from the emitter.

This process divides the region between emitter and collector into three regions: the plasma region (conductive), the active zone (partially conductive) and the passive zone (neutral). The plasma region is at the emitter's surface and is surrounded by the active zone, which, in turn, is surrounded by the passive zone (see Figure 2-1). In terms of the size of each region, the passive zone is the largest, while the plasma is the smallest and the active zone is in between. The active zone thickness is only a small percentage of the passive zone thickness (Parker 1997).

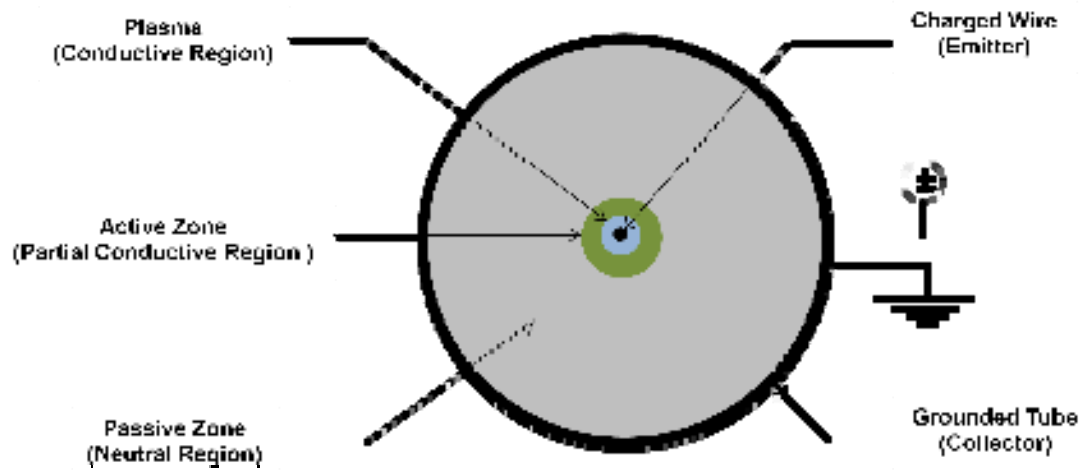

Figure 2-1 Top view of wire-tube geometry showing plasma, active and passive zones

The gas ions bordering the emitter will act as part of the emitter itself, increasing the size of the charged electrode and thus making it less sharp. Therefore, the ionization process is reduced in the outer region and stops altogether at a certain radius. If the ionization does not stop due to very high potential gradient, the ionized region will continue to grow, creating a conductive path between the two electrodes, eventually resulting in a voltage breakdown, which can be seen as a momentary spark or a continuous arc.

The moving electrons and ions between the two electrodes will develop a relation between the current and voltage. It is important to highlight this relation, since it verifies the quality of the corona discharge.

2.1.2. Current-Voltage Characteristics Curve (CVC)

The ionization quality of gas molecules due to corona discharge can be determined using the current-voltage characteristics curve (CVC) (White 1963). This curve can be used to determine power consumption during the ionization process,

since it provides the relation between resultant current (I) at a certain applied potential. The CVC also shows the onset voltage value (ϕ_0), which is the minimum voltage needed to start the ionization process in any fluid. And finally, it shows the breakdown voltage, the level at which the maximum allowed voltage is reached.

Figure 2-2 shows the different regions of the CVC curve. The ionization process does not start until the voltage reaches the onset voltage level. Once ionization starts, current flows between the electrodes, beginning at the low ionization region, and then moving to the high ionization region. The slope becomes steeper as voltage is increased. Finally it reaches the breakdown voltage.

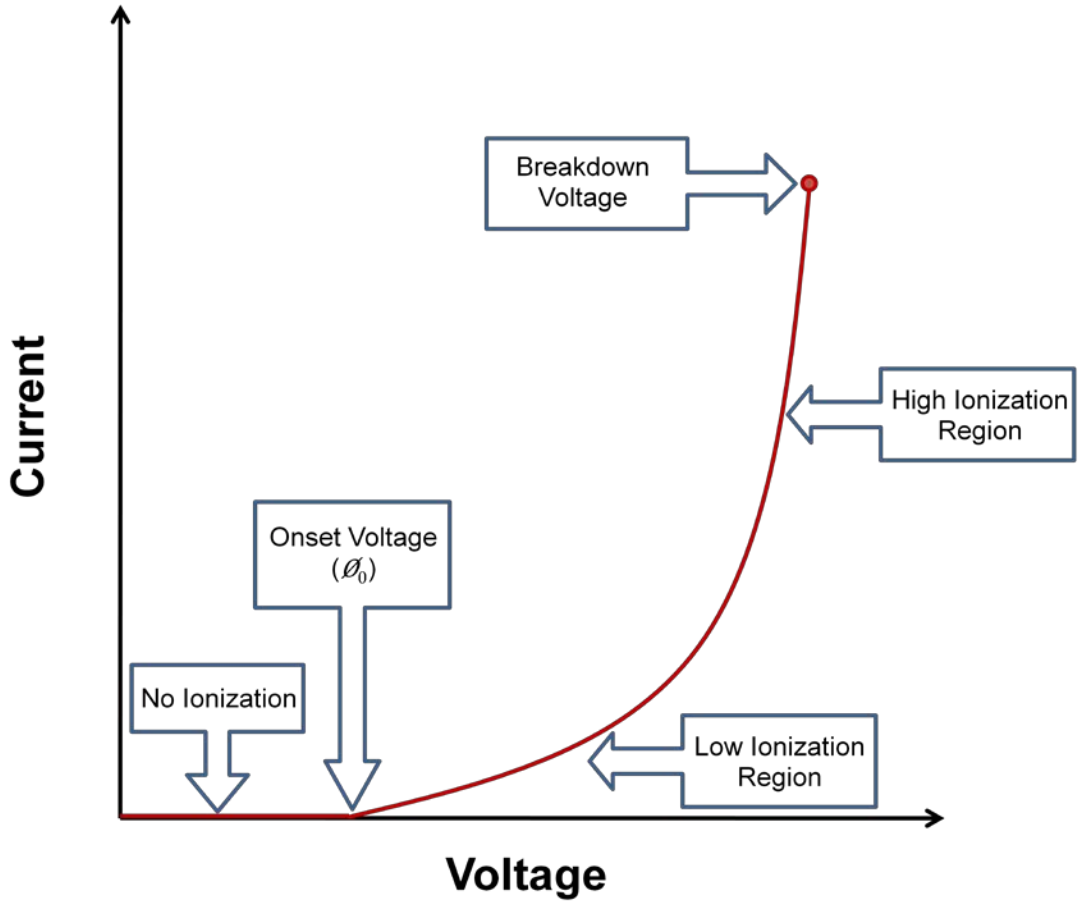

Figure 2-2 Current-voltage characteristics curve

Many parameters play a vital role in the ionization process and are reflected in the CVC curve, including polarity of the emitter electrode (+,-), fluid conditions such as temperature (T_f) and pressure (P_f), and geometry, which is the diameter of the wire or emitter (d_w) and tube or collector (d_t) or the spacing between the needle and plate or tube. The following sections will explain the effects of these parameters in detail.

2.1.2.1. Polarity of Emitter (Positive and Negative Corona)

The polarity of the emitter is the main parameter affecting ionization of gas molecules, since the ionization mechanism is different for both polarities. If the emitter electrode is connected to a power supply with positive polarity, the corona is called a positive corona, whereas it is called a negative corona when it is connected to power supply with negative polarity. Each polarity plays an important role in the ionization of the gas, and each polarity has a different appearance, different properties, and different advantages over the other.

The first and most obvious difference between the two polarities is their appearances (Zeleny 1924). In a positive corona, the plasma region is more stable and glows blue. On the other hand, for the negative corona, the plasma region is larger and appears as wavy tufts or brushes (see Figure 2-3). This increases the size of the active zone in the negative corona.

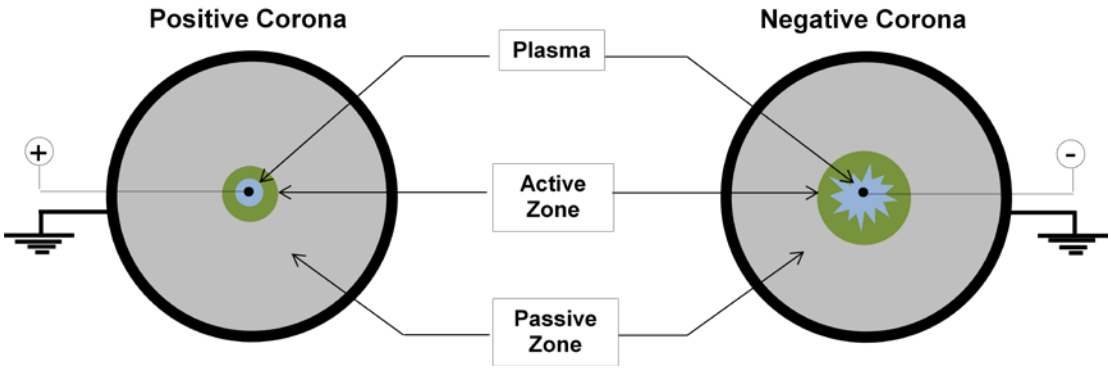

Figure 2-3 Appearance difference between positive and negative coronas

The different behaviors of the two polarities can be explained by the ionization process of the molecules in the gas. In the case of positive corona, the ions (i) are created at or just beyond the active zone, where electrons (e) are drawn to the emitter from neutral molecules, making them positive ions (i^+), where they move to the collector. The density of electrons is much greater than the positive ions. In the passive zone there is no ionization. The electron avalanche that then travels inward to the wire helps in maintaining the shape of plasma region around the wire, which is why no tufts exist in the positive corona.

On the other hand, in the negative corona, electrons are repelled from the gas molecules in the plasma and active zone regions. Then the electron avalanche travels outward to the collector with much higher density than the positive ions, which are traveling inward to the emitter. The direction of electrons' movement creates tufts on the surface of the plasma and expands its size. Chen and Davidson (2003) showed that the number of electrons in plasma is about 50 times greater for a negative corona, whose thickness can reach up to 200 μm. The ionization of gas molecules by electrons is very effective, since electrons have long, mean-free paths between

collisions, and this allows them to gain high energy from the electric field (Townsend 1903).

The ionization process is not limited to the active zone only in the negative corona, but rather is continuous throughout the passive region. The accelerated electrons with high energy free more electrons when they strike gas molecules. Then the velocity of electrons starts to decrease when they travel further from the emitter due to decreasing field strength. At this stage, electrons attach to gas molecules, making them negative ions (i^-), where they travel to the collector (see Figure 2-4).

The negative corona is only possible in gases with electronegative gas elements: for example, oxygen, chlorine, sulphur dioxide and many other gases that have high electron affinity due to their lack of electrons in their outer electron orbits (Brown 1959). On the other hand, negative corona is not possible in gases that have no such affinity, such as nitrogen, hydrogen and helium. These gases work as a trap for electrons and prevent them from reaching other molecules.

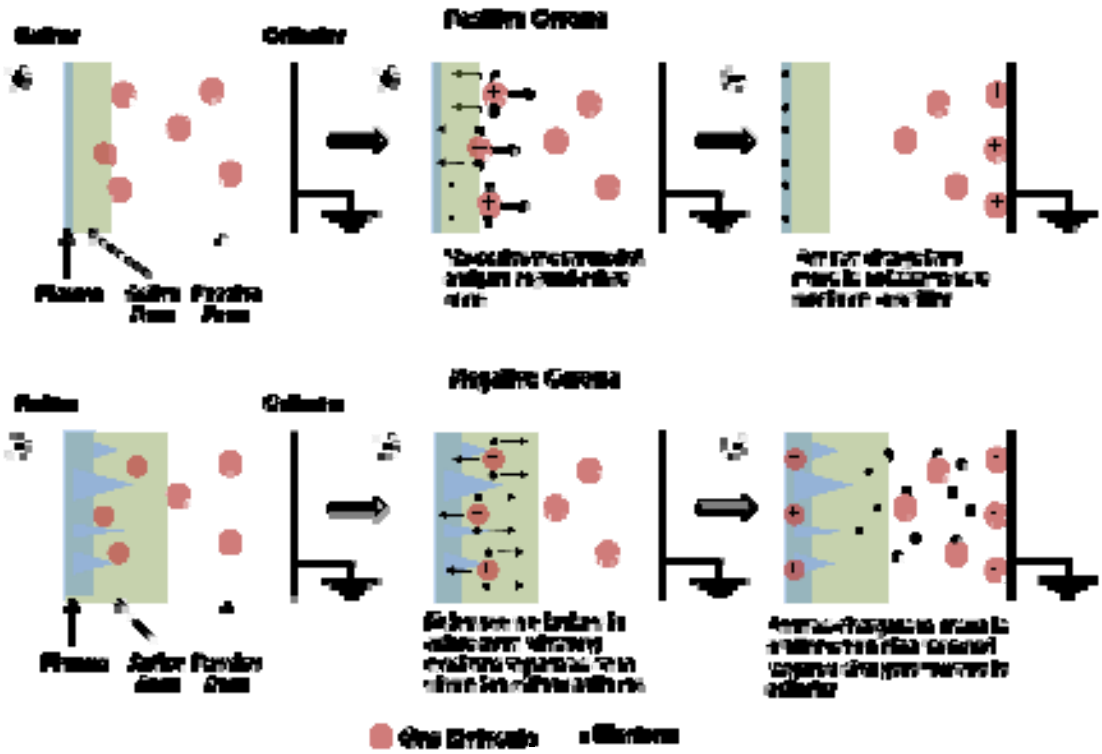

Figure 2-4 Ionization process for positive and negative coronas

The value of the maximum voltage reached in the positive corona is lower than the negative corona. This can be explained by the streamer theory of breakdown (Loeb and Meek 1941), which states that in the positive corona, the breakdown starts from the emitter in a high field region. In contrast, in the case of negative corona, the breakdown starts from the relatively low field region near the collector. Therefore, breakdown requires higher voltage than in the positive corona case.

As mentioned earlier, each corona polarity has advantages over the other in terms of solid particle separation (such as dust, smoke and particulate matter). For example, positive corona is preferable for indoor use due to its low ozone emission. In contrast, negative charging is more favorable for industrial use because of its superiority over positive corona and its ability to achieve higher efficiency (Hinds 1999).

2.1.2.2. Fluid Condition

Several investigations have studied the effect of flow condition on the corona discharge ionization process. White (1963) presented in his book a proportional relationship between gas temperature and corona discharge current. He found that as gas temperature increases, kinetic energy of the gas molecules rises, which increases the current. On the other hand, higher gas pressure resulted in a lower corona current.

The same relation was obtained between humidity and corona current. Higher humidity resulted in a lower corona discharge current. This is because of the electron affinity of the gas. For negative corona, as the electron affinity of a gas is low, the gas is incapable of supporting negative corona. In H_2O case, water has moderate electron affinity, so it is less supportive of corona current. These results are in agreement with Ohadi et al. (1994), who studied the effects of these parameters in an electrostatic heat exchanger.

The droplets contained in a gas flow might affect the relation between current and voltage. Sugita et al. (2003) found that the corona discharge current increased dramatically when water droplets were sprayed into the airflow. Xu et al. (2003) reached the same conclusion when studying various new electrode designs for water sprays with direct current. They found that current was higher with an air-water mixture than dry air alone.

Bologa et al. (2004) investigated CVC with air-oil mixture. They found that current decreased slightly, 3-5 %, when oil mists were injected in the gas flow. Ohadi et al. (1994) obtained a current reduction of about 40% with humid air for negative polarity charging. The difference in the resultant current between water and oil might

be caused by the relative permittivity difference between oil and water. The relative permittivity (ε_p) for mineral oil, which is usually used as a lubricant for compressors, is 2-4.5 at room temperature, whereas it is about 80 for water.

2.1.3. Analytical Prediction of the CVC Curve

Researchers have tried to calulate and predict the relation between resultant current and applied voltage in corona discharge. Peek (1929) developed a semiempirical formulla to calculate threshold field strength (E_0) and onset voltage for negative polarity. For a wire-tube geometry, and gas medium of air, this emprical relation can be presented as

$$E_0 = \left(30\,\delta + 9\sqrt{\frac{2\,\delta}{d_w}}\right) \times 10^5 \qquad \textbf{(2-2)}$$

$$\phi_0 = \frac{d_w}{2}\,E_0\,\log\frac{d_t}{d_w} \qquad \textbf{(2-3)}$$

$$\delta = \frac{T_0}{T_f}\,\frac{P_f}{P_0} \qquad \textbf{(2-4)}$$

where δ is identified as the relative density, T_0 is room temperature, and P_0 is atmospheric pressure.

Equation (2-3) shows that by increasing the diameter of wire, the onset voltage inreases and the ionization process starts at a higher voltage value. The diameter can be increased until the value of onset voltage is equal to the breakdown voltage. In this case, corona discharge does not occur. Peek (1929) found the

minimum ratio of the tube-to-wire diameters (d_t/d_w) to be 2.7 for corona discharge to occur in the system.

2.2. Particle Charging

Particles inside the electric field will become highly charged by colliding with moving electrons and ions. The resultant electrostatic force due to the charge can be greater than the gravity force by thousands of times (Hinds 1999). The electric charging acquired by the particles depends on many things, including the particle diameter size (d_p), ionic electric field strength, ionic charge density (ρ_i), the length of time that those particles are exposed to electric field (t), and relative permittivity or dielectric constant of the particles (ε_p). The relative permittivity (ε) in general represents the permittivity ratio of the electrostatic field produced in different materials (β) to the electrostatic field produced in a vacuum (β_0) under fixed potential and fluid conditions, Equation (2-5).

$$\varepsilon = \frac{\beta}{\beta_0} \qquad \textbf{(2-5)}$$

After acquiring a minimum limit charge, the particles will move away from the electrode with the same charge (emitter) to the electrode with opposite charge (collector). Since the lifetime of ions is brief due to mutual repulsion between ions and their high mobilities, ions must be continuously produced at high concentration in order to achieve particle charging. Corona discharge is proven to be the optimum method for such an application, prevailing over other ionization methods (Hinds 1999).

Research shows that two distinct mechanisms are active in charging the particles: diffusion charging (q_{diff}) and field charging (q_{fld}). Both mechanisms should be taken into account when investigating particle charging (Liu and Yeh 1968). Particle size plays an important role in determining the dominant charging mechanism. For a submicron particle, diffusion charging is dominant, while field charging becomes the prevailing factor when the particle diameter is in the micron range.

2.2.1. Diffusion Charging

When a particle is presented in a region filled with randomly moving ions created by a high voltage difference between two electrodes, it will become charged. This happens because the thermal motions of the ions cause them to diffuse through the gas and collide with particles due to Brownian motion. Such ions will generally adhere to particles due to the attractive electrical-image forces that come into play as the ions approach the particles (see Figure 2-5). The accumulation of electric charge on the particle gives rise to a repelling field, which tends to decrease the charging rate. Thus, the rate of charging decreases as charge accumulates on the particle and will ultimately proceed at a negligible rate, but it does not stop. As charge builds up, the particles move to the electrode that has the grounded electrode.

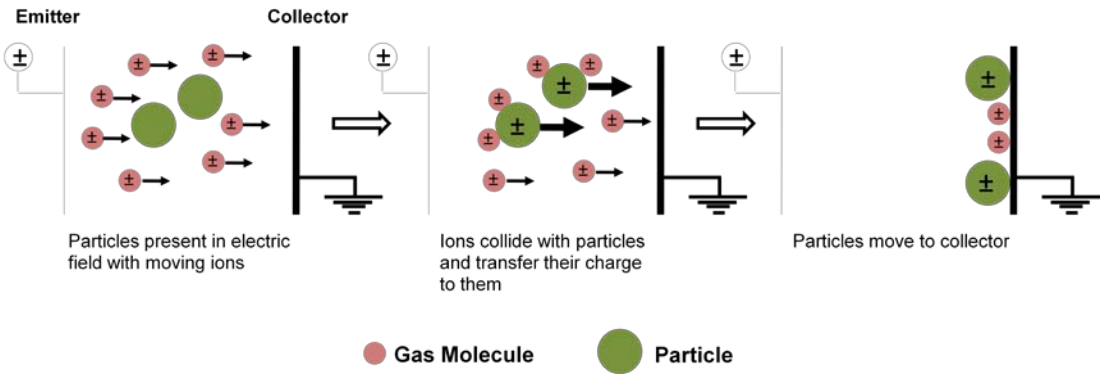

Figure 2-5 Diffusion charging mechanism

Unlike the electric field intensity, the charge density of the ions has a direct influence on this type of charging mechanism. Also, the temperature of the flow affects the charging process, but the particle's material to a first approximation plays no role. Assuming that every ion that strikes a particle due to Brownian motion is captured, the amount of accumulated diffusion charge on a given spherical particle is given by Equation (2-6):

$$q_{diff} = \frac{d_p\, k\, T_f}{2\, K_E\, e} \ln\left(1 + \frac{\pi\, K_E\, d_p\, \bar{C}_i\, e\, \rho_i\, t}{2\, k\, T_f}\right) \qquad \textbf{(2-6)}$$

where k, K_E, and $\bar{C}_i$ are the Boltzmann constant, proportionality constant (which depends on system of units used) and the mean thermal speed of the ion, respectively.

2.2.2. Field Charging

In field charging, as depicted in Figure 2-6, a particle enters a region of traveling ions between electrodes. The presence of the particles disturbs ions traveling along electrical field lines, so the ions strike the particle and transfer their charge to the particle's surface. After the particle becomes partially charged, the field strength around the particle will decrease and, as a result, the number of field lines will

decrease. After some time, the particle reaches a state called *saturation charge* ($q_{fld,sat}$), where there are no more field lines converging on the particle, so the charge rate becomes zero. After the particle is charged, it moves to the grounded electrode.

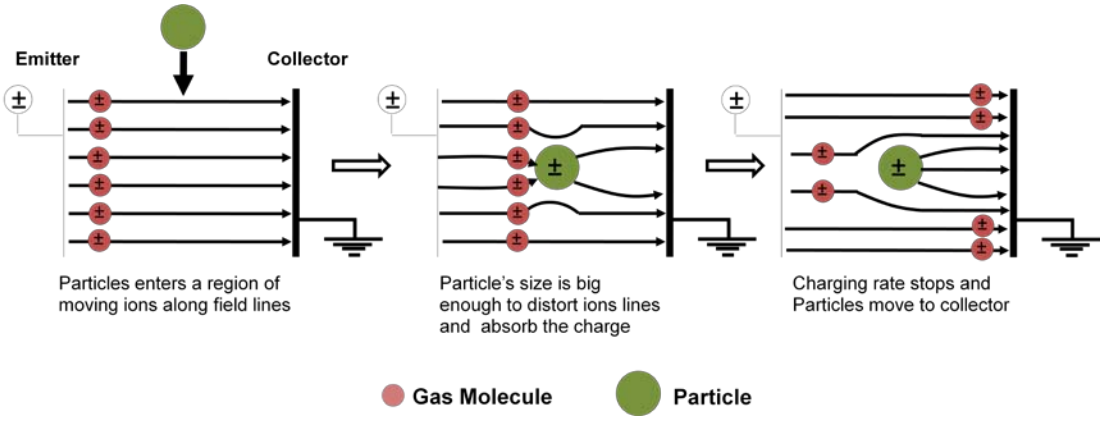

Figure 2-6 Field charging mechanism

Unlike the diffusion charging process, this type of charging is affected greatly by the electric field and material of the particle. Field charging can be presented mathematically by Equation (2-7):

$$q_{fld} = \left(\frac{3\,\varepsilon_p}{\varepsilon_p + 2}\right)\left(\frac{\mathbf{E}\,{d_p}^2}{4\,K_E}\right)\left(\frac{\pi\,K_E\,Z_i\,\rho_i\,t}{1 + \pi\,K_E\,Z_i\,\rho_i\,t}\right) \qquad \textbf{(2-7)}$$

where Z_i is the ion mobility. As t approaches infinity, the last term in Equation (2-7) becomes negligible and the saturation charge due to field charging can be presented by Equation (2-8).

$$q_{fld,sat} = \left(\frac{3\,\varepsilon_p}{\varepsilon_p + 2}\right)\left(\frac{\mathbf{E}\,{d_p}^2}{4\,K_E}\right) \qquad \textbf{(2-8)}$$

The first term on the right hand of Equation (2-7) depends on the particle's material and ranges from 1.0 to 3.0 for ε_p of 1.0 to ∞, respectively. The second term shows that field charging is proportional to electric field strength and the particle's surface area.

2.2.3. Charging Limit

The charging rate of a particle will reach a certain limit at which it will completely stop or become insignificant. The charge accumulated at the surface of the particle will affect the shape of the particle in the case of liquid droplets. The difference in charging limit between solid particles and liquid aerosols is discussed in the following sections.

2.2.3.1. Solid Particles

The maximum charge limit is reached when a particle reaches a state where it cannot accept more charges and starts emitting charges from its surface. This is due to the resultant electric field generated at the surface of the particle, causing the electrons on the surface to be ejected by the force of mutual repulsion (Hinds 1999). This limit can exist for solid particles (q_L) only and can be presented by Equation (2-9),

$$q_L = \frac{{d_p}^2 E_L}{4 K_E} \qquad \textbf{(2-9)}$$

where E_L is the surface field strength that a particle needs to repel incoming charges from electrons or ions. For negatively charged particles, this value is estimated to be 9.0×10^8 V/m, and for positively charged particles it is 2.1×10^{10} V/m. In the case of

particles with negative charging, electrons are emitted, whereas with positively charged particles, positive ions are emitted. Since it requires more energy to emit positive ions than electrons, this limit is higher for positively charged particles.

2.2.3.2. Liquid Droplets

When electric charges accumulated on the surface of a droplet exceed the surface tension, the droplets break up; the *mother droplet*, as it is called, breaks into smaller ones, *daughter droplets*. Lord G. I. Rayleigh was amongst the first scientist to study the phenomenon of liquid droplet breakup (Rayleigh 1882). He tried to calculate the maximum charge that would cause the breakup of a perfect conductor liquid droplet existing in a vacuum where there is no external electric field to disturb the surface of the droplet. He derived this relation using perturbation methods, and it came to be known as the Rayleigh limit (q_R) (see Equation (2-10)):

$$q_R = \pi\sqrt{8\,\gamma\,\beta_0\,{d_p}^3} \qquad \textbf{(2-10)}$$

where γ is the surface tension of the droplet.

Many researchers have tried to validate this limit experimentally. Early works focused on verifying the breakup of a charged single droplet existing in a space where there is no electrical field gradient, using the Millikan force balance method (Millikan 1935). Some studies were within about 70-100 % agreement of the Rayleigh limit (Doyle, et al. 1964, Abbas and Latham 1967, Schweizer and Hanson 1971, and Taflin, et al. 1989). Other studies investigated the accuracy of Equation (2-10) when droplet diameters were varied. Gomez and Tang (1994) and Davis and Bridges (1994)

independently verified that the charge limit of large droplets tended to agree with the Rayleigh limit more than smaller droplets. In contrast, De Juan and Fernandez De La Mora (1997) found that breakup of smaller drops of viscous liquid was in better agreement with the Rayleigh limit than the breakup of bigger drops. On the other hand, one work claimed that for some types of liquid, breakup occurred independently of droplet diameter (Richardson, et al. 1989). Many factors contribute to the difference in the results for these studies, such as shape of the droplets, the accuracy of the equipment, and the difficulty of measuring the charge and size of droplets.

In an attempt to validate the breakup of a droplet in an electrical field gradient space, De Juan and Fernandez De La Mora (1997) found that the induced charge (q_i) of the droplet that leads to its breakup is significantly smaller than the Rayleigh limit This difference is due to the free surface charge (q_f). Shrimpton (2005) tried theoretically to calculate the maximum free surface charge that could participate in the breakup (see Equations (2-11) and (2-12)):

$$q_R = q_f + q_i \tag{2-11}$$

$$q_f = q_R \left(\frac{\varepsilon_s}{2\,\varepsilon_s - 1}\right)\left(1 - \frac{3}{2}\,\mathbf{E}\sqrt{\frac{d_p\,\beta_0}{2\,\varepsilon_s\,\gamma}}\left[\frac{\varepsilon_p - \varepsilon_s}{\varepsilon_p + 2\,\varepsilon_s}\right]\right) \tag{2-12}$$

where ε_s is relative permittivity of space.

Based on Equations (2-10) and (2-11), the breakup charge for larger droplets tends to agree more with the Rayleigh limit than smaller droplets. This finding agrees

with what Gomez and Tang (1994) and Davis and Bridges (1994) proved in their experimental works.

Since the Rayleigh limit underestimates the needed charge for droplet breakup, many researchers have worked to devise a better relation for it. One of the inaccurate assumptions that Rayleigh made was that the shape of the droplet is spherical before it breaks, which was not true, as some researchers found (Wilson and Taylor 1925). The droplets instead have a conical shape and produce a jet of very fine droplets then they have already broken. Macky (1931) tried to calculate the critical electrical field (E_c^0) needed to cause droplet breakup based on the type and diameter of a droplet as shown in Equation (2-13):

$$E_c^0 \propto \left(\frac{\gamma}{d_p}\right)^{1/2} \quad \textbf{(2-13)}$$

In 1964, Sir Geoffrey Taylor redefined this relationship as Equation (2-14), or Taylor's limit, as it came to be known. One of his main assumptions was that instability of a droplet would not occur unless there was a pressure difference between inside and outside the droplet, which contradicted what some researchers assumed (Zeleny 1917):

$$E_c^0 = \frac{c}{(8\,\pi)^{1/2}} \left(\frac{4\,\gamma}{\beta_0\, d_p}\right)^{1/2} \quad \textbf{(2-14)}$$

where c = 1.625 for a liquid droplet in air.

Taylor also derived a relationship between applied field strength and the resulting aspect ratio (σ), which is the ratio of major to minor axis of the spheroid droplet.

$$\mathbf{E} = I_2\, \sigma^{-4/3}(2 - \sigma^{-3} - \sigma^{-1})^{1/2} \left(\frac{4\,\gamma}{\beta_0\, d_p}\right)^{1/2} \qquad \textbf{(2-15)}$$

$$I_2 = \frac{1}{2\,(1 - \sigma^{-2})^{3/2}} \ln\left[\frac{1 + (1 - \sigma^{-2})^{1/2}}{1 - (1 - \sigma^{-2})^{1/2}}\right] - \frac{1}{1 - \sigma^{-2}} \qquad \textbf{(2-16)}$$

The droplet becomes unstable when $\mathbf{E} = E_c^0$, and that, which occurs when σ = 1.85.

2.3. Particle Collection

Collecting charged particles is the second step, after charging. The objective of industrial applications is to collect unwanted particles from gas flows. Issues that accompany particle collection are presented in the following sections.

2.3.1. Collection Mechanism

After acquiring a certain charge from moving ions in the gas medium, the particle will move to the electrode of opposite charge and deposit on its surface. This action will depend on the particle's charge, the strength of the electric field and the velocity of the gas flow. Also, the position of the particle or how far it is from the collector will affect the collection process along with the length of the collector. The charge of the particle and the strength of the electric field can be evaluated by the terminal velocity ($\mathbf{u}_p$) of the particle, which is the velocity of the particle toward the collector (see Figure 2-7).

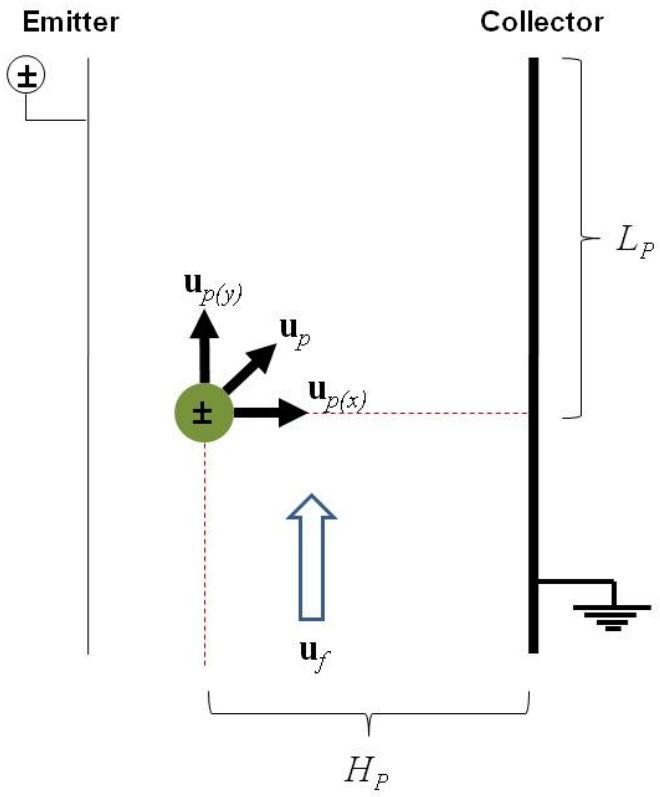

Figure 2-7 Terminal velocity of a charged particle under electric field in moving gas

For laminar flow, theoretically, 100% of the particles will be collected if the following condition in Equation (2-17) is applied:

$$\mathbf{u}_p > \mathbf{u}_f \frac{H_p}{L_p} \qquad \textbf{(2-17)}$$

where $\mathbf{u}_f$, H_p and L_p are the fluid velocity, distance between particle and collector and the vertical distance between particle and end of the collector, respectively. Equation (2-17) is considered in the design of electrostatic precipitators (ESPs) when flow is laminar.

When the flow is turbulent, as is the dominant case in ESPs, Equation (2-17) cannot be considered. In order to measure the efficiency of particle separation in

ESPs ($\eta_{ESPs,Tur}$) for wire-tube geometry, the Deutsch-Anderson equation is applied (Deutsch 1922).

$$\eta_{ESPs,Tur} = 1 - \exp\left(\frac{-V_{TE}\, A_c}{Q}\right) \quad \textbf{(2-18)}$$

The collection surface of the collector (A_c) is

$$A_c = \pi\, d_t\, L \quad \textbf{(2-19)}$$

where Q is flow rate and L is the length of the collector. There are many assumptions behind Equation (2-18), including that particles are distributed uniformly across every section and that particles are fully charged once entering the ESP.

2.3.2. Back Corona and Particle Re-entrainment

The continuation of particle deposition on the collector surface will create a thin layer in case of solid particles or liquid film in case of droplets. This layer will change the ionization process and make it weaker. This condition is called "back corona." Some of the collected particles will have the tendency to go back to the gas flow, which is called "particle re-entrainment." This happens because of gas flow, particle collision, or electrostatic forces.

The particle layer at the collector's surface will increase the resistivity of the particles, where back corona exists at a resistivity of 2×10^{10} ohm-cm. The particle layer will also change the CVC where the ionization is decreased and will lead to lower efficiency. The breakdown voltage will occur at an earlier stage. Therefore, the removal of collected particles is essential for continuing, efficient operation.

2.4. Mathematical Model of Electrostatic Body Force on a Particle

The particle will have net forces acting on it due to fluid flow and electric field. The following section will highlight the main equations that reflect these forces on a particle along with some assumptions for electrostatic force in flow field.

2.4.1. Momentum Balance Equation

To simulate the net forces acting on a particle, consider a particle subject to electric and fluid flow fields for isothermal flow. The trajectory can be determined from the momentum balance applied to this particle:

$$\frac{d\mathbf{u}_p}{dt} = F_D\left(\mathbf{u}_f - \mathbf{u}_p\right) + \frac{\mathbf{g}\left(\rho_p - \rho_f\right)}{\rho_p} + \mathbf{F}_e \qquad \textbf{(2-20)}$$

where $\mathbf{u}_p$, ρ_p, ρ_f, $\mathbf{g}$, F_D, and $\mathbf{F}_e$ are particle velocity, particle density, fluid density, gravity, Stokes drag force, and electrostatic body force, respectively. The Stokes drag force is given as

$$F_D = C_{F_D}\frac{18\,\mu_f}{\rho_p\,{d_p}^2} \qquad \textbf{(2-21)}$$

where μ_f is fluid dynamic viscosity. The constant (C_{F_D}) depends on the particle's diameter size and can be presented by Equation (2-22). This is because for submicron particles, drag force acting on the particles is independent of the relative Reynolds number. Stokes's law assumes that the relative velocity of the gas at the surface of a droplet is zero. Since this assumption is not accurate for submicron particles, the

Cunningham correction factor (C_c) must be included in the calculation of the drag force (Qunis, et al. 1991):

$$C_{F_D} = \begin{cases} \frac{C_D \, \mathrm{Re}_p}{24} & , d_p > 1.0 \; \mu m \\ \frac{1}{C_c} & , d_p < 1.0 \; \mu m \end{cases} \quad \textbf{(2-22)}$$

where C_D and Re_p are the drag coefficient and relative Reynolds number, respectively. The drag coefficient for spherical particles is calculated by using developed correlations at different ranges of Reynolds numbers (Morsi and Alexander 1972). The relative Reynolds number and Cunningham correction factor can be defined as

$$\mathrm{Re}_p = \frac{\rho_f \, d_p \, |\mathbf{u}_p - \mathbf{u}_f|}{\mu_f} \quad \textbf{(2-23)}$$

$$C_c = 1 + \frac{2\,\lambda}{d_p}\left(1.257 + 0.4\, e^{\frac{-1.1\, d_p}{2\,\lambda}}\right) \quad \textbf{(2-24)}$$

where λ is the mean free path, which is defined as the average distance traveled by a molecule between successive collisions. The electrostatic body force in Equation (2-20) can be represented as

$$\mathbf{F}_e = \frac{q_p \mathbf{E}}{{}^1\!/_6 \; \pi \, {d_p}^3 \, \rho_p} \quad \textbf{(2-25)}$$

To calculate this body force, the local electric field in the vicinity of the particle and the charge accumulated on the particle (q_p) must be determined. The

total particle charge is the summation of diffusion charging and field charging (see Equations (2-6) and (2-7)).

$$q_p = q_{diff} + q_{fld} \tag{2-26}$$

Then Equation (2-20) can be rewritten as

$$\frac{d\mathbf{u}_p}{dt} = C_{F_D}\frac{18\mu_f}{\rho_p {d_p}^2}(\mathbf{u}_f - \mathbf{u}_p) + \frac{\mathbf{g}(\rho_p - \rho_f)}{\rho_p} + \frac{\mathbf{E}}{{}^1\!/_6\,\pi {d_p}^3 \rho_p} \left[\frac{d_p k T_f}{2K_E e}\ln\left(1 + \frac{\pi K_E d_p \bar{C}_i e \rho_i t}{2kT_f}\right) + \left(\frac{3\varepsilon_p}{\varepsilon_p + 2}\right)\left(\frac{\mathbf{E}{d_p}^2}{4K_E}\right)\left(\frac{\pi K_E Z_i \rho_i t}{1 + \pi K_E Z_i \rho_i t}\right)\right] \tag{2-27}$$

2.4.2. Dimensionless Form of Momentum Balance Equation

Presenting the momentum equation for a particle, Equation (2-27), in a non-dimensionless form leads to the appearance of a new set of dimensionless numbers. These numbers are due to the effect of flow and electric fields. The dimensionless numbers due to flow field, such as Reynolds and Froude numbers, are well known, whereas in electric field they are not commonly used. Therefore, a new set of dimensionless numbers due to electric field are recommended to be used (IEEE-DEIS-EHD Technical Committee 2003). Table 2-1 shows the dimensionless numbers used in the momentum balance equation. Readers who are interested in more information about applying these dimensionless parameters in EHD governing equation should consult the work of Shoushtari (2004).

Table 2-1 Dimensionless Numbers

Symbol	Expression	Name
Re	$\frac{\rho_p L u'}{\mu_f}$	Reynolds Number
Fr	$\frac{u'}{\sqrt{\mathbf{g} L}}$	Froude Number
$E_{hd,p}$	$\frac{L^3 E' \rho_i'}{\rho_p v_p^2}$	EHD Number (Conductive Electric Rayleigh Number)
Md	$\frac{\beta_0 L^2 E'^2}{\rho_p v_p^2}$	Masuda Number (Dielectric Electric Rayleigh Number)
λ_D	$\left(\frac{\beta_0 k T_f}{e \rho_i'}\right)^{1/2}$	Debye Length
Db	$\left(\frac{L}{\lambda_D}\right)^2$	Debye Number
τ	$\frac{t' u'}{L}$	Mechanical Convection Time
τ_i	$\frac{t' \bar{C}_i}{L}$	Mechanical Convection Time (Ions)
τ_E	$\frac{t' Z_i \rho_i'}{\beta_0}$	Space Charge Decay Time

$$d_p = L d_p^* \qquad \mathbf{u}_p = u' \mathbf{u}_p^* \qquad \mathbf{u}_f = u' \mathbf{u}_f^*$$

$$\mathbf{E} = E' \mathbf{E}^* \qquad \rho_i = \rho_i' \rho_i^* \qquad t = t' t^* \qquad \textbf{(2-28)}$$

After using the mentioned dimensionless parameters and dimensionless parameters in Equation (2-28), the non dimensional form of Equation (2-27) can be presented as

$$\frac{d\mathbf{u}_p^*}{dt^*} = 18C_{F_D}\frac{\tau}{\mathrm{Re}}\frac{\left(\mathbf{u}^* - \mathbf{u}_p^*\right)}{{d_p^*}^2} + \frac{\tau}{\mathrm{Fr}^2}\frac{\left(\rho_p - \rho_f\right)}{\rho_p} + 6\frac{\tau}{\mathrm{Re}^2}\frac{\mathbf{E}^*}{{d_p^*}^3} \quad \textbf{(2-29)}$$

$$\left[2\frac{\mathrm{E_{hd,p}}}{\mathrm{Db}}d_p^*\ln\left(1+\frac{1}{8}\tau_i\mathrm{Db}d_p^*\rho_i^*t^*\right) + \left(\frac{3\varepsilon_p}{\varepsilon_p+2}\right)\left(\mathrm{Md}\mathbf{E}^*{d_p^*}^2\right)\left(\frac{\tau_\mathrm{E}\rho_i^*t^*}{4+\tau_\mathrm{E}\rho_i^*t^*}\right)\right]$$

The dimensionless equation and numbers were not used in this work except for just short summary presented in section (8.3) as a part of recommended future work.

2.5. Summary

The fundamentals of electrostatic charging due to corona discharge were reviewed in this chapter. Also the main parameters that affect the corona discharge mechanism were highlighted and explained. The particle charging and collection mechanisms were reviewed in detail along with particle behavior in an applied electrostatic field. At the end of the chapter, the mathematical form of the momentum balance equation for a particle under electrostatic field was presented along with its non-dimensional form.

CHAPTER 3: LITERATURE REVIEW—GAS-LIQUID DROPLET SEPARATION

This chapter will present the existence technologies for separating liquid droplets from gas flows. Also, it will review the background and the previous studies on the effect of electrostatic force on liquid droplets. The analytical and numerical studies found in the literature will also be discussed.

3.1. Background

The separation of suspended particles from gases has been one of the basic scientific and technical problems of the industrial era, and this interest continues today (White 1963). Stricter environmental legislation and standards on emissions of fine particles have been motivating forces in the development of more efficient separators. Different industrial applications, such as clean rooms for various operations including micro- and nano-fabrication technologies, refrigeration and HVAC systems, and many other applications require controlled droplets concentrations in moving gaseous mediums to maintain system functionality and efficiency.

One example of droplet removal from gas flow is the separation of oil droplets from refrigerant in refrigeration cycles at the exit of the compressor, which is very important in maintaining system efficiency (ASHRAE 2008). The build-up or carry-over of micron-side droplets of lubricating oil from compressors lowers the performance and decreases the system's efficiency. The droplets contaminate the

systems, while they lower the cooling capacity in heat exchangers. Also, in the long run, if the droplets are not removed, compressors will be damaged due to loss of lubricating oil. One study showed that for every 1% contamination of oil in a refrigerant system, the system efficiency will drop 3% ((Key 2002)). Another study conducted by Yun, et al. (2007) investigated the effect of polyalkylene glycol (PAG) oil concentration in a supercritical CO_2 system in minichannel tubes. They found that when oil concentration was increased from 0 to 4 wt.%, the average gas cooling heat transfer coefficient was decreased by 20.4% and the average pressure drop was increased by 4.8 times.

The oil leaves compressors as very small droplets of micron and submicron sizes. A study conducted by Temprite, an oil management company in the refrigeration industry, showed that droplet size ranges between 0.1-40 μm, and more than 50% of these droplets are below 1.0 μm (Temprite, Inc. 2007). At high pressure and RPM, compressors release oil as smoke whose particle size ranges between 0.03-1.0 μm (Air Cleaninf Equipment, Inc. 2007). The small size of the droplets makes separating them from gas flow very challenging.

Another application of droplet removal from gas flow is the removal of water droplets from an airflow in environmental control system (ECS) such as in aerospace applications. Additional applications can be found in the health and environmental safety area. For instance, the separation of radioactive aerosols from air in treatment and sludge retrieval operations in high-level radioactive waste tanks is considered an important health issue. Another example is gas-liquid droplet separation in flare knock-out drums to reduce emitting harmful gases to environment.

The droplets in gas flow have a wide range of size depending on how they are produced and how they are affected by the medium around them. Flow conditions such as temperature and velocity have a major effect on droplet size. Droplets may be classified as sprays, mists or aerosols, depending on their size (Bürkholz 1989). If the droplet's size is greater than 10 μm then it is classified as a spray, and if it is less than 10 μm then it is classified as a mist or an aerosol.

3.2. Existing Conventional Technologies

A variety of methods for separating droplets from process streams operate under different principles, such as inertial separation as applied in cyclones (centrifugal) and wave-plate separators, and impaction and diffusion as used in packed-bed and coalescence force-based filters. However, many industrial and conventional gas-liquid separators are limited in terms of separating fine droplets from gas streams (Scharge, et al. 1998) and (TeGrotenhuis and Stenkamp 2001). This is because in most conventional separation systems performance depends on the difference in density between gas and liquid. In the case of very small droplets, this difference vanishes and separator performance decreases.

As general rule, the efficiency of a separator is associated with the size of droplets that it can separate. Therefore, a curve of the efficiency vs. the droplet's size is needed to evaluate the separator performance. This efficiency is called grade efficiency (also known as fractional efficiency), η_G, since it does not represent the overall efficiency of the separator, but rather its efficiency at a certain droplet size.

3.2.1. Inertial-Based Separators

- **Cyclone Separators**

In this type of separator, the gas-liquid droplet mixture goes under radial motion as in cyclone or centrifugal separators, then the gas leaves through an outlet that is in the axial direction, see Figure 3-1. The design of this type is either conical or cylindrical. The gas enters the separator tangentially. Because of the density difference between gas and liquid, droplets become separated from gas and are deposited on the separator housing. The limitation of this type of separator is its efficiency dependency on droplet size. The efficiency falls dramatically when the aerosol diameter size drops below 1 µm. For such small droplets the density factor becomes insignificant and the droplets remain in the gas flow.

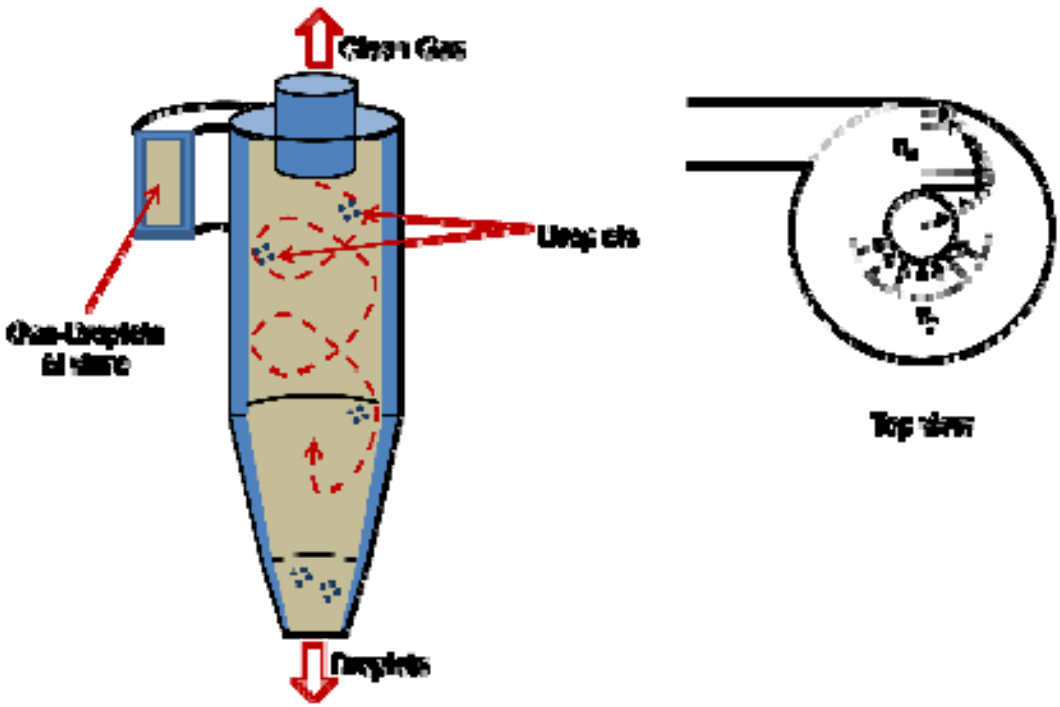

Figure 3-1 Cyclone Separator

- **Wave-Plate Separators**

This type is widely used in industry for droplet removal from gas flows. Wave plates (known also as baffle bundles) are made of a series parallel plates in a wave shape, as shown in Figure 3-2. Each plate consists of drainage champers that hold the separated droplets from re-entraining. This type of separator is efficient for removing droplets bigger than 5 µm and is preferred in high water-concentration applications (Calvert 1978).

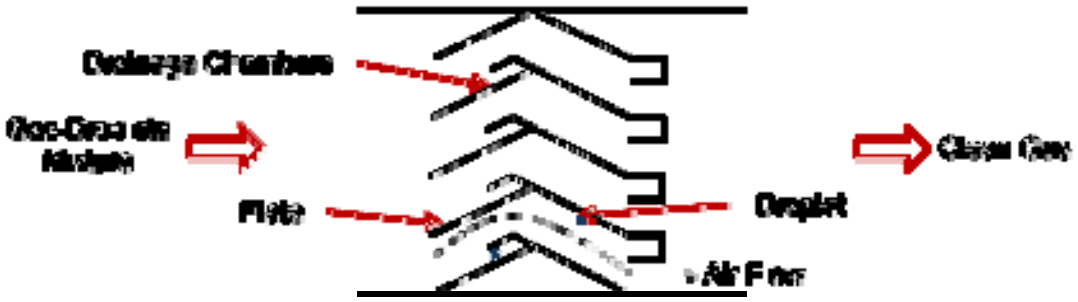

Figure 3-2 Wave-plate separator

3.2.2. Coalescence-Based Separators

- **Wire and Fiber Filters**

Wire and fiber filters are made out of a porous media structure made of wires or fibers. They can be arranged vertically or horizontally, uniformly or randomly. This media structure forces small droplets in the gas flow to join and create bigger droplets. Then the droplets are drained to a liquid reservoir, and the gas exits in a clean condition, as shown in Figure 3-3. Although coalescence-based separators are more efficient, their performance decreases when droplet size is below 0.5 µm. In addition, this type of separator has significant pressure drop and a high maintenance cost.

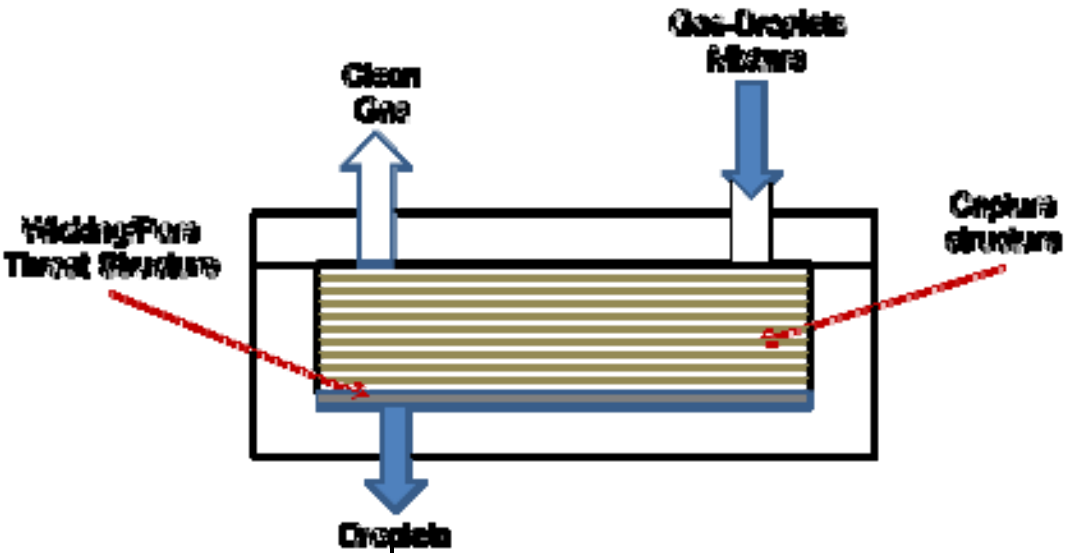

Figure 3-3 Coalescence Separator

- **Packed Bed Separators**

In this type of separator, liquid is sprayed from the top while the gas that has liquid droplets is flowing upward, see Figure 3-4. When the liquid and gas are in contact, liquid continues flowing down, carrying the droplets with it. The goal of packed bed separators is to increase the contact surface area between liquid and gas. Different materials are used for packed beds, including steel Pall rings and glass Raschig rings.

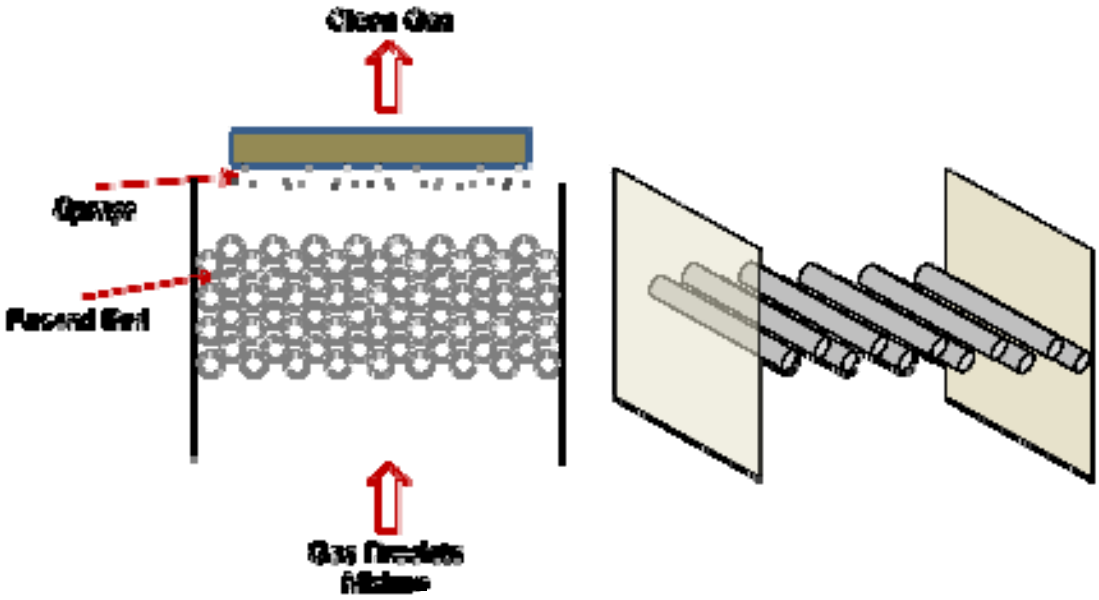

Figure 3-4 Packed bed separator

To overcome the limitations of conventional separators in terms of small droplet separation, researchers have investigated the possibility of increasing the size of droplets in order to enhance separation efficiency. One of these investigations focused on water droplet growth through heterogeneous condensation (Heidenreich and Ebert 1995). Based on their theoretical and experimental results, they concluded that a droplet's size of few nanometers can be enlarged with high growth rates. Unfortunately, this technique is not feasible for all applications, so a new separation technology must be employed.

3.3. Experimental Works on Gas-Liquid Droplet Separation via Electrostatic Force

It was mentioned in Chapter 2 that electrostatic precipitators (ESPs) are used on a large scale in industry to remove solid particles (such as dust, smoke, or particulate of matter) from gas flow. However, little experimental work on utilizing

electrostatic forces to separate droplets (sprays, aerosols and/or mists) from gas flows has been conducted. In general, the application of ESPs in separating droplets is very limited and has not been implemented as in dust separation (Bürkholz 1989). However, utilizing ESPs in the separation of droplets should be more thoroughly studied, especially since liquid droplets usually have higher relative permittivity than solid particles, which makes them more attracted to electrostatic field. Also, collected droplets can be simply drained out of a collector's surface, whereas, in contradictory, solid particles simply accumulate at the surface and participate in the back corona and particle re-entrainment, which decreases the ESP's performance. Despite these advantages only a few studies on utilizing ESPs to separate droplets were found in the literature. The industrial applications are discussed below, followed by a review of the analytical literature on ESP gas-liquid separation.

- **Separation of Sulfuric Acid Mist**

In this application, sulfuric acid mist is removed from flue gas using ESP-based technology, as shown Figure 3-5. For this operation, the temperature of the gas is reduced to 110 ^{o}C in order to condense the acid. The sulfuric acid removal efficiency can be as high as 99.7% (Tomimatsu 1999).

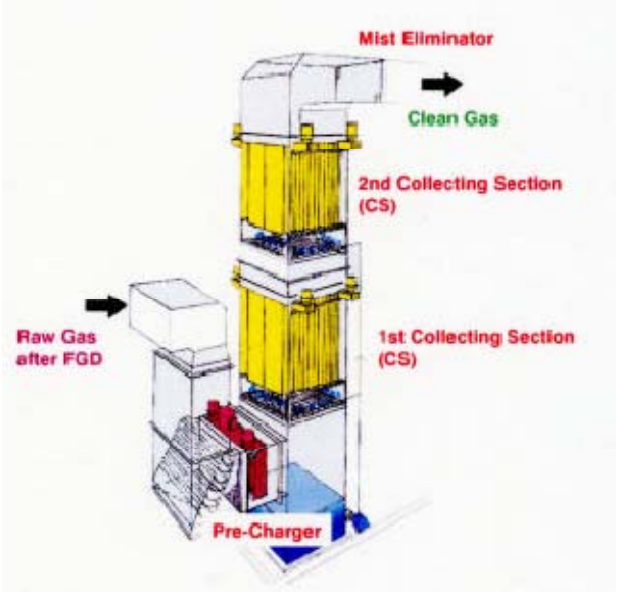

Figure 3-5 Sulfuric acid removal unit, adopted from Tomimatsu (1999)

- **Separation of Oil Mist**

A two-stage ESP is used to remove oil mist from an airflow (Bologa, et al. 2004). The dirty air passes through a filter to remove large droplets, then proceeds to the ionization section to separate small droplets, as shown in Figure 3-6. The efficiency of oil separation for this process ranges between 96.5 to 99% depending on the droplet's size.

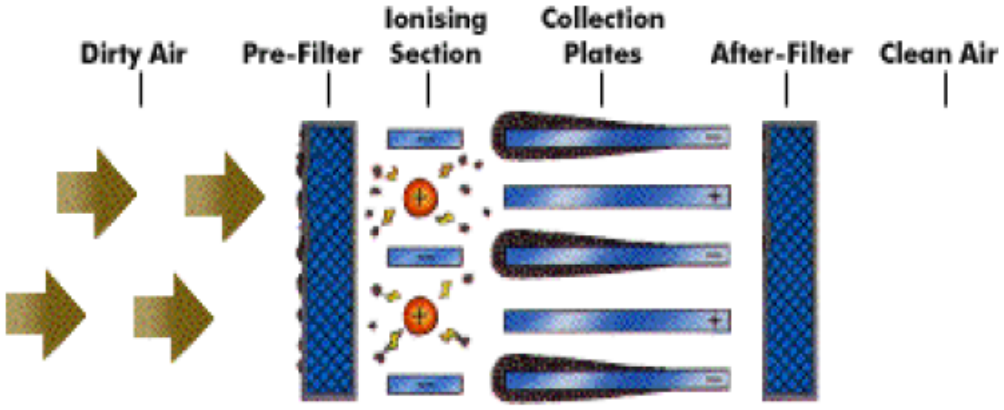

Figure 3-6 Oil droplet removal unit, adopted from Bologa, et al. (2004)

Few experimental studies have evaluated the effect of different parameters on the separation efficiency of electrostatic force. This is due to the unstable nature of droplets. Unlike solid particles such as dust, droplets might evaporate, break up and/or coalescence after colliding with other droplets. On the other hand, a lot of numerical and analytical studies have been published in this field.

3.4. Analytical Studies on Gas-Liquid Droplets Separation via Electrostatic Force

Many researchers and scientists have tried to represent the electrostatic effect on traveling particles using mathematical models. In 1824, M. Hohlfeld, a mathematics teacher in Leipzig, Germany, first described the precipitation of smoke particles by electricity. The first commercially successful process was developed in 1906 following experiments by F.G. Cottrell at the University of California, Berkeley. In 1926, Deutsch made the first attempt to derive a theoretical equation for the particle charging process, but his attempt failed because he did not recognize the difference between diffusion and field charging. A few years later, Arendt and Kallmann (1926) developed the first theoretical expression for diffusion charging that gave the rate of particle charging, assuming that the particle had already taken an appreciable charge. For field charging, Rohmann (1923) and Pauthenier and Moreau-Hanot (1932), working individually, derived a theoretical expression for field charging.

Numerical simulation of the separation process in ESPs involves modeling the electrohydrodynamic (EHD) flow due to the interaction between the electric field and

the space charge within the fluid flow, as well as the particle movement. To model the effect of all of these phenomena, one should solve the Maxwell equation for the electrostatic field and space charge coupled with both particle dynamics and Navier-Stokes equations. In terms of particle movement, both Eulerian and Lagrangian approaches have been widely used to predict particle dispersion in an ESP. The Eulerian method is based on solving the continuity equation of particles to obtain particle concentration distribution, while in the Lagrangian method the momentum equation for each particle is solved to obtain its trajectory. The performance characterization of ESPs depends on the solution of this coupled problem, which can be obtained with a varying degree of accuracy using different models characterized by different degrees of complexity and computational cost.

In his book Parker presented some cases that highlighted the efficiency of electrostatic precipitators with different flow conditions (Parker 1997). He used the theoretical migration velocity of solid particles (such as dust or smoke) obtained by Riehle to calculate the separation efficiency (Riehle 1929). When he compared the theoretical and experimental outcomes, he found that the efficiency for the experimental work was much higher than the theoretical one.

Goo and Lee (1997) developed a numerical scheme to estimate the collection efficiency of particles in the wire-plate ESP. Some of the physical phenomena they considered were corona-field, turbulent EHD flow-field, in situ particle charging and turbulent motion of particles. They used the Lagrangian particle-tracking method coupled with the Monte-Carlo method for simulating the stochastic nature of turbulence to overcome the deficiencies of the Eulerian method. The analytical code

was used to analyze an experimental work done earlier by Kihm (1987). The calculated efficiency was lower than the experimental one due to many factors such as the difficulty in estimating the exact charging properties of the particles used in the experiment and the inlet conditions of the flow and the particles.

Talaie et al. (2001) developed a numerical model based on the Eulerian approach to predict the performance of a double-stage electrostatic precipitator. In their work, the effect of polydisperse particle loading was directly included in the velocity distribution, electrical field distribution, and particle concentration. Also, the change in gas eddy diffusivity was considered in their model. Their results confirmed the significant effect of particle size distribution on ESP performance.

Sugita et al. (2003) investigated the behavior of water aerosols under electrostatic force in order to separate it from an airflow. The study used theoretical analysis to investigate the motion of a water aerosol under electrostatic forces and the theoretical length of the separator needed to collect the aerosols. The mean diameter of the water aerosols they used was 30 μm. They were able to obtain an analytical equation for the minimum length needed to collect the aerosols.

Soldati (2003) later on developed a two-dimensional Eulerian, advection-diffusion type model for particle transport with distributed parameters. A cost function for a model ESP was defined, and the influence of a number of design parameters on cost and collection efficiency was examined. The results showed that the most cost-effective way to increase the collection efficiency of a wire-plate ESP is to decrease the wire-to-wire distance.

Then Talaei (2005) came up with a two-dimensional mathematical model for the performance of wire-duct, single-stage electrostatic precipitators. The main objective of his model was to study the effect of inlet particle concentration and applied voltage on corona sheath thickness. He used the Lagrangian approach to predict the movements of particles. He found that increasing particle concentration participates in quenching corona sheath thickness.

Lei et al. (2008) performed a numerical study to investigate the behavior of charged particles in electrostatic precipitators for turbulent flow. They used the Eulerian approach to simulate the electrostatic fields and the Langragian approach for in situ particle charging and tracking. They found that for particles smaller than 0.1 μm, the flow turbulence had a very significant effect on their movements, but the difference of charge among particles was not obvious. On the other hand, particles larger than 10 μm were not influenced by the flow turbulence in their movememnt, but they reached the saturation charge quickly. For particles lying in between, the effect was not obvious.

3.5. Summary

This chapter reviewed the background and recent research on various conventional technologies used to separate liquid droplets from gas flows. It also represented examples from industry where the electrostatic force in ESPs used to separate droplets. It showed that there is a lack in experimental work on the effect of some parameters on the separation process; this lack should be addressed. On the other hand, numerical and analytical studies presented in this chapter showed that such studies have been the focus of research in the area of separation.

CHAPTER 4: NUMERICAL MODELING

4.1. Introduction

More numerical modeling studies than experimental works can be found in the literature in the area of particle charging and separation in gas flow due to the complexity of experimental work, especially in the case of liquid droplets. The goal of developing a computational model is to conduct a parametric study on how applied electric potential (ϕ_e), fluid velocity ($\mathbf{u}_f$), fluid temperature (T_f) and length of collecting tube (L) will affect the grade efficiency (η_G). Also, the effect of relative permittivity of particles (ε_p) will be evaluated through injecting droplets of two different liquids. Equation (4-1) represents how the grade efficiency is defined in this model. The cases studied involved separating water droplets from air.

$$\eta_G = 1 - \frac{\text{No. of Escaped Particles}}{\text{No. of Injected Particles}} \qquad \textbf{(4-1)}$$

In addition to efficiency calculation, the model will be used also to predict the number of charges on the surface of particles (n). The relation between charge (q) and number of charges is presented in Equation (4-2). It was mentioned in section 2.2(2.2.3.2) that droplets might break up due to the accumulated charge on the surface of the droplets. If we know the surface charge of the droplets, we can compare it against Rayleigh limit (q_R) to determine whether the droplets are broken up.

$$q = \mathrm{n}\, e \qquad \textbf{(4-2)}$$

4.2. Model Assumptions

The momentum balance equation on a particle along its non-dimensional form was explained in section (2.42.4.1). In order to simulate the effect of electric field on particle charging, the following assumptions were taken into consideration:

1. The effect of flow field on electric field and moving ions between electrodes is negligible.
2. Corona discharge has insignificant effect on flow field since $E_{hd,f}/Re^2 < 1$ (Chang, et al. 2006).
3. The fluid flow field is not affected by the motion of the particles.
4. All the particles are spherical.
5. The charge of particles at the inlet is zero.
6. The temperatures of the particles and fluid are the same.
7. The initial velocity of particles at the inlet is the same as fluid velocity.
8. The accumulated charge on each particle does not affect the local electric field.
9. Due to low particle concentration, there is no interaction among the particles, such as collisions and coagulation.
10. The particles disappear (are removed) once they touch the ground electrode (collector).

The velocity of the fluid can be obtained from continuity and the Navier-Stokes equations, as shown in Equations (4-3) and (4-4), respectively.

$$\nabla . \mathbf{u}_f = 0 \qquad \textbf{(4-3)}$$

$$\rho_f \left(\mathbf{u}_f \,.\nabla \mathbf{u}_f\right) = -\nabla P_f + \mu_f \nabla^2 \mathbf{u}_f + \mathbf{F}_{EHD} \quad \textbf{(4-4)}$$

where $\mathbf{F}_{EHD}$ is the electrohydrodynamic body force applied to the particle carrier fluid and is given as

$$\mathbf{F}_{EHD} = \rho_i \mathbf{E} \quad \textbf{(4-5)}$$

The ion charge density (ρ_i) and electric field strength (**E**) should be used in the mathematical model. In order to do so, the Poisson's (or Gauss's law) (Equation (4-6)) and conservation of charge (Equation (4-7)) must be solved.

$$\nabla^2 \phi = -\frac{\rho_i}{\beta} \quad \textbf{(4-6)}$$

$$\frac{\partial \rho_i}{\partial t} + \nabla . \mathbf{J} = 0 \quad \textbf{(4-7)}$$

The current density (**J**) is the summation of ionic mobility, conduction and convection components, respectively, given as

$$\mathbf{J} = \rho_i Z_i \mathbf{E} + \sigma_i \mathbf{E} + \rho_i \mathbf{u}_f \quad \textbf{(4-8)}$$

Since the electrical conductivity of gases (σ_i) is negligible, and the velocity of fluid is much less than ion velocity (Z_i **E**), the last two terms in Equation (4-8) can be dropped out. Therefore,

$$\mathbf{J} = \rho_i Z_i \mathbf{E} \quad \textbf{(4-9)}$$

The total electrical current passing from the charged electrode (emitter) to the ground electrode (collector) is given by

$$I = \int_{A_0} \mathbf{J} \cdot \mathbf{dA} \tag{4-10}$$

where A_0 is any closed area that encloses the emitter or collector electrodes.

4.3. Boundary Conditions

The boundary conditions must also be specified to be able to solve the set of governing equations and determine the trajectory of every particle entering the computational domain. The boundary condition for Equation (2-20) at the injection surface (inlet) is given by

$$\mathbf{u}_p = \mathbf{u}_f \tag{4-11}$$

The boundary conditions for Equation (4-4) depend on the given geometry and are straightforward. For example, on walls, the no-slip condition is imposed. For Equation (4-6), the following boundary conditions are enforced:

$$\begin{cases} \phi = \phi_e & \text{on the charged electrode (emitter) surface} \\ \phi = 0 & \text{on the ground electrode (collector) surface} \\ \dfrac{d\phi}{dn} = 0 & \text{on all other surfaces} \end{cases} \tag{4-12}$$

where ϕ_e is the applied voltage at the wire surface (emitter electrode) and n is local unit vector normal to the surface. Here it is assumed that, except the emitter and collector electrodes, all other surfaces are perfectly insulated.

The boundary conditions for charge density calculated from Equation (4-7) are more involved, and various approaches have been suggested. In the current work, it is assumed that:

$$\begin{cases} \rho_i = \rho_{i,e} & \text{on the charged electrode surface} \\ \dfrac{d\rho_i}{dn} = 0 & \text{on the ground electrode surface and all other surfaces} \end{cases} \quad \textbf{(4-13)}$$

where $\rho_{i,e}$ is the charge density at the emitter surface and its value is assumed to be known. If the current-voltage characteristic (CVC) of the separator is known, then $\rho_{i,e}$ can be set such that the calculated current from Equation (4-10) matches the experimental current for a given voltage.

4.4. Numerical Method

The commercial CFD code Fluent (version 6.2, Lebanon, NH) was used to solve the governing equations. Since the Fluent code does not provide a built-in solver for potential and charge conservation equations (i.e. Equations (4-6) and (4-7)), a user-defined program determining the charge density and the electric fields as well as the particle charging was written and incorporated with main source code (Shoushtari 2004). The electrostatic force influence on particles was modeled through an applied body force as described in Equation (2-20). The major steps of numerical solution are as follows:

1. Solve for the electric and ion charge density fields using Poisson's and charge conservation equations.
2. Solve for the flow field using Navier-Stokes and continuity equations.
3. Track particles using momentum equations and determine temporal charge accumulation on particles as they travel.

This numerical method can be applied to various geometries to study their performances. Since this method is based on the Lagrangian approach, the polydisperse particles injection can easily be incorporated.

4.5. Wire-Tube Geometry

The numerical method was used to perform a parametric study on classic wire-tube geometry. This is a simple geometry that conveniently represents many industrial applications. Moreover, from a modeling perspective, the advantage of this geometry is the availability of analytical solutions for electric field governing equations (i.e., Equations (4-6) and (4-7)). Therefore, the numerical results of these equations can be compared against the analytical solutions. The numerical results of particle tracking can be used to investigate the efficiency of this class of separators for separation of fine droplets. The length (L) of the wire and tube is the same as shown in the schematic configuration in Figure 4-1.

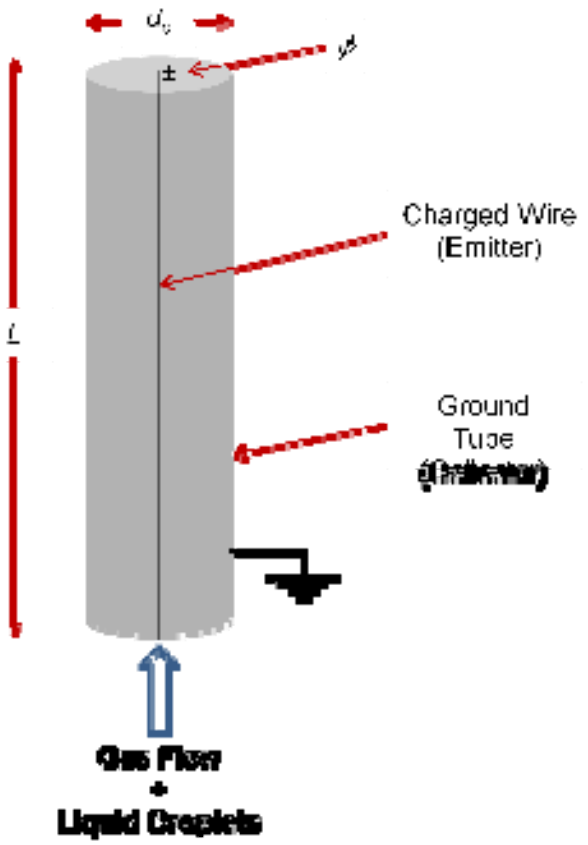

Figure 4-1 Wire-tube schematic

4.5.1. Modeling Parameters

In this modeling the particles were water aerosol droplets carried with the air stream. The modeling input parameters listed in Table 4-1 and Table 4-2 summarize the selected range of parameters used in this study. All thermophysical and electrical properties of fluid in Table 4-1 are at room temperature. For each modeling case, only one parameter changed at a time.

Table 4-1 Modeling Input Variables

Tube diameter (m)	d_t = 0.02
Wire diameter (m)	d_w = 0.00008
Fluid density (kg/m^3)	ρ_f = 1.18
Fluid viscosity (kg/(m.s))	μ_f = 1.86 × 10^{-5}
Fluid permitivity (F/m)	β_f = 8.854 × 10^{-12}
Aerosol relative permitivity	ε_p = 80
Ion mean thermal speed (m/s)	$\bar{C}_i$ = 240
Ion mobility (m^2/(V.s))	Z_i = 1.5 × 10^{-4}

Table 4-2 Modeling Varied Parameters

Wire electric potential (kV)	ϕ_e = 4, 5, 6, 7, 8
Average air flow inlet velocity (m/s)	$\mathbf{u}_f$ = 0.3, 0.6, 0.9, 1.2, 1.5
Air flow temperature (K)	T_f = 280, 300, 320
Separator length (m)	L = 0.05, 0.075, 0.1, 0.125, 0.15

The final study will investigate the relative permittivity of droplets effect on the separation performance. Since different liquids have different values of relative permittivity, then the effect of electrostatic charge on droplets of different liquids might be different from one liquid to another. Two liquid types will be used for this study, water and oil (synthetic lubricant). The reason of selecting water and oil is because of the wide range difference between their relative permittivity values. At

room temperature, the relative permittivity for water is 80, as mentioned in Table 4-1, where it is only 2 for oil. Refer to section (2.2) for more information about relative permittivity.

4.5.2. Computational Domain

Due to symmetry, only half of the cylindrical tube was considered as the computational domain, as shown in Figure 4-2. Also, since the electric force exerted on the airflow was axisymmetric, no recirculation was created, and air fluid flow was not affected by EHD interaction. Therefore, $\mathbf{F}_{EHD}$ in Equation (4-4) was not considered.

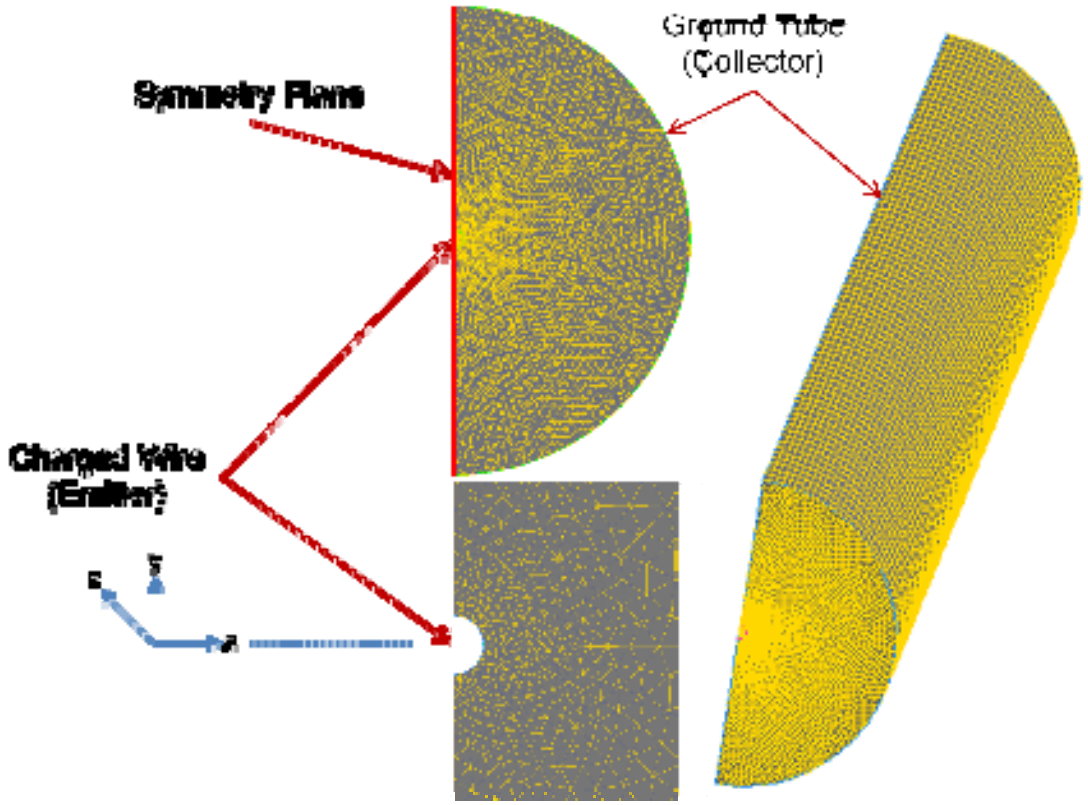

Figure 4-2 Computational fluid dynamic domain and grid system

The computational domain was descritized to 487520 computational cells using Tri-Pave meshing scheme in each cross-section as well as uniform meshing in the axial direction. To capture the high-intensity electric field, a high concentration of cells was created in the vicinity of the wire electrode.

For the fluid flow boundary condition, the fully developed parabolic velocity profile was imposed at the tube inlet such that average inlet velocity was equal to those values given in Table 4-2. For electric field, the wire electric potential was set based on values given in Table 4-2, and the tube wall was always grounded. The charge density on the wire electrode was set using the analytical solutions of Equations (4-6) and (4-7).

4.5.3. Solving Equations for Cylindrical Coordinates

Applied potential and charge density must be fed to the numerical solution. Since the applied potential is one of the model variables, charge density is the only variable that needs to be calculated. First, the initial electric field at the wire (E_0) was calculated using Peek's formula, Equation (2-2). Then the analytical solution of Poisson's equation, Equation (4-6), for cylindrical coordinates can be presented as

$$\frac{1}{r}\frac{d}{dr}\,r\,\frac{d\phi}{dr} = -\frac{\rho_i}{\beta} \qquad \textbf{(4-14)}$$

where r represents the displacement in the radial direction.

The current density, Equation (4-9), can be presented as Equation (4-15). Then by combining both Equations (4-14) and (4-15),

$$\mathbf{J} = 2\,\pi\,r\,\rho_i\,Z_i\,\mathbf{E} \qquad \textbf{(4-15)}$$

$$\frac{1}{r}\frac{d}{dr}\left(r\frac{d\phi}{dr}\right)^2 = -\frac{\mathbf{J}}{2\,\pi\,Z_i\,\beta} \qquad \textbf{(4-16)}$$

Two solutions exist for Equation (4-16), (Feng 1999):

1. For $C_1 \geq 0$, the solution is

$$\phi = -\sqrt{\left(\frac{\mathbf{J}}{2\,\pi\,Z_i\,\beta}\right)r^2 + C_1} + \sqrt{C_1}\ln\left(\frac{\sqrt{\left(\frac{\mathbf{J}}{2\,\pi\,Z_i\,\beta}\right)r^2 + C_1} + \sqrt{C_1}}{r}\right) + C_2 \qquad \textbf{(4-17)}$$

2. For $C_1 < 0$, the solution is

$$\phi = -\sqrt{\left(\frac{\mathbf{J}}{2\,\pi\,Z_i\,\beta}\right)r^2 + C_1} + \sqrt{-C_1}\arctan\left(\frac{\sqrt{\left(\frac{\mathbf{J}}{2\,\pi\,Z_i\,\beta}\right)r^2 + C_1}}{\sqrt{-C_1}}\right) + C_2 \qquad \textbf{(4-18)}$$

4.5.4. Particle Injection Method

The particles were injected using uniform surface distribution injection, Figure 4-3. A custom MATLAB code was written for uniform surface particle injection since the Fluent platform did not have this injection method as a built-in option. In this code, the initial velocity of particles in all direction was assumed to be zero and the temperature of gas flow and particles the same. The particles consist of water droplets moving in an airflow.

Preliminary tests of the model showed that the number of injected particles affects the separation efficiency significantly if it is lower than 200 particles. This is due to the effect of injection location. For example, if only one particle is injected it may be collected if it is close to the collector, but if it is not, then it may not be

collected. To eliminate the effect of particle injection locations, many particles should be injected. To minimize any error and to insure the efficiency independence on the particle number, 500 equally distant particles were injected in each study. The particles were assumed to be at a halt once they were injected, and they gradually accelerated along the airflow due to the drag force. The particles that were deflected by the electric field force and which collided with the tube wall were totally collected, and no reflection existed. It is assumed that there is no interaction between particles, in the form of collision or coagulation, due to their low concentration based on domain volume (less than 1.0 %).

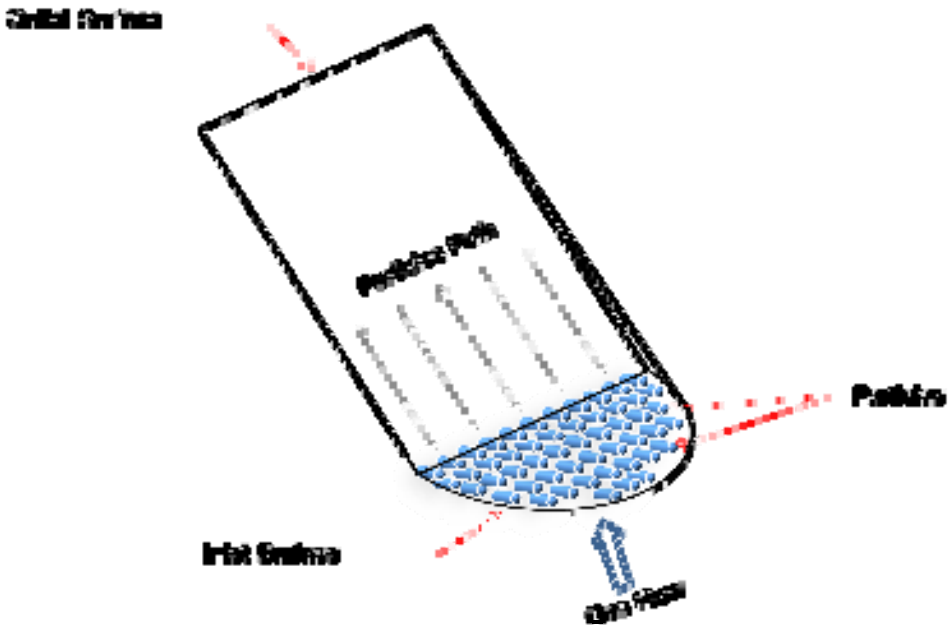

Figure 4-3 Uniform particle injection at inlet surface

4.5.5. Verification of Numerical Model

The numerical model solution for potential field and charge density was verified against the analytical solution, Equations (4-14) and (4-15). Figure 4-4 and Figure 4-5 show comparisons between both numerical and analytical results for the

applied electric potential and charge density distribution along the radial distance, respectively. The analytical solution was obtained from the work of Feng (1999), as mentioned earlier. As seen there, a favorable agreement between the results was obtained. The results show that the charge density decreases more than four-fold as one moves from the emitter to collector surfaces.

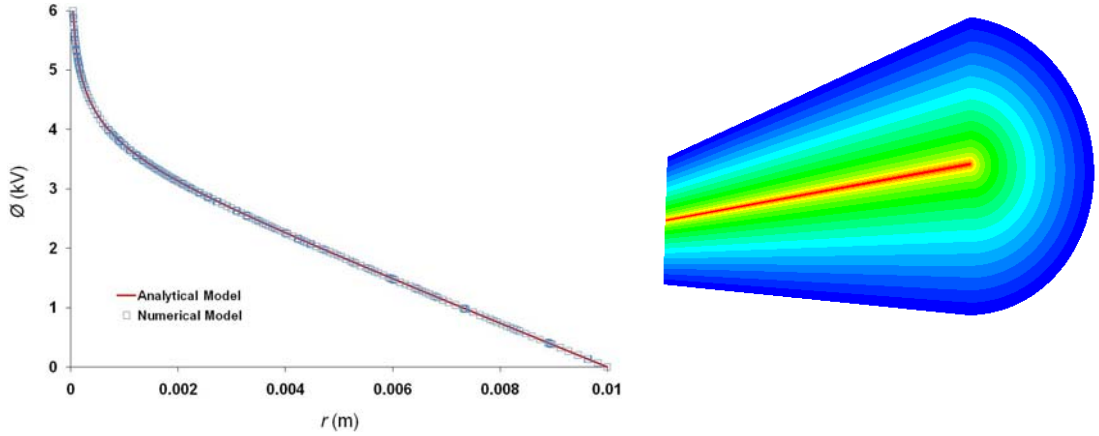

Figure 4-4 Comparison in electric potential field between numerical and analytical models (ϕ_e = 6.0 kV, u_f = 1.0 m/s, T_f = 300 K and L = 0.15 m)

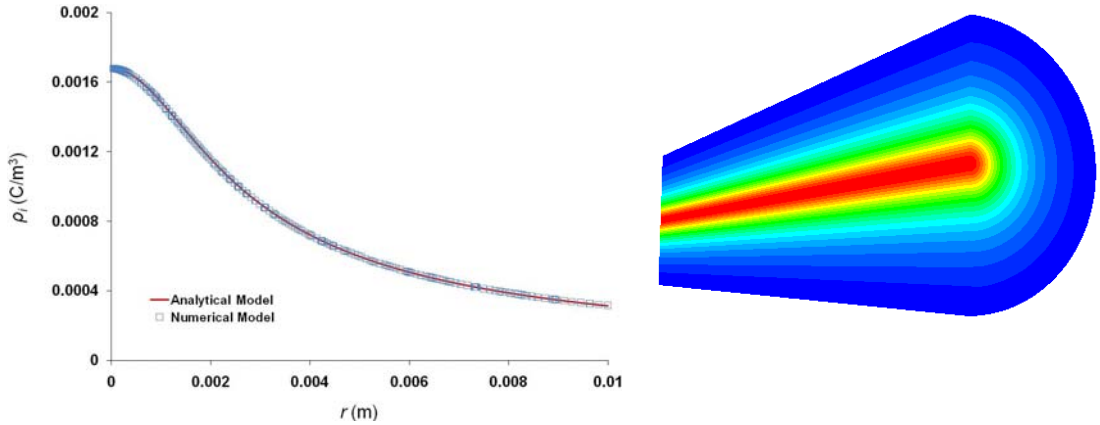

Figure 4-5 Comparison in charge density field between numerical and analytical models (ϕ_e = 6.0 kV, u_f = 1.0 m/s, T_f = 300 K and L = 0.15 m)

4.5.6. Current-Voltage Characteristics Curve

As the last step before generating results for the numerical model, the Current-Voltage Charcateristics (CVC) had to be obtained. This is important for calculating

the charge density, characterizing the separator performance, and calculating the power consumption. Figure 4-6 shows the CVC for the given separator geometry. The minimum voltage to sustain a corona discharge for the conditions studied here was 4 kV, which is in agreement with the corona onset voltage given by Equation (2-3). Since the emitter is a wire electrode, then the current in Figure 4-6 is presented as current per unit length (**J**).

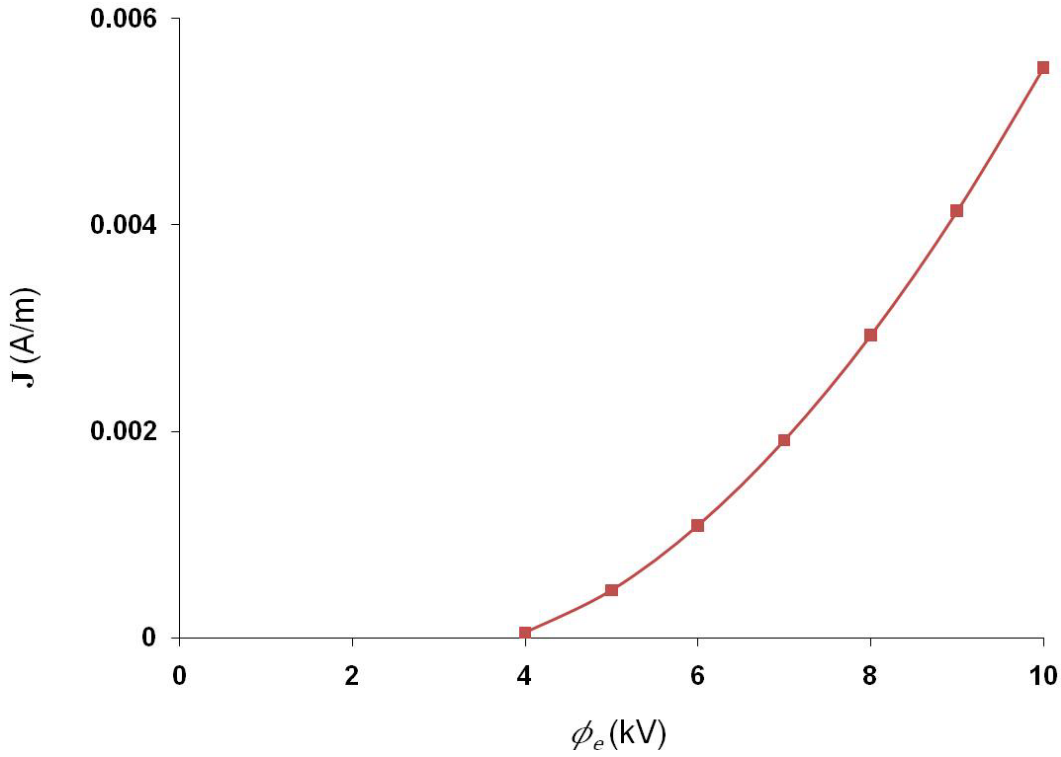

Figure 4-6 Current-voltage characteristics for the wire-cylinder separator at room temperature and ambient pressure

4.6. Numerical Results

The numerical model introduced in this chapter was used for different findings. First the accumulated charge on droplets was calculated to compare it against the Rayleigh limit. If the charge were found to be less than Rayleigh limit, then the possibility of droplet breakup would be very weak. Then the model was used

to conduct a parametric study on how the applied voltage, flow velocity, flow temperature and separator length would affect the grade efficiency. The flow in all of the studied cases is laminar flow (Re < 2300).

4.6.1. Accumulated Charge on Droplet Surface

Particle size plays an important role in how the particle is charged. Figure 4-7 shows the number of charges accumulated on injected particles as they travel inside the separator by each of the two different charging mechanisms, diffusion and field charging, as well as the combined effect. It can be seen from the figure that particles of less than 0.5 µm are charged mainly through diffusion charging, where particles of size greater than 0.5 µm are predominantly charged through field charging.

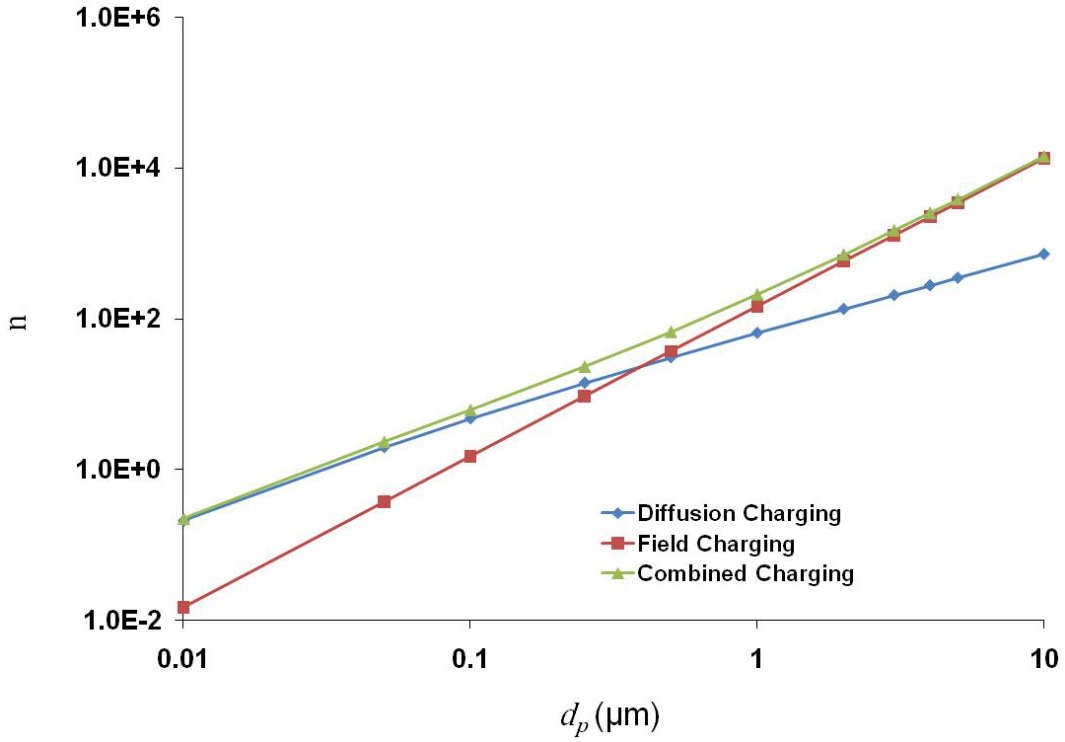

Figure 4-7 Number of charges accumulated on a particle due to diffusion charging, field charging or diffusion and field charging (ϕ_e = 4.0 kV, u_f = 1.0 m/s, T_f = 300 K and L = 0.15 m)

In order to ensure that the water aerosol droplets maintained their integrity and did not break into parts as they moved inside the high electric field, the number of accumulated charges had to be checked against the Rayleigh limit. Figure 4-8 shows a comparison between the Rayleigh limit calculated from Equation (2-10) and the number of accumulated charges over all the injected aerosol droplets. The difference ratio between the Rayleigh limit and accumulated charge on a particle ranged between 65 and 150. Therefore, theoretically the limit was not reached in this study and all other studied cases.

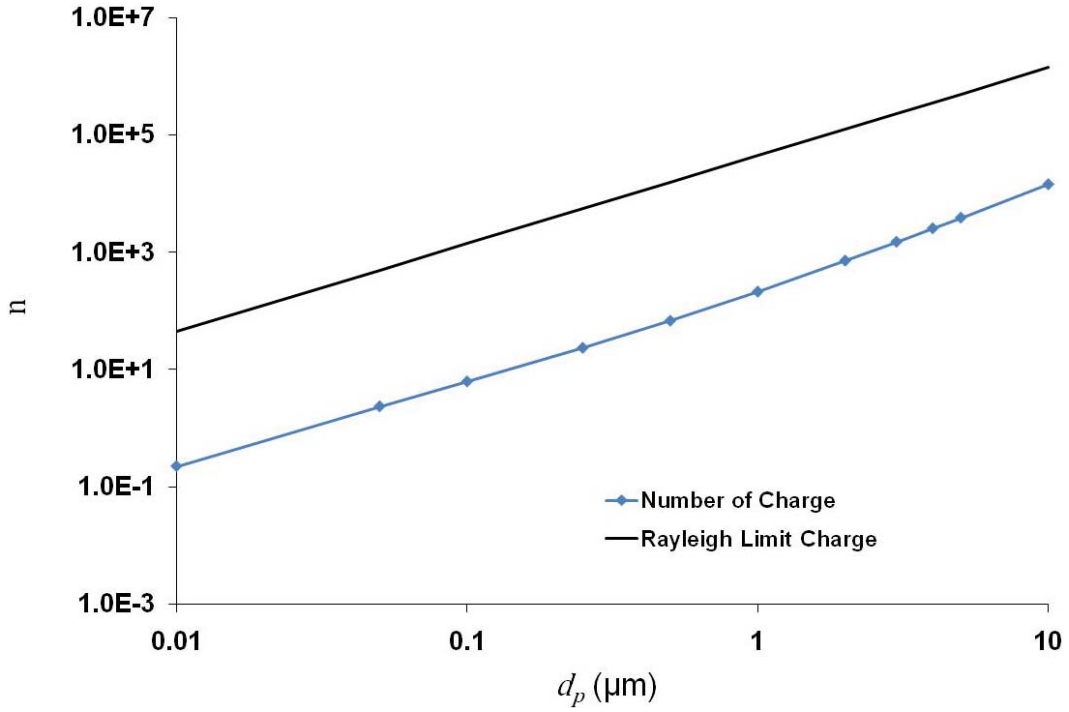

Figure 4-8 Comparison between Rayleigh limit and the number of charges accumulated on particles due to diffusion and field charging (ϕ_e = 4.0 kV, u_f = 1.0 m/s, T_f = 300 K and L = 0.15 m)

4.6.2. Parametric Study

For the following cases of the parametric study, the performance is based on the number of injected water droplets and number of the droplets that are not

collected, or escaped. Figure 4-9 shows a comparison case where a number of droplets are injected in the computational domain; one case not all droplets are collected and the other case all droplets are collected. Any droplets that reach the outlet are considered escaped. Then Equation (4-1) will be used to calculate the grade separation efficiency (η_G).

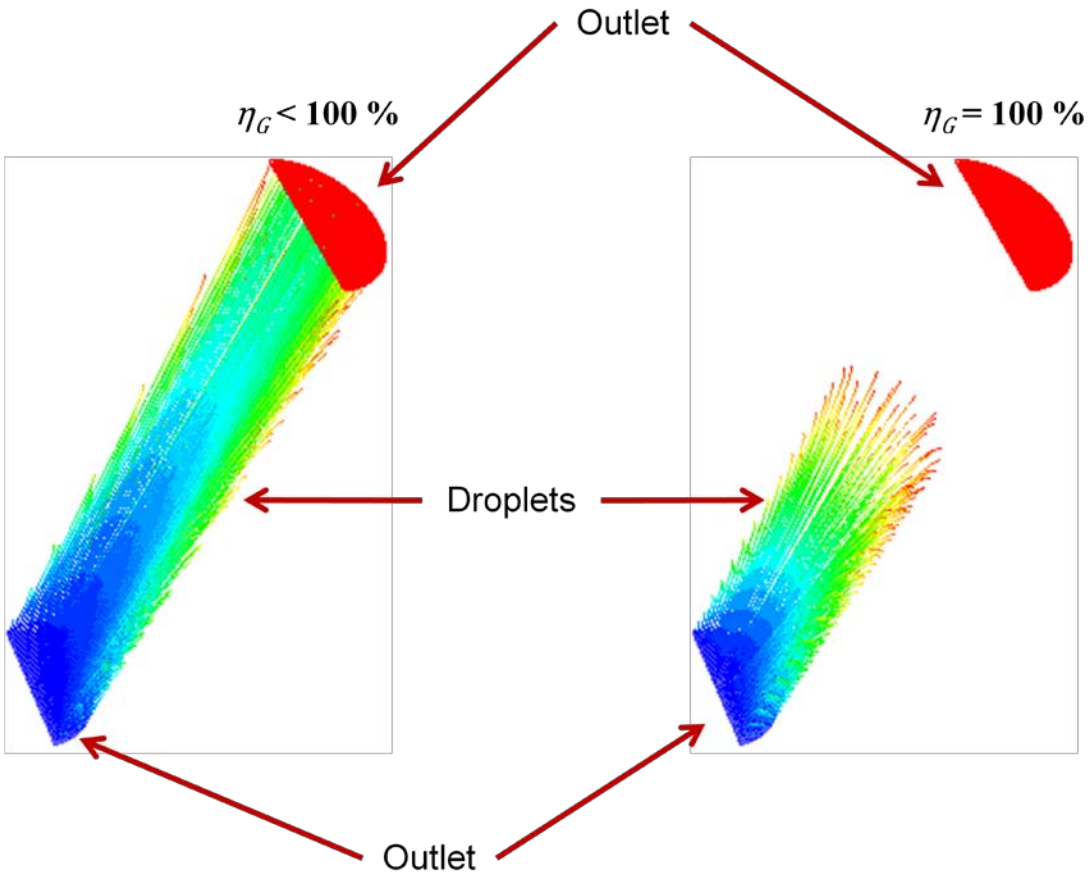

Figure 4-9 Droplets separation and collection

4.6.2.1. Effect of Applied Potential

The first case in the parametric study investigated the effect of applied electric potential on grade separation efficiency. Figure 4-10 shows five cases where a potential increase improved separation efficiency. The reason for this is that

increasing the electric potential leads to enhancement of the electric field intensity and an increase of charge density, which both enhance the charging process.

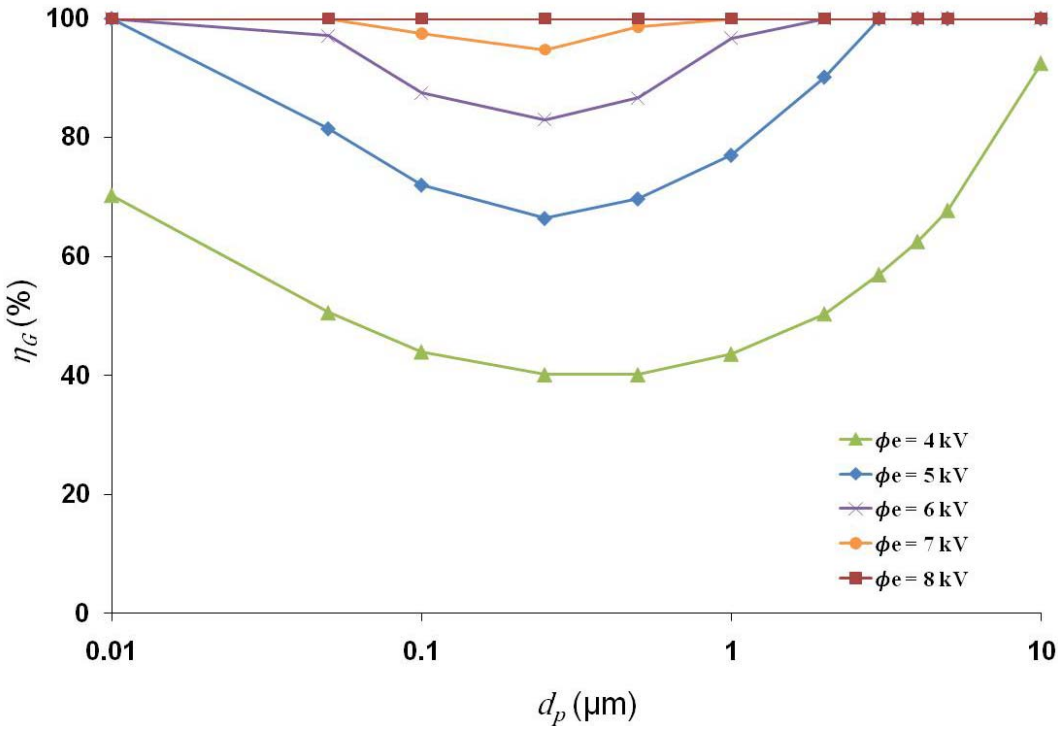

Figure 4-10 Applied electric potential effect on separation efficiency for five cases (u_f = 0.9 m/s, T_f = 300 K and L = 0.15 m)

The efficiency generally starts decreasing as the aerosol diameter size becomes greater than 0.01 µm, and then it starts increasing once diameter size passes 0.5 µm. The reason for this behavior is that the total charging is the summation of diffusion and field charging. The diffusion charging mechanism is the more dominant factor on small particles, while the field charging is more dominant on larger particles. However, the combined effects are less effective when the particle size is in-between. Looking at case (5) where the applied voltage is 8 kV, 100% efficiency was reached at all different aerosol diameters. The power consumption in this case was about 2.4 W.

4.6.2.2. Effect of Flow Velocity

The next case addressed the effect of flow rate on charging and collecting water aerosols. As expected, increasing the flow rate lowered the efficiency because of the shorter resident time available for the aerosols to receive charge, to travel to the collector electrode, and get trapped, as Figure 4-11 shows. For example, in case number (1), where the velocity was 0.3 m/s, the efficiency was 100% at all different diameter sizes, while for velocity 1.5 m/s the minimum efficiency decreased to 66% at diameter size 0.25 µm.

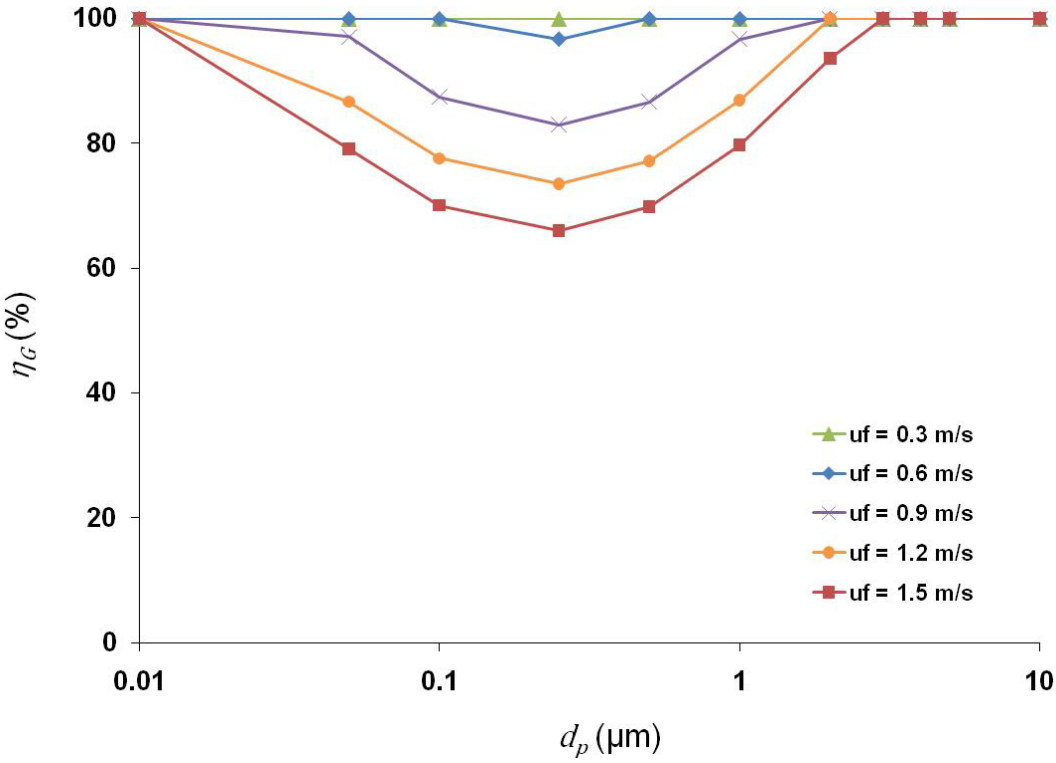

Figure 4-11 Flow velocity effect on separation efficiency for five cases (ϕ_e = 6.0 kV, T_f = 300 K and L = 0.15 m)

4.6.2.3. Effect of Flow Temperature

The third case investigated the effect of flow temperature on the separation efficiency. As mentioned earlier, in diffusion charging ions move due to Brownian

motion. Based on Equation (2-6), the flow temperature can affect this charging mechanism, the primary method of charging of small particles (i.e. < 0.5 µm.). The result of our study, presented in Figure 4-12, shows that over the investigated range of temperatures, the temperature influence is very low and is only on small particles. Overall, the effect of temperature on the separation efficiency can be disregarded without any substantial error. The temperature change is considered one of the thermophysical properties of gas and particles such as density and viscosity.

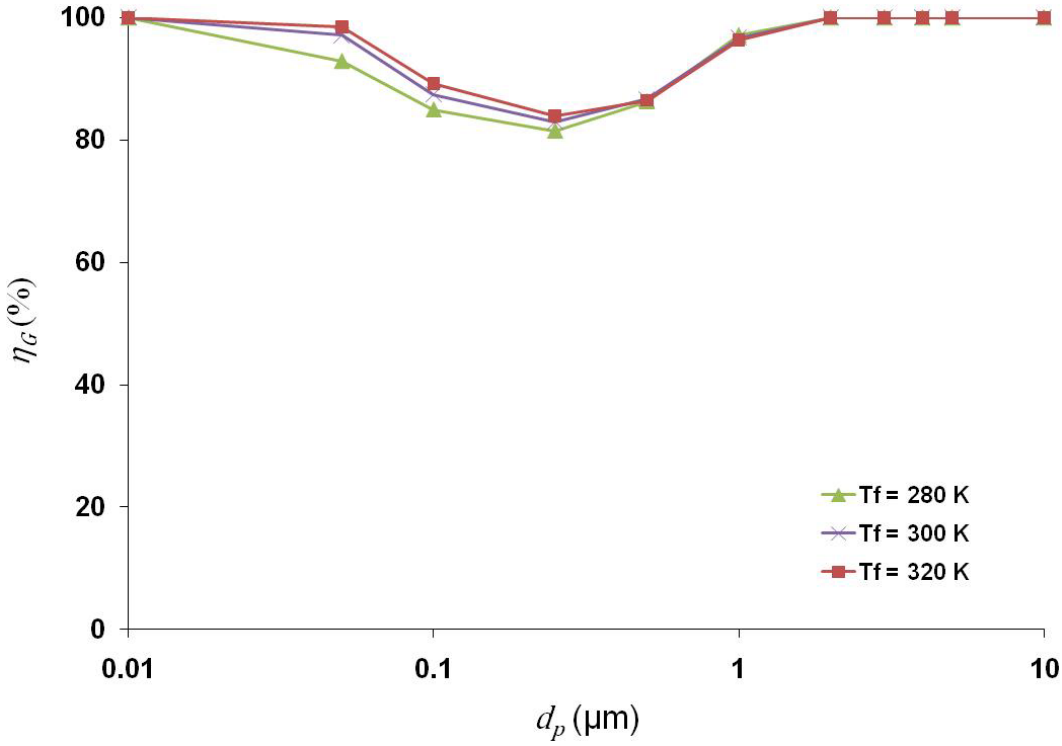

Figure 4-12 Flow temperature effect on separation efficiency for three (ϕ_e = 6.0 kV, u_f = 0.9 m/s and L = 0.15 m)

4.6.2.4. Effect of Separator Length

The forth case investigated the effect of the separator length on separation performance. Figure 4-13 shows that as the length increased, so did the separation efficiency. Increasing the length means increasing the aerosol residence time as well

as the collection area, which eventually enhances the performance of the separator. As seen there, the minimum efficiency varied from 61% for a 0.05 m separator to 100% for a 0.15 m separator. One must consider the increase in separator length results in higher power consumption by the electric field, thus there is an optimum length for a given system design.

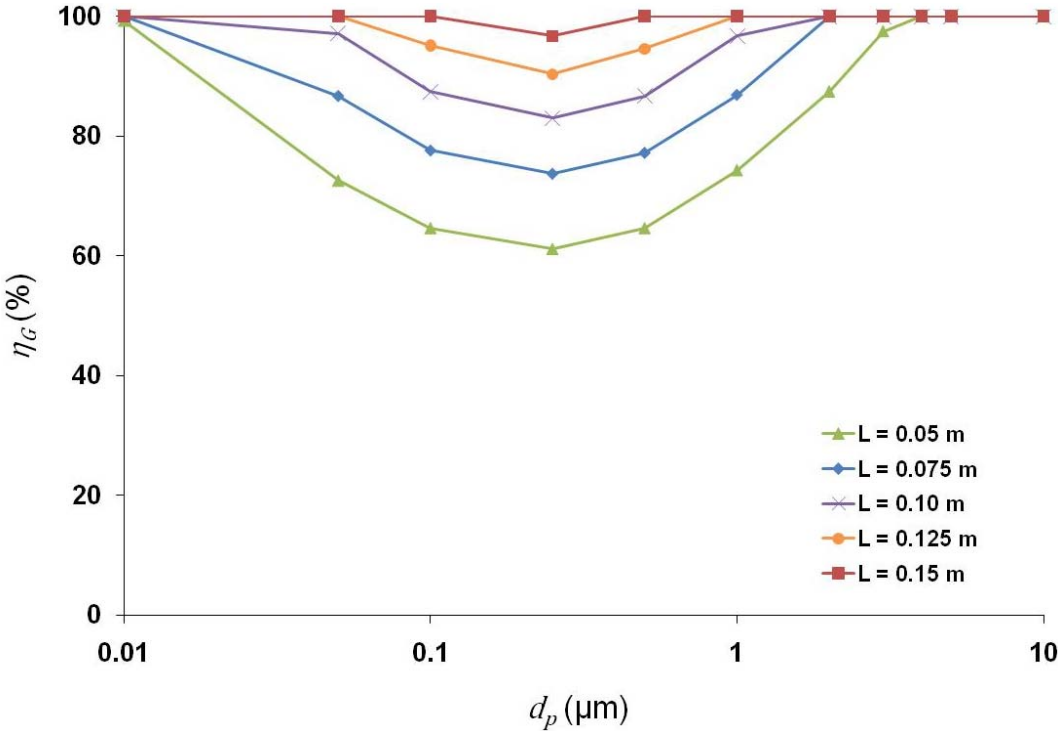

Figure 4-13 Separator length effect on separation efficiency for five cases (ϕ_e = 6.0 kV, u_f = 0.9 m/s, and T_f = 300 K

4.6.2.5. Effect of Relative Permittivity

The last case investigated the effect of relative permittivity of droplets on separation performance. Figure 4-14 shows a comparison study where in one case water droplets were injected in the computational domain under certain parameters of emitter polarity, flow temperature and velocity. Next, oil droplets were injected while

keeping these parameters fixed. The grade efficiency was calculated for each case as shown in the figure. Oil has low relative permittivity (2.0), where it is 80 for water.

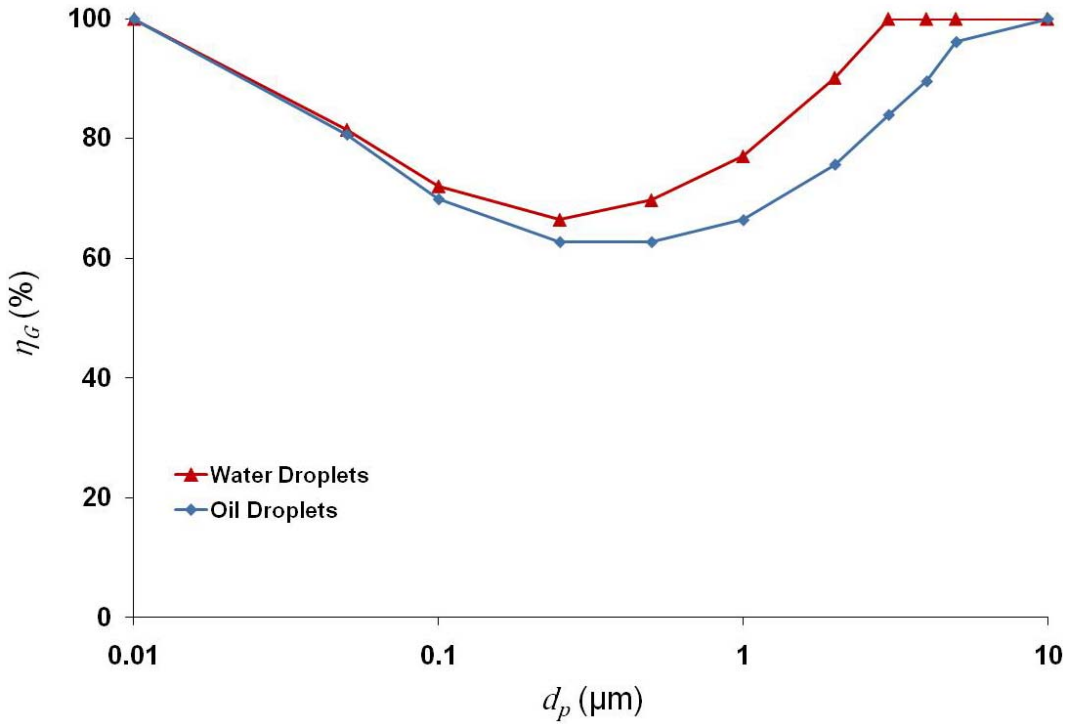

Figure 4-14 Comparison study in the effect of relative permittivity between water and oil droplets (ϕ_e = 5.0 kV, u_f = 0.9 m/s, T_f = 300 K, L = 0.15 m)

The effect of relative permittivity was changing depending on the size of droplets. For small droplet size of 0.01, there was no effect. Then as the particle size was increasing, the difference in efficiency between water and oil was increasing reflecting the effect of relative permittivity on the separation process. As the droplet size approached 10.0 µm, the difference was decreasing until it vanished.

Equation (2-7) can be used to explain the how relative permittivity was affecting the separation efficiency. First, the relative permittivity term appears only in the field charging mechanism. That's why the effect of relative permittivity is increasing as the droplet size decreased. Then the size of droplet becomes more

dominant than the relative permittivity once the droplet reaches certain size. The average efficiency for water and oil was 87 % and 81 %, respectively.

4.6.3. Mesh Study

A mesh study was conducted to investigate the independency of numerical model results with the number of computational cells. The study used the same meshing scheme, Tri-Pave, but with finer and coarser computational grids. Figure 4-15 shows a comparison between three cases that had the same input parameters with different cell numbers, where (a) was with decreased cell numbers, (b) was the standard case and (c) was with increased cell numbers. The average difference between cases (a) and (b) was about 0.5%, while the difference between cases (b) and (c) was about 0.8%. Therefore, for the parametric study in this paper it can be concluded that the results are independent of the cell number within ±1%. Thus, the computational cell number can be increased to improve the accuracy.

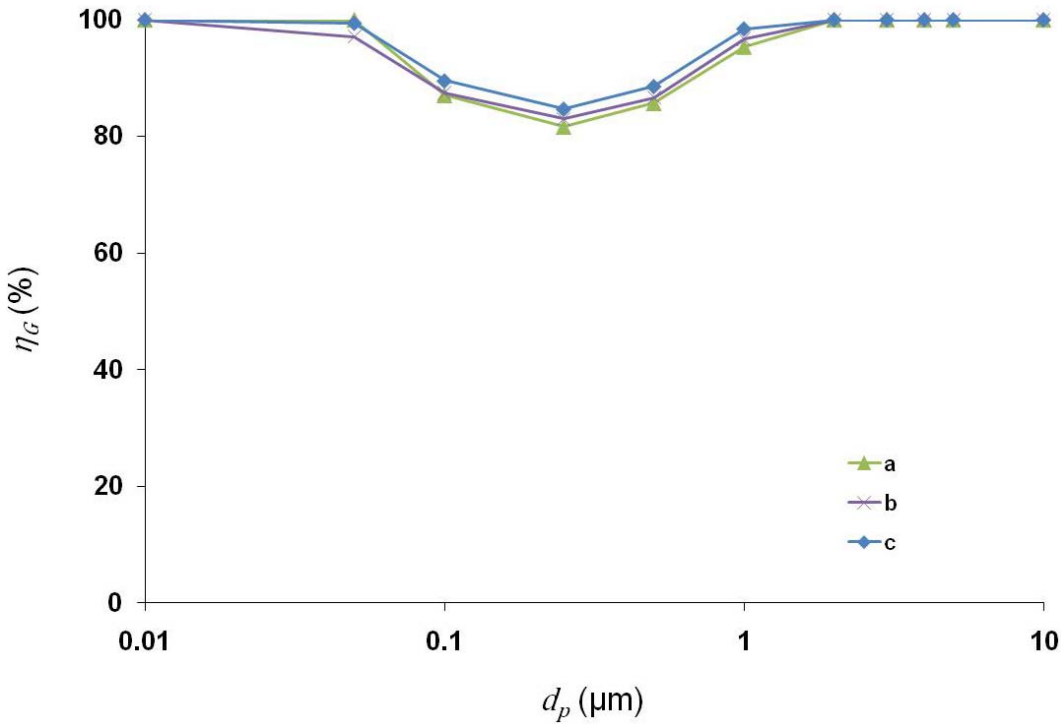

Figure 4-15 Mesh study comparison between three cases (ϕ_e = 6.0 kV, u_f = 0.9 m/s, and T_f = 300 K, and L = 0.10 m), with different computational cell numbers: a = 94655 cells, b = 487520 cells and c = 753840 cells

4.7. Conclusions

A numerical methodology based on the Lagrangian approach was outlined to study the performance of electrostatic aerosol separators in laminar flow. A parametric study on the performance of electrostatic separators was performed, and the influences of applied potential, fluid velocity, temperature and separator geometry were investigated. Also, the effect of relative permittivity of droplets was highlighted. Based on the results obtained, increasing the applied voltage and separator length directly increases the separation efficiency. On the other hand, the efficiency decreases as the flow velocity increases. The effect of flow temperature on the performance of the separator was found to be insubstantial. The relative permittivity affects the performance based on the droplet size. It has no effect for droplets that are

smaller than 0.025 μm or larger than 10 μm. Electrostatic separation can be considered an energy-efficient mechanism at low air velocities. Numerically, it can achieve 100% efficiency with reasonable power consumption, 2.4 W for a voltage of 8 kV and wire length of 0.1 m in the present study.

4.8. Summary

This chapter presented in detail the steps taken to model the effect of electrostatic forces on the charging and separation process. The numerical modeling results were compared with the analytical solutions to validate the numerical model. A mixture of air-water droplets was used in this model. The model was used to calculate the number of charges, which was compared against the Rayleigh limit to investigate the breakup of water droplets. Also, the model was used to conduct a parametric study that showed the effect of applied potential, flow velocity, flow temperature, separator length and relative permittivity on the separation efficiency.

CHAPTER 5: AIR-WATER SEPARATION—EXPERIMENTAL WORK AND RESULTS

5.1. Introduction

This chapter introduces a parametric study on air-water droplet electrostatic separation. The objective of the tests was to study the effect of electrostatic forces on the separation of fine water droplets in an airflow and to evaluate the role of key operating parameters on the performance of electrostatic separation. These parameters included applied voltage (ϕ_e), emitter polarity (+,-) and air flow velocity ($\mathbf{u}_f$).

The test section had a wire-tube geometry in which the wire was the emitter electrode (charged) and tube was the collector electrode (ground). A testing facility was constructed for separator testing. Instruments and measurements devices used in the setup will be described, and the testing procedures will be explained in detail. Finally, the results highlighting the performance of the separator will be presented along with a comparison study between experimental and numerical modeling results.

5.2. Test Setup

5.2.1. Test Section

The test section of the setup consisted of the electrostatic separator, used to separate water droplets from air stream. A wire-tube geometry was implemented for the separator design as shown in Figure 5-1. The wire acted as the emitter electrode (charged), while the tube performed as the collector electrode (ground). The wire had

a diameter of 0.08 mm and made out of stainless steel. The tube inside diameter was 20 mm and made out of copper. The lengths of wire and tube were both 150 mm.

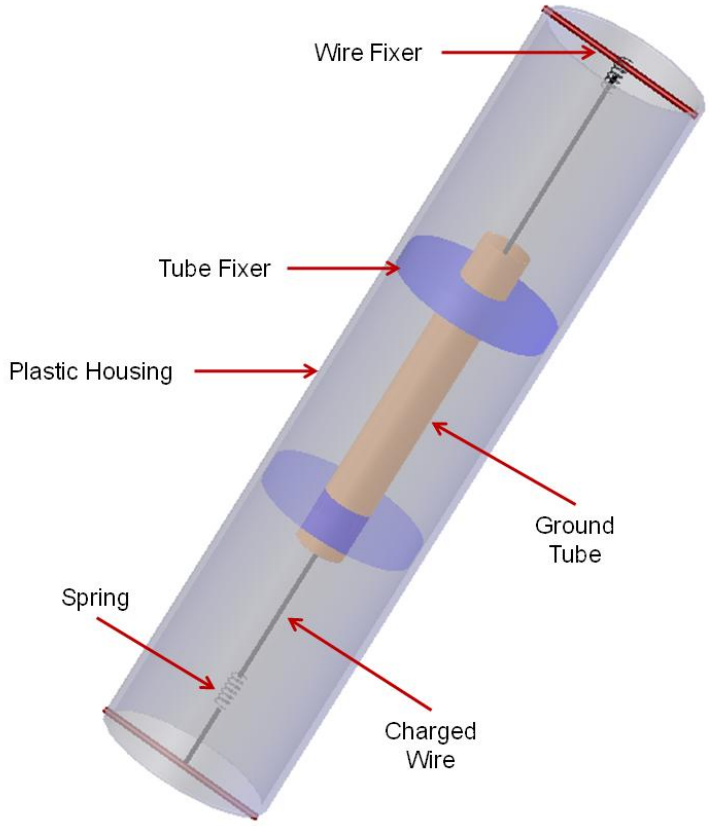

Figure 5-1 Schematic diagram of wire-tube electrostatic separator for air-water separation

The high water conductivity was considered in the design. Therefore, the wire ends were fixed at permissible distance from the ground tube to eliminate bridging or sparking between electrodes. A plastic tube (OD = 77 mm, ID = 71 mm and L = 350 mm) was used as a housing for the separator. The ends of the wire were fixed using the ends of the plastic housing as shown in the Figure 5-1. Two springs were used to keep the wire stretched. The ground tube was fixed inside the housing tube by friction. Two rubber tube fixers were used to mount the ground tube. The wire was centered in the middle of the ground tube. A portion of the wire surface area that was

not placed inside the copper tubes was insulated. Therefore, the length of the wire that was not insulated was the same as the length of the tube. A picture of the separator is shown in Figure 5-2. The corona glow at the wire surface when voltage is applied is shown in Figure 5-3.

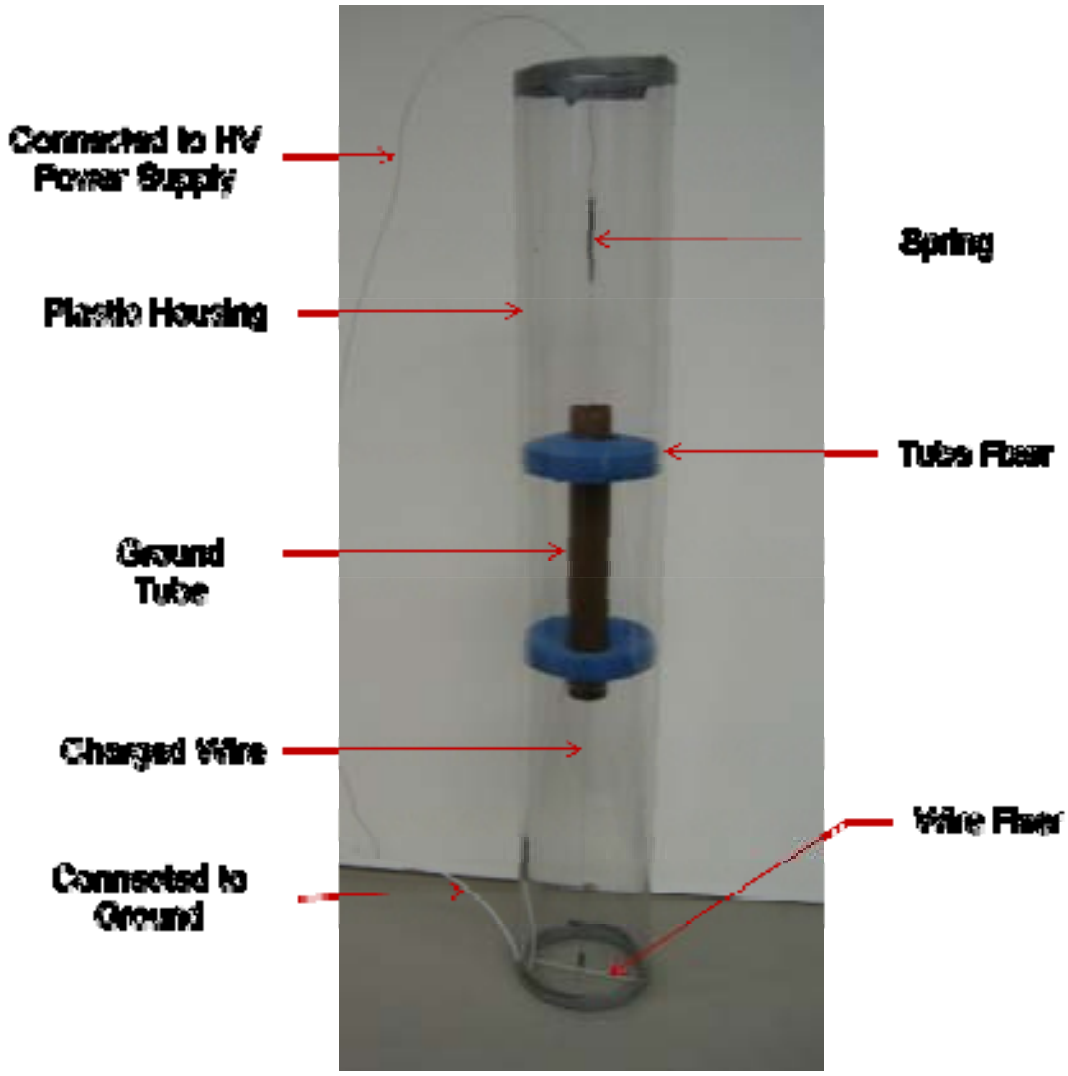

Figure 5-2 Wire-tube electrostatic separator for air-water separation

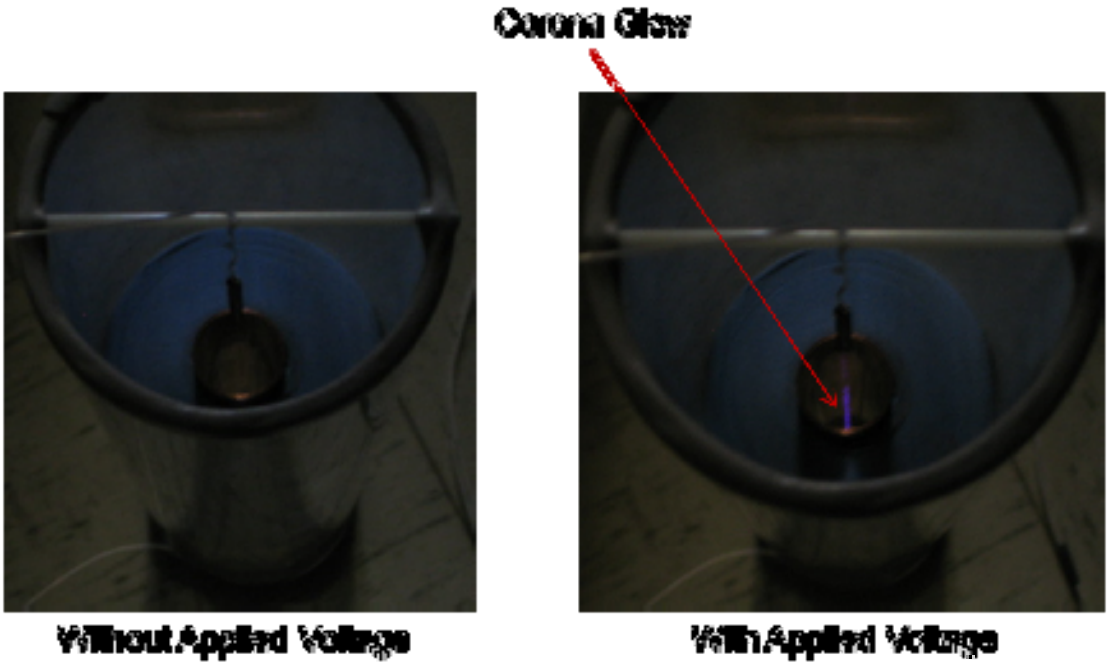

Figure 5-3 Corona glow at the wire surface

5.2.2. Test Loop

A closed loop setup was used to test the electrostatic separator performance. To ensure accurate results, the airflow had to be clean of any impurities. Therefore, all of the test setup elements such as pipes, fittings and other circuit elements were selected from nondegrading materials. Figure 5-4 shows a schematic of the closed loop test setup.

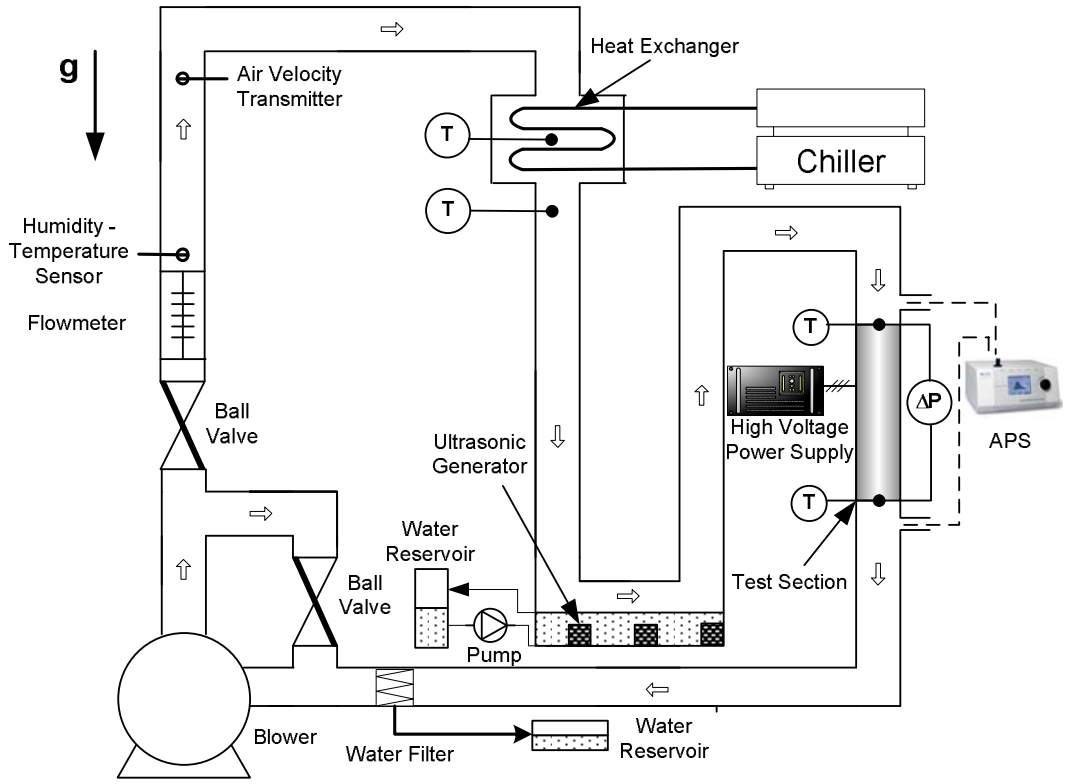

Figure 5-4 Schematic sketch of the closed loop test setup

The connecting tubes in the test setup were PVC pipes (ID = 77.0 mm). The other components in the test setup can be divided into three categories: air supply components, water supply components, and instruments and measurement components, as listed below.

- Air supply components:
    1. Air blower (Gast, Inc.)
    2. Ball valve (Spears, McMaster-CARR, Inc.)
    3. Heat exchanger
    4. Chiller (Neslab, Inc., HX-150)
- Water supply components:
    1. Low pressure head gear pump, 250 ml/min, (Ismatec, Inc., MCP 2)

2. Water reservoirs
    - Distilled water reservoir for the production of water droplets
    - Water reservoir to collect remaining water before entering the blower
3. Ultrasonic moisture generators, 5 units, 1500 ml/hour (Mico, Inc.)

- Instruments and measurement components:

1. Variable area flowmeter (Fischer Porter, Inc.)
2. Humidity-temperature sensor (Vaisala, Inc., HMI 38)
3. Air velocity transmitter (Dwyer Instruments, Inc., 641RM-12-LED)
4. Thermocouples (Omega, Inc., T type)
5. Differential pressure transducer (Validyne Engineering, Inc., P855 D)
6. Weight scale*
7. Aerodynamic particle sizer (TSI, Inc., 3321)
8. Data acquisition switch unit* (Agilent Technologies, Inc., 34970A)
9. DC high-voltage power supply
    - Positive polarity (0-60 kV, Glassman High Voltage, Inc., ER60P5)
    - Negative polarity (0-30 kV, Glassman High Voltage, Inc., EK30N20)

All items with (*) are not shown in the schematic of the test loop.

Starting from the blower, the airflow was adjusted using the ball valves. Then the airflow passed through the flowmeter to the heat exchanger. Before entering the heat exchanger, humidity, temperature and velocity of air were measured. A chiller was used to control the temperature of air to the desired temperature. The air then flowed to the ultrasonic generator unit and carried water droplets to the test section. The droplet concentration was measured at the inlet and outlet of the test section. The

pressure drop and temperature were monitored across the separator. Finally the air flowed back to the blower.

A filter was used between the test section and blower to prevent water droplets that may exist in the flow from entering the blower. The collected water was then drained into a water reservoir. This will also help capture any particles or contamination that exists in the loop that may exist at the beginning of tests.

The heat exchanger used in the setup was an automotive evaporator. To use the heat exchanger as part of the setup, it had to be insulated. Therefore, layers of installation were added to accommodate the high pressure inside the evaporator. Also, thermocouples were attached to the evaporator to measure the temperature; see Figure 5-5. A leakage test was conducted to ensure the evaporator vessel was secured against any leakage.

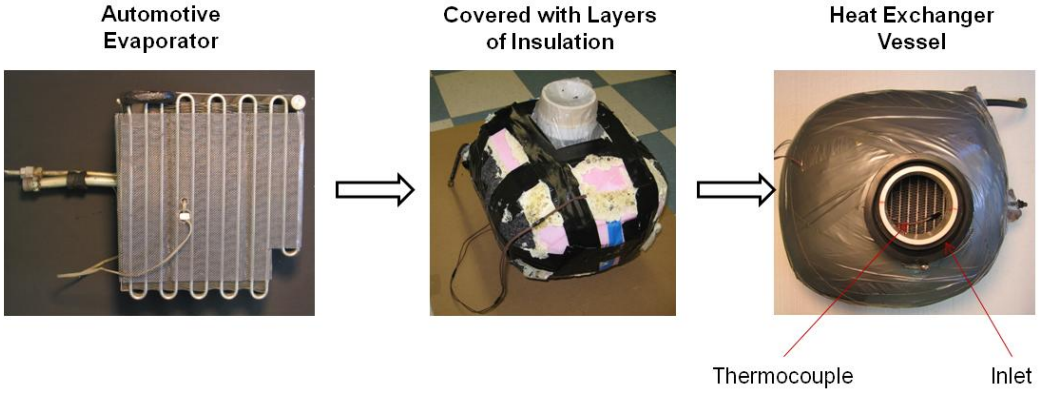

Figure 5-5 Heat exchanger vessel

Ultrasonic generation method was used to produce water droplets, for which five ultrasonic generators were used. They were mounted in a water pool unit as depicted in Figure 5-6.

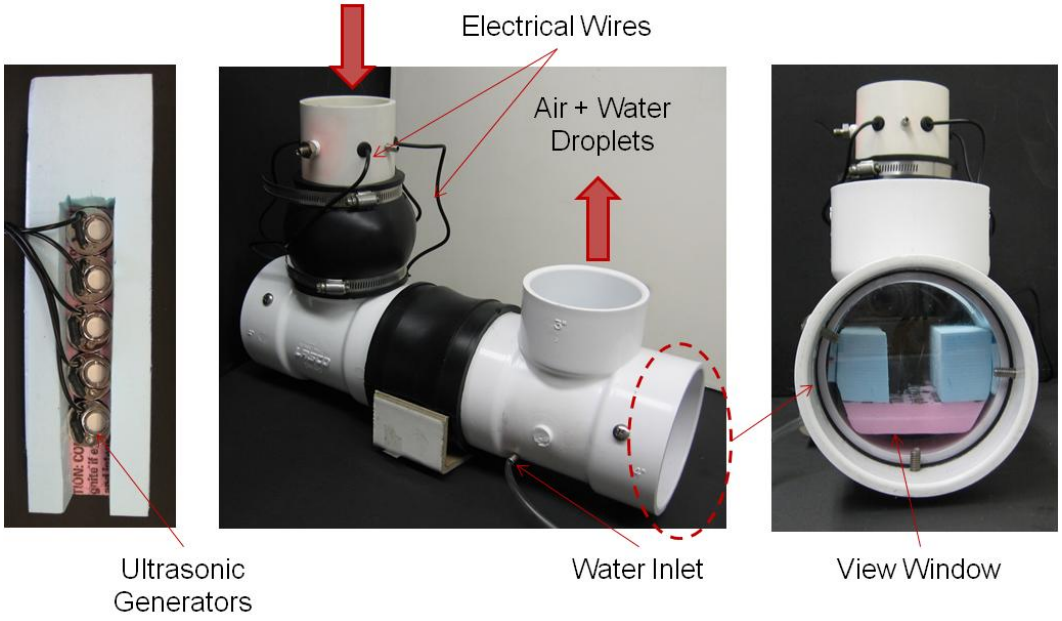

Figure 5-6 Ultrasonic generator unit

The performance of this type of generator depends greatly on the water level above its diaphragm, so it was essential to keep the water elevation relatively constant. To do so, the water flow was circulated to the unit through two ports using the gear pump. The water was fed to the unit through the bottom port, where the excess water was drained from the other port on the side. Both inlet and outlet water lines were connected to the same reservoir. To measure the amount of water injected, the weight of the reservoir was constantly monitored.

The actual test setup is shown in Figure 5-7, in which the airflow direction is presented by arrows.

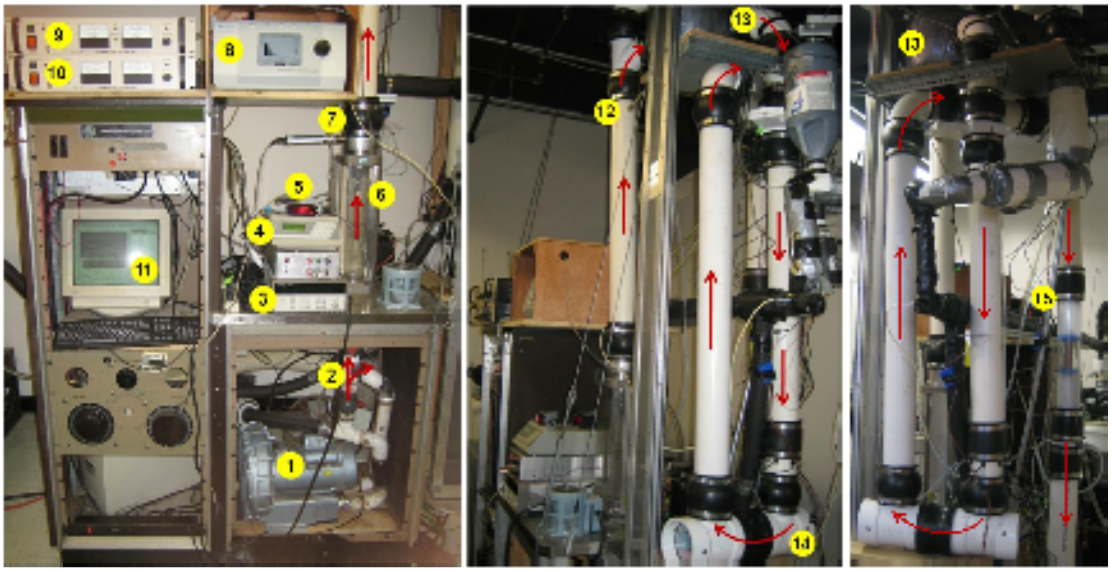

Figure 5-7 Air-water droplet separation test setup, where:

1. Blower	**2. Ball Valves**	**3. DAS Unit**
4. Humidity Sensor Reader	**5. AVT Reader**	**6. Flowmeter**
7. Humidity Sensor Probe	**8. APS Unit**	**9. HV Power Supply (-)**
10. HV Power Supply (+)	**11. Computer**	**12. AVT Probe**
13. HX Vessel	**14. Water Pool**	**15. Electrostatic Separator**

The flow direction through the electrostatic separator was changed to study the effect of gravity on separator performance and the amount of collected droplets of water. In the original orientation the air flowed was upward. Then the separator position was moved to the other line to redirect the airflow passing downward through the separator, as depicted in Figure 5-8. More detailed analysis about the effect of the flow direction is presented in section (5.6.3).

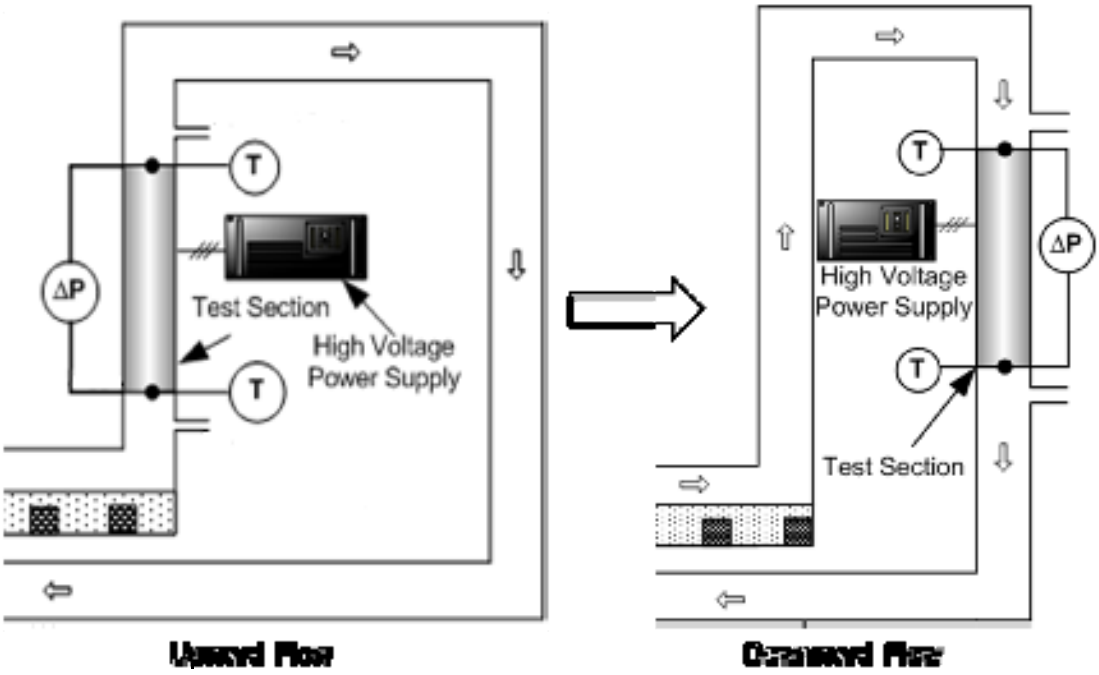

Figure 5-8 Changing flow direction inside the separator

5.3. Equipment, Instruments and Measurement Devices

This section will highlight some of the main instruments and devices used in the test loop.

- **Aerodynamic Particle Sizer (APS)**

The purpose of this device (shown in Figure 5-9) was to measure water droplet concentration and size at the inlet and outlet of the electrostatic separator. It measures droplet concentration based on the total number ($Conc._{No}$) and total weight ($Conc._{Wt}$). Based on the concentration, the efficiency and performance of the separator can be evaluated. The aerodynamic particle sizer (APS) can measure a concentration up to 10,000 /cm^3. This device can also measure droplet sizes ranging from 0.1-20 µm.

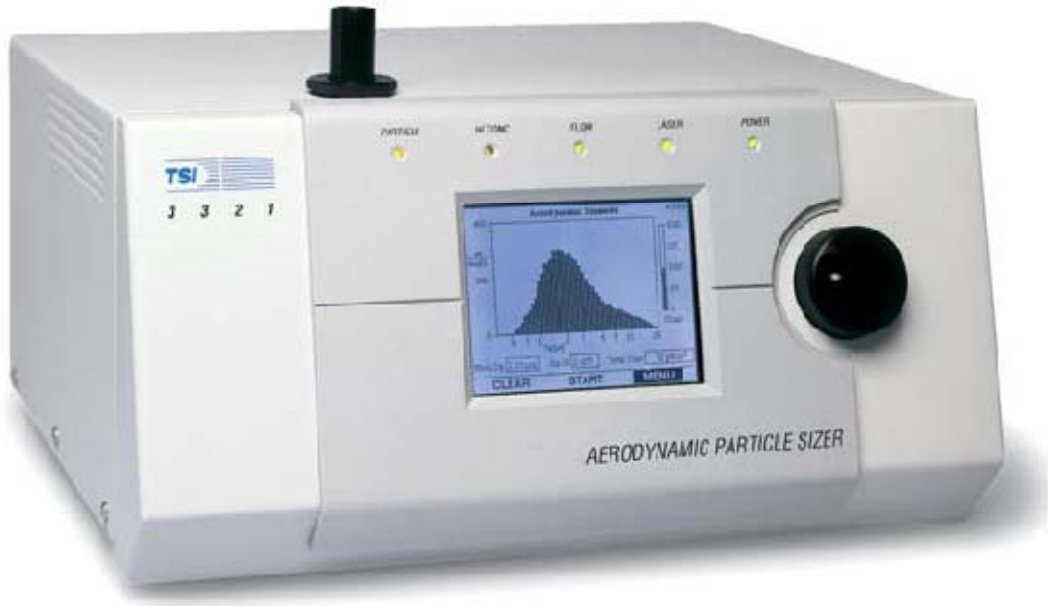

Figure 5-9 Aerodynamic particle sizer (TSI-3321), adopted from (TSI, Inc. 2009)

The APS operates based on continuous sampling from the flow. It uses a double-crest optical system to detect the occurrence of particle coincidence (Hairston, et al. 1996). Then the APS is calibrated to measure the particle size through measuring the time-of-flight during which the particle is accelerated between the double-crest layers, Figure 5-10.

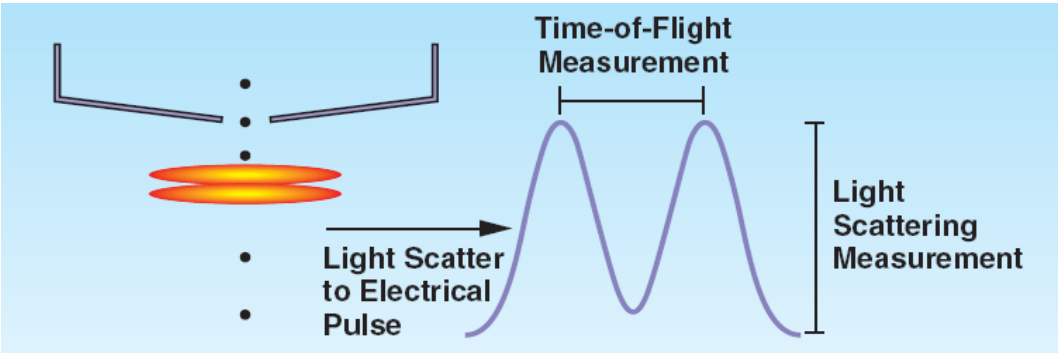

Figure 5-10 APS uses an optical system to calculate time-of-flight, adopted from (TSI, Inc. 2009)

The operation of the APS starts when the aerosols are accelerated to the inlet of the device. The total flow rate the device can pump is 5 L/min. The flow then is

divided into two separate paths: 4 L/min goes through a double-filtered region, while the other 1 L/min goes through unfiltered. The two flows rejoin just before the optical detection area, as shown in Figure 5-11. Table 5-1 shows the main specifications, features and allowable operating conditions of the APS (TSI-3321). The device is suitable for measurement of relatively low concentrations of aerosols. For 0.5 µm and 10 µm diameters, the maximum concentration to be measured by the APS is about 1000 particles/cm^3 and 10,000 particles/cm^3, respectively.

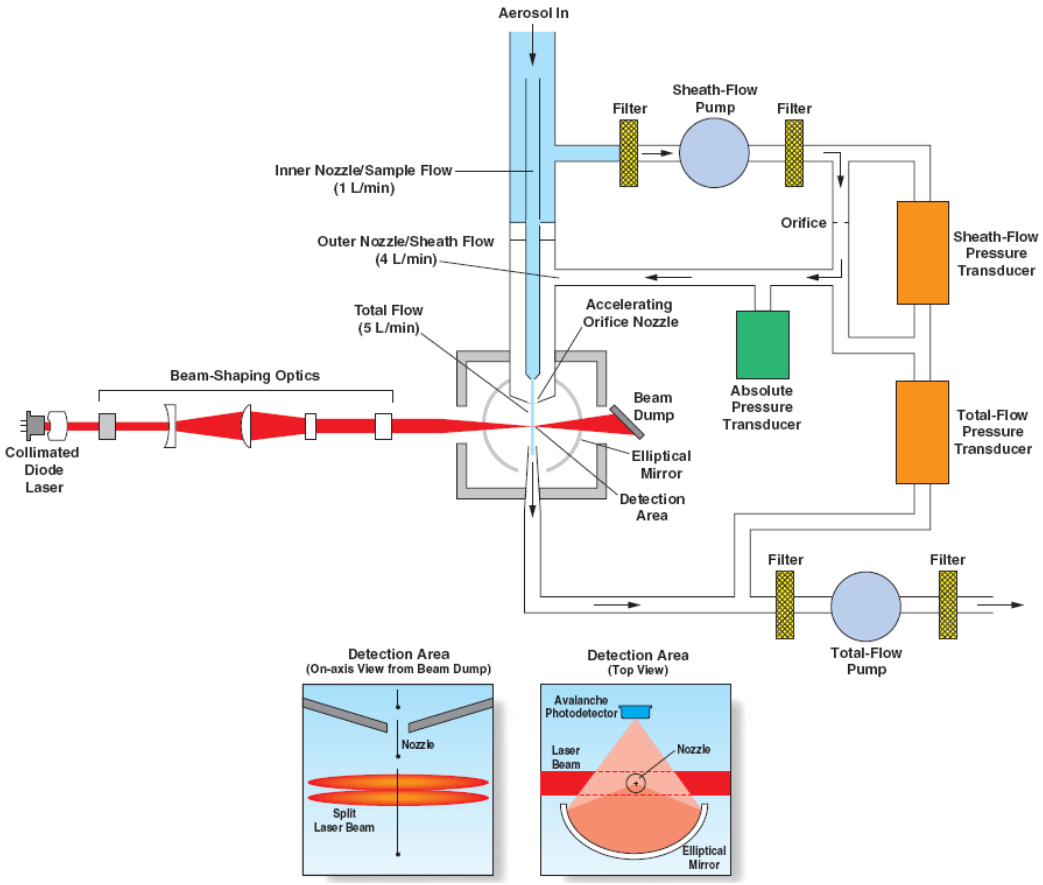

Figure 5-11 Schematic of APS operation, adopted from (TSI, Inc. 2009)

Table 5-1 Aerodynamic Particle Sizer (TSI-3321) Specification and Feaures

Particle size range	0.1-20 µm
Particle concentration	0.001-10,000 particles/cm^3
Accuracy	±10% @ 10,000 particles/cm^3
Size resolution	0.02 µm @ 1.0 µm 0.03 µm @ 10 µm
Maximum processing rate	> 200,000 particles/sec
Operating temperature	10-40 ^oC
Operating pressure	1 bar
Operating humidity	10-90 % (R.H.)

- **Air Velocity Transmitter**

This device measures the velocity of an airflow. It uses a heated mass flow sensor that allows for precise velocity measurements at various flow rates and temperatures. It has its own velocity reader, as shown in Figure 5-12, and also has an output voltage to transmit signals to the data acquisition system. The device is moderately accurate and measures a wide velocity range, as shown in Table 5-2. The probe was placed in the center of the tube such that it measured the maximum velocity of air.

Figure 5-12 Air Velocity Transmitter (Dwyer-641), adopted from (Dwyer, Inc. 2009)

Table 5-2 Air Velocity Transmitter (Dwyer-641) Specifications and Feaures

Velocity range	1.25-75 m/s
Temperature limits	-40-100 ^{o}C
Pressure limits	6.9 bar
Humidity limit	Non condensing
Resolution	0.05 m/s @ 75 m/s
Accuracy	±3% (0-50 ^{o}C) ±4% (-40-0 ^{o}C and 50-100 ^{o}C)

- **Other Equipment and Devices**

Other instruments and devices are presented in Table 5-3 along with their specifications, features and operational conditions ranges.

Table 5-3 Instruments and Measurement Devices

Device	Type	Manufacturer (Model)	Specifications
Differential pressure transducer	Diaphragm	Validyne Engineering, Inc. (P855D)	• Range: 0-1.4 k Pa • Accuracy: ±0.1 Pa
Thermocouple	T-Type	Omega, Inc.	• Range: -200-350 °C • Error: ±0.5 °C
Humidity sensor		Vaisala (HMI38)	• Range: 0-100 % R.H. • Error: ±5.4 % R.H.
Flowmeter	Rotameter	Fischer Porter	• Range: 0-026 m^3/s • Accuracy: 0.2%
Data acquisition switch unit		Agilent Technologies, Inc. (34970A)	• Thermocouple Accuracy: ±1.0 ^oC • DC voltage Accuracy (10 V): ± (0.0035 % of reading + 0.0005% of range)
High voltage power supply	Positive polarity	Glassman High Voltage, Inc. (ER60P5)	• Output Voltage: 0-60 kV • Output Current: 0-5 mA • Accuracy is 1% of rated + 1% of setting
High voltage power supply	Negative polarity	Glassman High Voltage, Inc. (EK30N20)	• Output Voltage: 0-30 kV • Output Current: 0-20 mA • Accuracy is 0.5% of rated + 0.2% of setting

5.4. Testing Procedures

The following testing procedures were followed for each test to insure the accuracy and repeatability of the results:

- Calibrate in advance the test setup instruments such as differential pressure transducer, air velocity transmitter and humidity-temperature sensor; see section (5.5);

- Turn on the data acquisition unit and monitor temperature output reading;
- Turn the blower on and adjust the flow rate using the ball valves;
- Turn on the chiller to obtain the desired temperature;
- Turn on the APS to get the temperature to a steady state;
- Turn on the ultrasonic generators after turning on the water pump;
- Monitor the injected amount of water by measuring the water reservoir and time;
- Let the set setup loop reach steady state condition in terms of temperature and water droplet concentration;
- Take measurements of water droplet concentration at the separator inlet;
- Increase voltage gradually and stop just before reaching breakdown voltage;
- Take measurements of water droplet concentration at the separator for different values of applied voltage once it exceeds the onset voltage;
- Analyze the collected data.

5.5. Instrument Calibration

- **Differential Pressure Transducer**

The calibration was performed using a U-tube manometer and water as the liquid. The pressure transducer analog output was connected to a multimeter. Once a pressure difference was established in the port that connects the transducer to the U-tube manometer, the output signal corresponding to the pressure difference was measured. An output voltage was obtained from the multimeter that corresponds to the elevation change. Figure 5-13 shows the calibration curve for the pressure transducer.

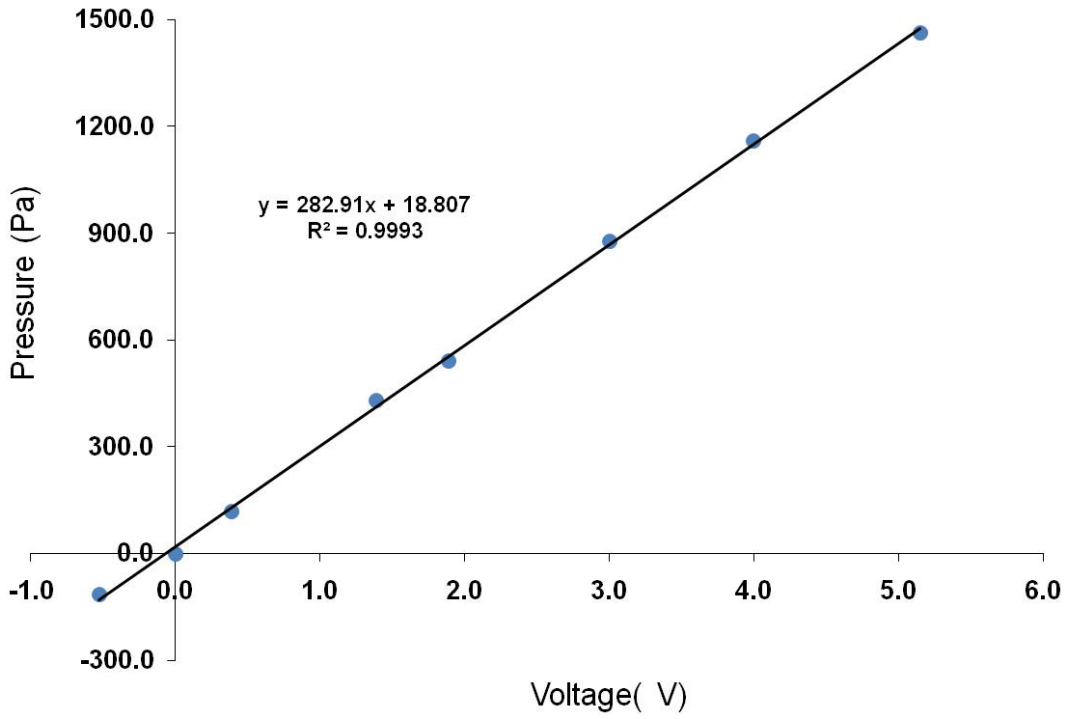

Figure 5-13 Calibration curve for the differential pressure transducer

- **Air Velocity Transmitter (AVT)**

The AVT was calibrated with a flow meter. The AVT was connected to a multimeter to measure the output voltage. Since the AVT probe was mounted in the center of the tube, it measured the maximum flow velocity, $\mathbf{u}_{f,max}$. On the other hand, the flow meter measured the average flow velocity, $\mathbf{u}_f$. The relation between these two velocities depends on the flow regime. Equations (5-1) and (5-2) show this relation.

$$\mathbf{u}_{f,max} = 2\,\mathbf{u}_f \text{ (Laminar flow)} \qquad \textbf{(5-1)}$$

$$\mathbf{u}_{f,max} = \frac{(m+1)(2m+1)}{2m^2}\,\mathbf{u}_f \text{ (Turbulent flow)} \qquad \textbf{(5-2)}$$

where m is a weak function of Reynolds number. Figure 5-14 shows the calibration curve for velocity profile obtained by the AVT and flow meter. Figure 5-15 shows the

ratio between maximum and average velocities, which is the constant term in Equation (5-2), $\frac{(m+1)(2m+1)}{2m^2}$. This term is equal to 1.2 for the range of velocities used in this calibration.

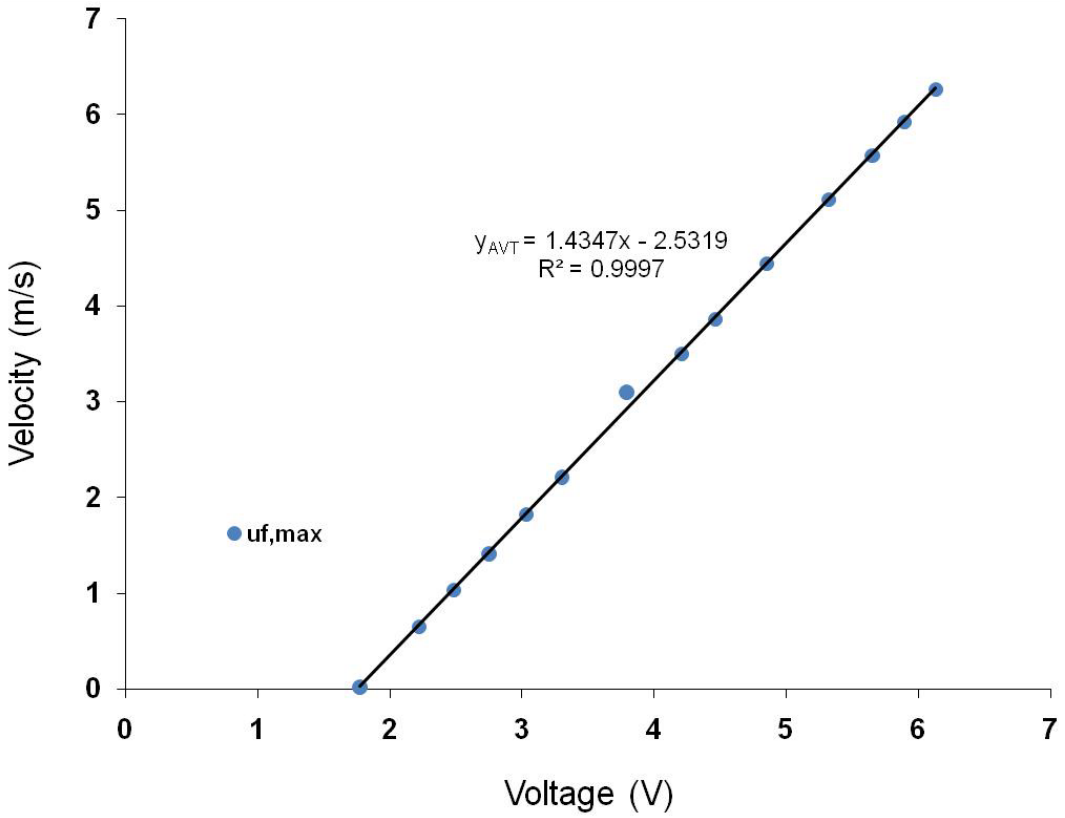

Figure 5-14 AVT calibration curves

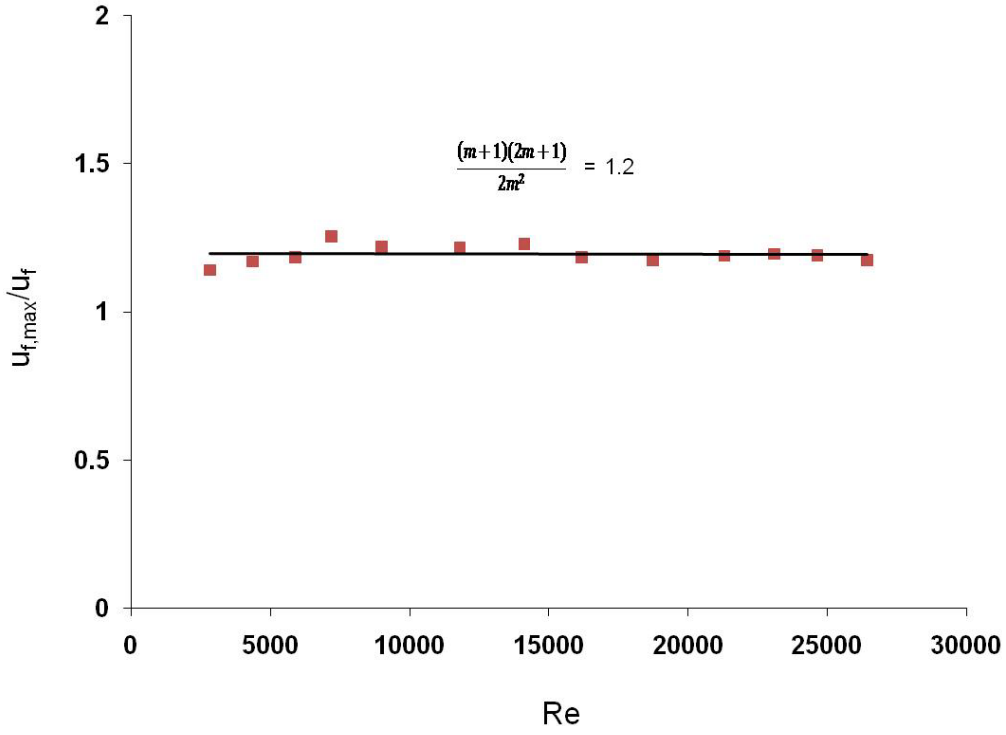

Figure 5-15 Ratio of maximum velocity to average velocity

- **Humidity-Temperature Sensor**

Four different saturated solutions with known relative humidities were used to calibrate the humidity sensor. The solutions used were K_2SO_4, $MgCl_2$, LiCl and NaCl. The solution's relative humidity is a function of temperature. The sensor can also measure temperature. The device comes with an output reader to read both relative humidity and temperature. The calibration process was as follows:

1. Leave the humidity sensor and solution chambers in the same room and wait for four hours until their temperatures reach equilibrium.
2. Remove the filter cap from the probe.
3. Insert the sensor probe into the solution chamber and wait for ten minutes before taking the reading.

4. Since the temperature is known, then the relative humidity of the solution is known.
5. Adjust the resistance of the probe to the corrected reading and measure output voltage through a multimeter.
6. Repeat steps 3-5 with different salt solutions.

Figure 5-16 and Figure 5-17 show the calibration curves for the humidity sensor and temperature, respectively.

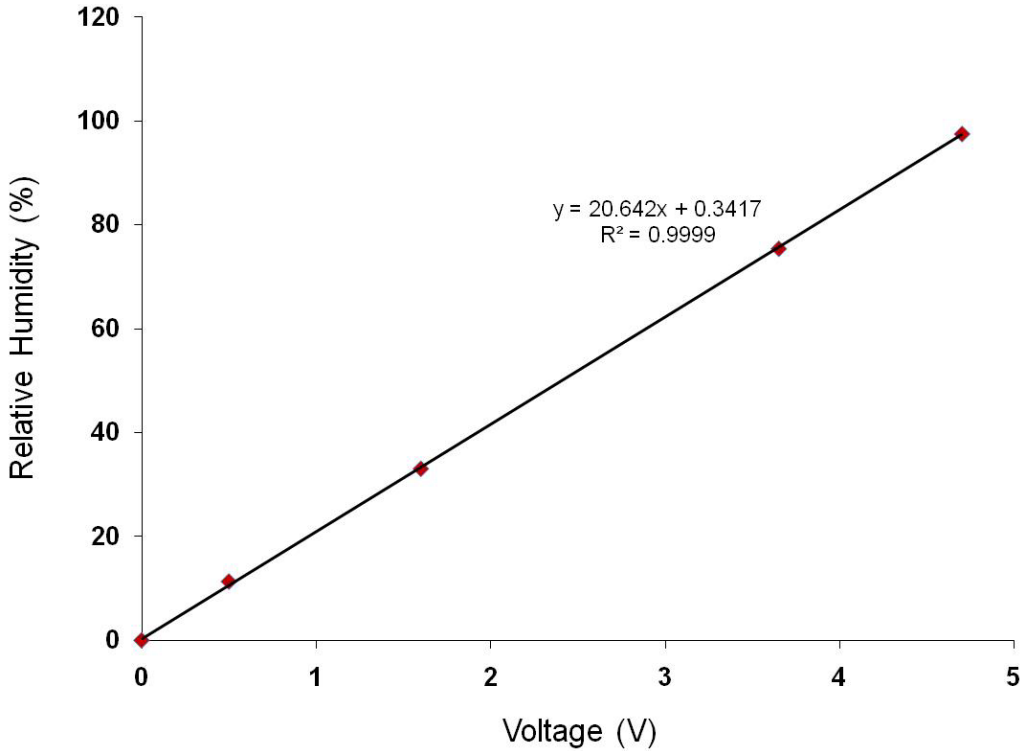

Figure 5-16 Humidity sensor calibration curve (T_{room} = 21.0 ^{o}C)

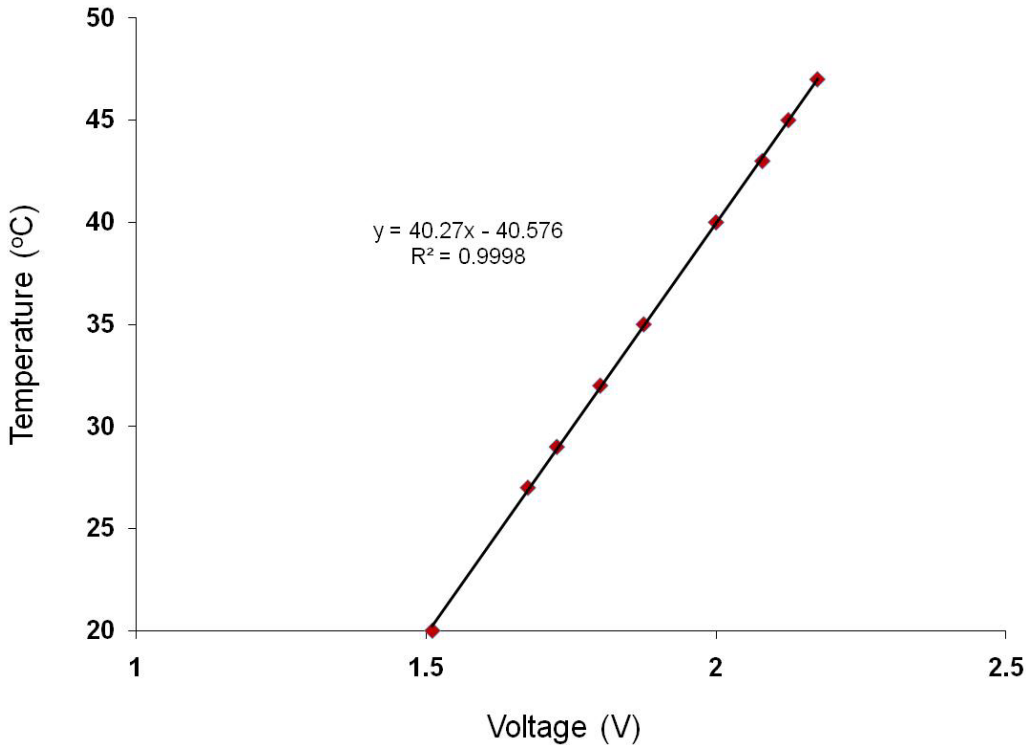

Figure 5-17 Temperature sensor calibration curve

5.6. Results and Discussion

The results will be divided into six sections. The first part will highlight the effect of temperature difference between the test section and the APS unit and how this difference decreases the accuracy of the obtained results. The second part will show the water droplets distribution that was produced by the ultrasonic generation and measured by the APS. The third part will investigate the effect of flow direction on the separator performance. The forth part will present the efficiency and performance of the electrostatic separator in removing water droplets from airflow. The fifth part will study the effect of electrostatic force in the pressure drop across the separator. Finally, in the last part, selected experimental work results will be compared against the numerical study results that were presented in Chapter 4.

5.6.1. Temperature Effect on the Particle Sizer Concentration Reading

The effect of flow temperature on the performance of the electrostatic separation was one of the study parameters in this work. However, the water droplets evaporated during measurements when the temperature of the APS was higher than the separator temperature. The APS operates between 30-33 ^{o}C, and the temperature can be obtained using the front panel control knob and built-in display.

The evaporation of the droplets was verified by plotting the particle weight concentration vs. the temperature difference between the inlet or outlet of the separator and the APS unit, as shown in Figure 5-18. To conduct the test, all parameters were fixed, including airflow velocity and water droplet injection, except the temperature. At the start of the test, the temperature was set to a low temperature (5 ^{o}C). Then the temperature was increased gradually. The data for the water concentration at the separator inlet was collected at each temperature setting. Between each temperature setting, enough time was allowed for the loop to arrive at steady state condition. The collected data were repeatable within the accuracy of the APS, as shown in Figure 5-18.

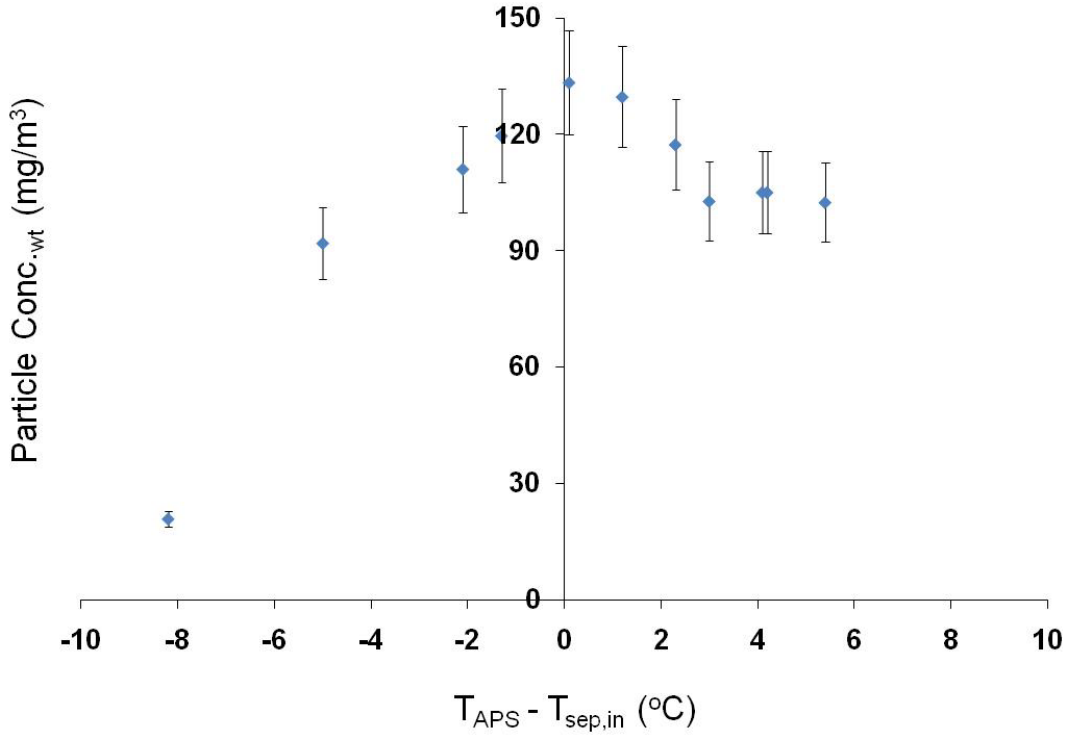

Figure 5-18 Temperature difference effect on water droplets measurements ($\dot{V}_{air}$= 0.01 m^3/s, $\dot{V}_{water}$ = 4.5 ml/min)

Also, a comparison between two cases is shown in Figure 5-19; in one case there is a temperature difference between APS (T_7) and the test separator (T_3), and in the other case their temperature is the same. The data plotted on the psychometric chart show that water evaporated when moist air went from T_3 to T_7. The temperature at the separator inlet (T_3) was obtained by assuming the air to be saturated (RH = 100 %) after leaving the heat exchanger. Once the air passes through the water droplet region, it will carry the water droplets, which will be added as humidity ratio. When the airflow moves to the APS, all properties are constant except the temperature. The droplets evaporate when they move from T_3 to T_7. Therefore, the difference between them should be kept as low as possible.

Given these results, the test loop should be operated at a temperature close to the APS temperature to limit the evaporation of the droplets, so T_3 and T_7 values should be close to each other.

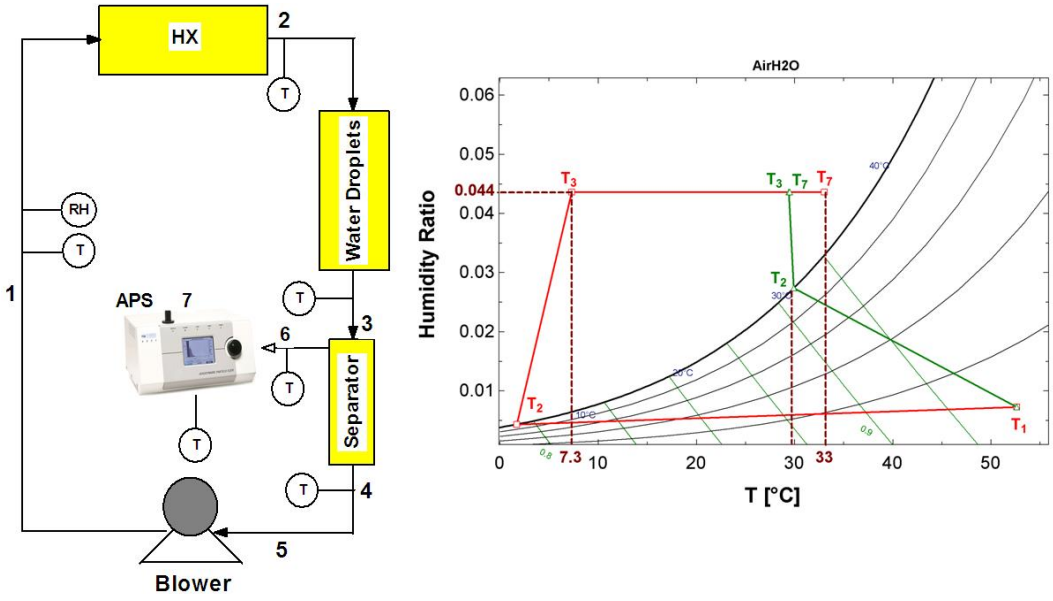

Figure 5-19 Water evaporation on the psychometric chart showing two cases: T_3 = 7.3 °C, and T_3 = 30 °C while T_7 = 33 °C

5.6.2. Generation of Water Droplets

The ultrasonic generation method was used to produce water droplets. The droplets produced have wide range of sizes—what is known as polydisperse droplets. Hence, it was more appropriate to evaluate the performance based on the concentration of total weight of particles ($Conc._{Wt}$) rather than on the total number ($Conc._{No}$). As mentioned in section (5.3), the APS can measure the two types of concentrations: concentrations based on the total number of particles ($Conc._{No}$) and concentrations based on the weight of particles ($Conc._{Wt}$).. Therefore, the total efficiency (η), Equation (5-3), will be used instead of the grade efficiency (η_G) that is presented in Equation (4-1) to evaluate the total efficiency of the separator.

$$\eta = 1 - \frac{\text{Wt. of Escaped Particles}}{\text{Wt. of Injected Particles}} \qquad \textbf{(5-3)}$$

The results for the measured water droplet concentrations were conducted at the separator inlet. Figure 5-20 presents the droplet concentrations generated by the ultrasonic generators measured at the inlet. The water injection rate, measured by scaling the water reservoir, was 4.5 ml/min. The water concentration measured by the APS for one of the cases was 282 mg/m^3. The big difference between the injected and measured water concentrations was due to the large water droplets produced, which were out of the APS range. The droplets' mean diameter was 3.6 µm.

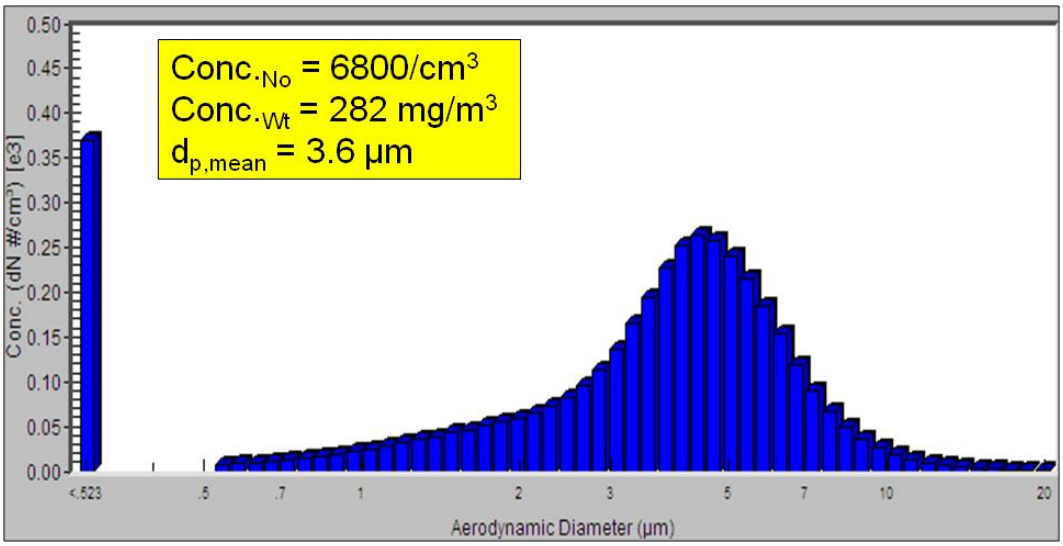

Figure 5-20 Water droplet concentrations generated by ultrasonic generators at the inlet (5 units, $\dot{V}_{air}$ = 0.01 m^3/s)

5.6.3. Flow Direction Effect on Separator Performance

Before proceeding to testing results, the effect of flow direction on performance should be discussed. The electrostatic separator was designed to be tested in the vertical position. When the airflow direction was upward (i.e., against gravity), the water gradually collected on the collector surface as scattered water

droplets. Once joined, they formed bigger droplets with a tendency to slide down due to gravity. Since the flow direction was upward, the droplets were stopped from moving and remained at the surface, as shown in Figure 5-21. Once this happened, bridging between the electrodes was initiated due to the high conductivity of water. Therefore, long periods testing could not be conducted while airflow direction was upward.

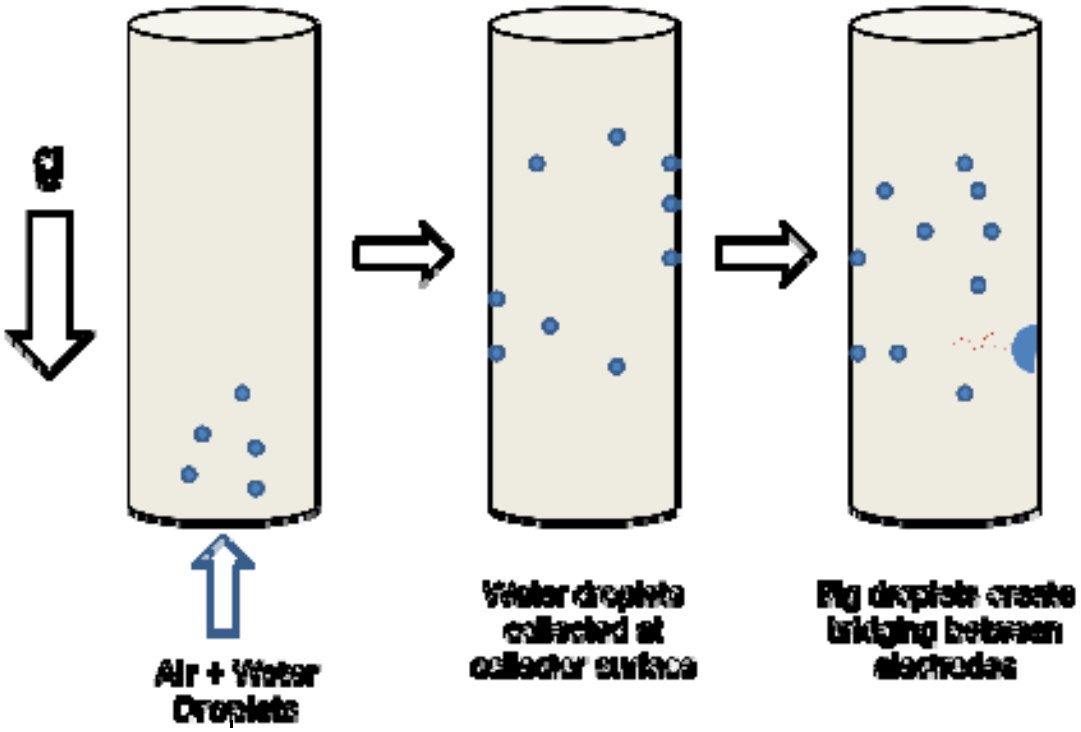

Figure 5-21 Bridging betweeen electrodes during upward flow testing

When the air flowed downward, bridging was eliminated. The big droplets at the collector surface dripped out of the separator and were carried out with the flow. The droplet size ranged between 2-3 mm.

5.6.4. Parametric Study

The study investigated the effect of varied parameters, including applied voltage, emitter polarity, airflow velocity and temperature on the performance of electrostatic separation. The range of selected parameters is shown in Table 5-4. The results will be presented based on the concentration of total weight of droplets at the outlet for different values of applied voltage.

Table 5-4 Experiment Varied Parameters

Wire electric potential (kV)	ϕ_e = 0, 1, 2, 3, 4, 5, 6, 7
Emitter Polarity	Positive, Negative
Average air flow inlet velocity (m/s)	$\mathbf{u}_f$ = 0.3, 0.9, 1.5, 5.0, 7.5

5.6.4.1. Effect of Applied Potential

The first parametric study focused on the effect of applied voltage on the electrostatic separation performance. But, before the results are discussed, the current-voltage characteristics curve (CVC) is presented for dry air in Figure 5-22 for the geometry of interest under standard conditions. It was mentioned earlier in section (2.1.2) that the CVC curve could be used to assess the electrostatic separator's performance. So, the higher the value of corresponding current at fixed voltage, the better the ionization process, which leads to better performance.

Since the geometry is consistent with a wire-tube separator, the current in Figure 5-22 is presented as current per unit length (**J**). The polarity of the emitter for the following CVC curve is negative.

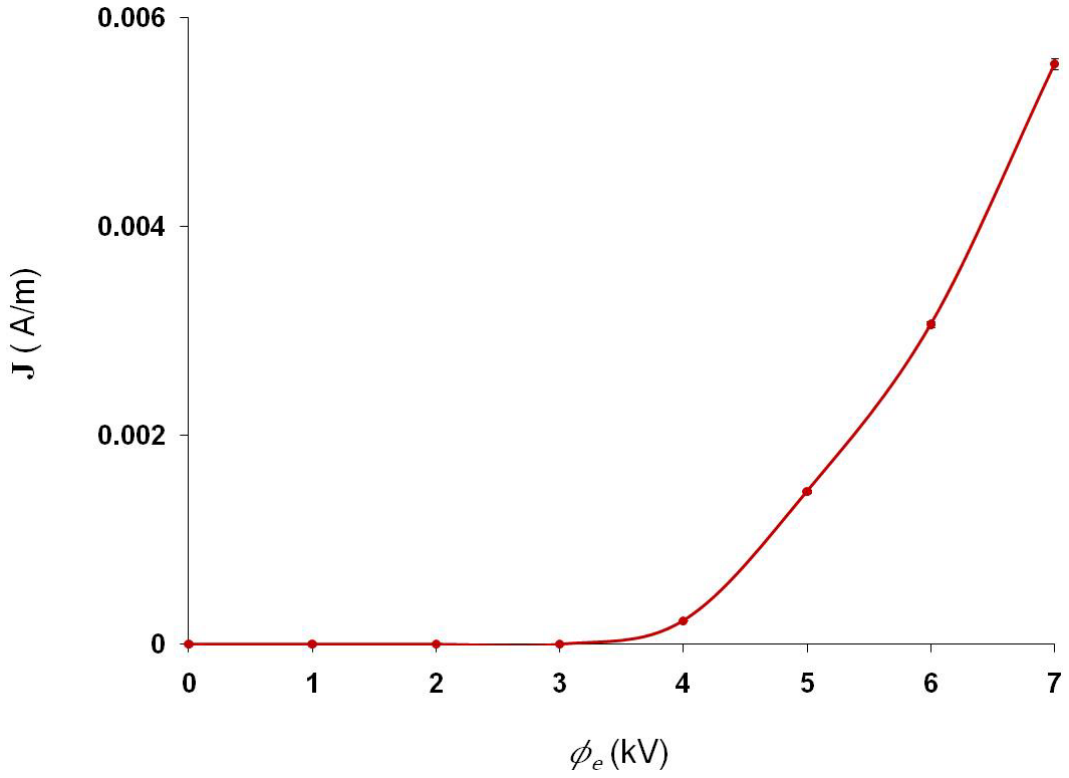

Figure 5-22 Current-voltage characteristics curve for wire-cylinder separator (standard conditions, negative polarity)

The onset voltage (ϕ_0) for this geometry is 3.8 kV. After this value, the ionization process takes place inside the separator. The maximum voltage reached for this and all other studied cases is 7.0 kV.

The effect of applied voltage on the concentration of total weight of water droplets at the outlet is shown in Figure 5-23. The velocity of airflow inside the separator was 0.9 m/s. The results were repeatable to within the APS accuracy.

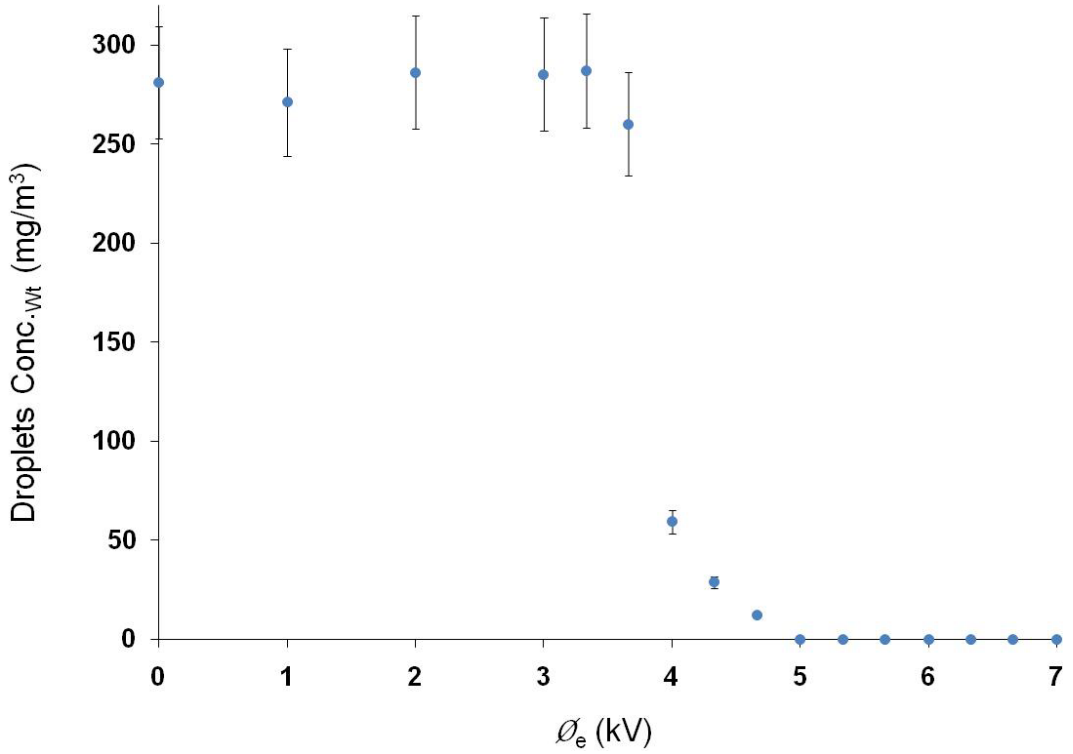

Figure 5-23 Effect of applied voltage on separator performance based on total weight of droplets (u_f = 0.9 m/s, negative polarity, standard conditions)

The electrostatic force started to show its effect in separating oil droplets from airflow after the ionization process started at 3.8 kV. At a voltage of 4.0 kV, the weight concentration dropped significantly, indicating very high separation performance. Figure 5-24 presents the same data in term of the total efficiency that was calculated based on Equation (5-3). The total efficiency at applied voltage of 7.0 kV was 99.999 %.

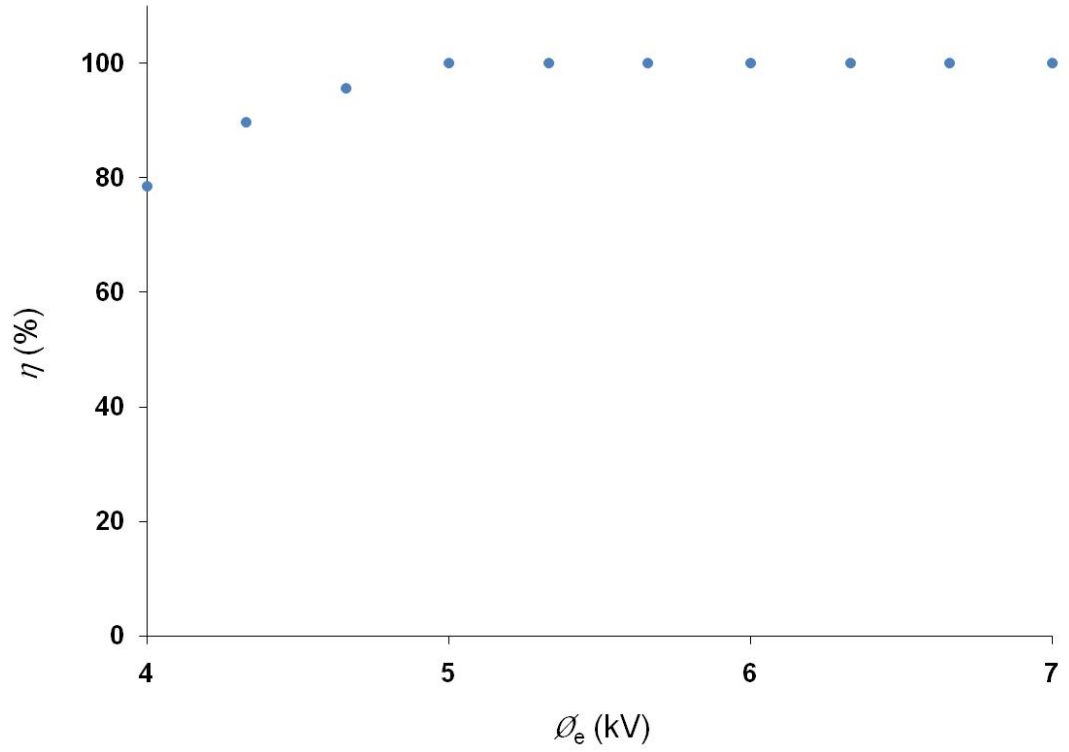

Figure 5-24 Effect of applied voltage on separator performance based on total efficiency (u_f = 0.9 m/s, negative polarity, standard conditions)

5.6.4.2. Effect of Emitter Polarity

As discussed in section (2.1.2.1), emitter polarity plays significant role in the ionization process. This can be verified instantly by obtaining the CVC curve for both polarities, as shown in Figure 5-25. The emitter polarity eventually will affect the charging and separation mechanisms. Therefore, a comparison study was conducted where the emitter polarity was changed. Figure 5-26 shows the effect of polarity on the electrostatic separation.

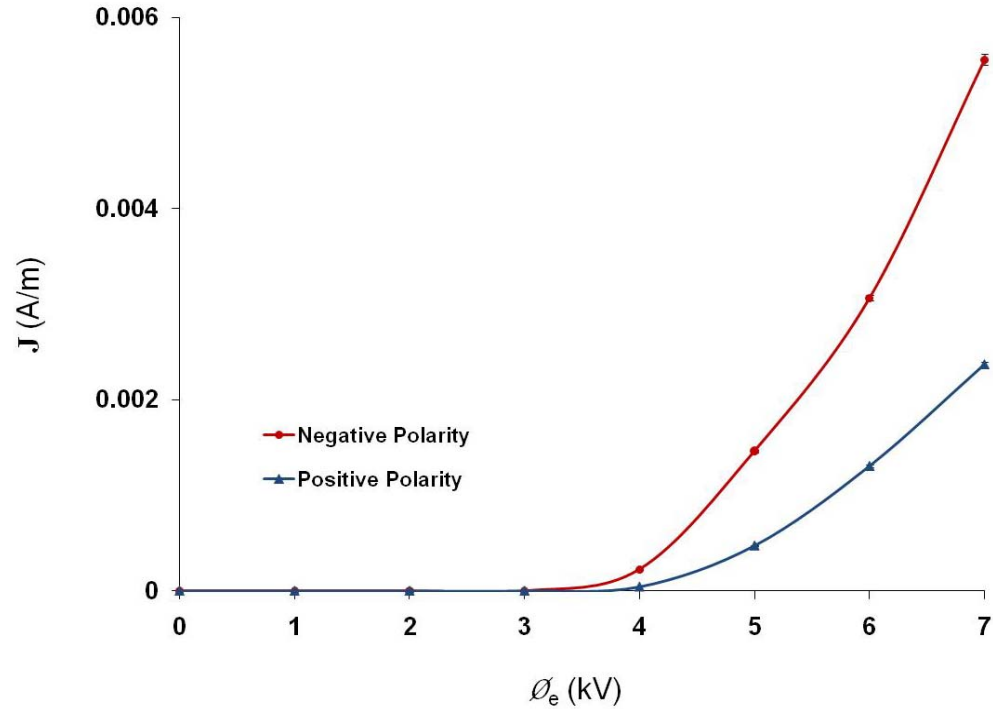

Figure 5-25 Current-voltage characteristics curve comparison between positive and negative polarities (standard conditions)

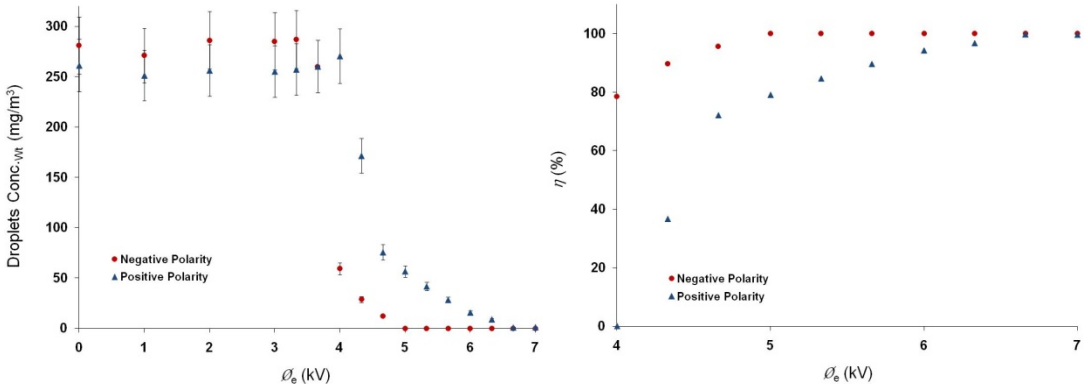

Figure 5-26 Effect of emitter polarity on separator performance based on total weight of droplets (u_f = 0.9 m/s, standard conditions)

The CVC clearly distinguished between the ionization process of positive and negative charging. The negative charging was higher, and thus it performed better in the separation process. With negative charging, the separation process began at lower voltage than the positive one. The trend of the graph showed better efficiency at all

voltage settings for the negative charging process. At a maximum voltage of 7.0 kV the total efficiency was 99.999 % for negative charging, whereas it was 98.536 % for positive charging.

5.6.4.3. Effect of Flow Velocity

This case study investigated the effect of the flow velocity on the separation efficiency. Changing the flow velocity does not have any effect on the CVC, so the CVC in this study can be the same as the one in Figure 5-22. Therefore, one may assume the charging process would be the same for all cases. The velocity range for the studied cases was from 0.3 to 7.5 m/s, as shown in Figure 5-27. The test was conducted under standard conditions, and emitter polarity was negative.

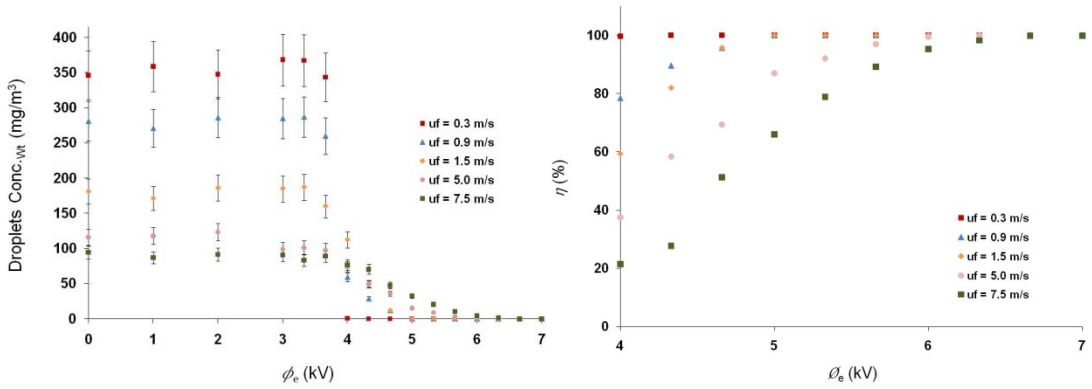

Figure 5-27 Effect of flow velocity on separator performance based on total weight of droplets (negative polarity, standard conditions)

The initial water droplet concentration was different between the cases, it decreased as the velocity was increased. Overall, all data points of different cases had the same trends, and all of them pointed at same conclusion. As expected, the performance of electrostatic separation was affected by the velocity of the flow. As the velocity increased, the separation efficiency decreased.

The flow velocity affected the movement of charged droplets toward the collector electrode. Higher velocity decreased the resident time that the droplets needed to travel to the collector electrode surface. The flow velocity did not have any effect on the charging process, which was verified by the CVC curves for the range of velocities used. This conclusion was expected, since the ion speed in the radial direction between electrodes could reach up to 240 m/s under standard conditions (Hinds 1999). Therefore, the effect of flow velocity can be neglected on the ionization and charging process, but not on the collection process. In the current study as the air velocity changed from 0.3 m/s to 7.5 m/s the separation efficiency decreased from an average of 99.966 % to average of 72.791 %.

5.6.5. Pressure Drop

The pressure drop across the separator was measured with the differential pressure transducer. The objective of this test was to determine how much the secondary flow due to electrostatic force contributed to the total pressure drop. The total pressure drop was very small. For example, at an average velocity of 7.5 m/s, the total pressure was only 87.0 Pa. When the applied voltage was increased to the maximum voltage of 7.0 kV, the pressure drop went up to 98.0 Pa, thus introducing a negligible pumping power consumption. To measure the ratio of the electrostatic force's effect on the total pressure drop, Equation (5-4) was used.

$$DP_{ratio,\phi_e} = \left(\frac{DP_{\phi_e} - DP_{\phi_e=0}}{DP_{\phi_e}}\right) * 100 \qquad \textbf{(5-4)}$$

where DP_{ϕ_e} is the total pressure drop when a certain voltage is applied and $DP_{\phi_e=0}$ is the pressure drop when there is no applied voltage. Figure 5-28 shows the pressure drop study for five cases of different flow velocities.

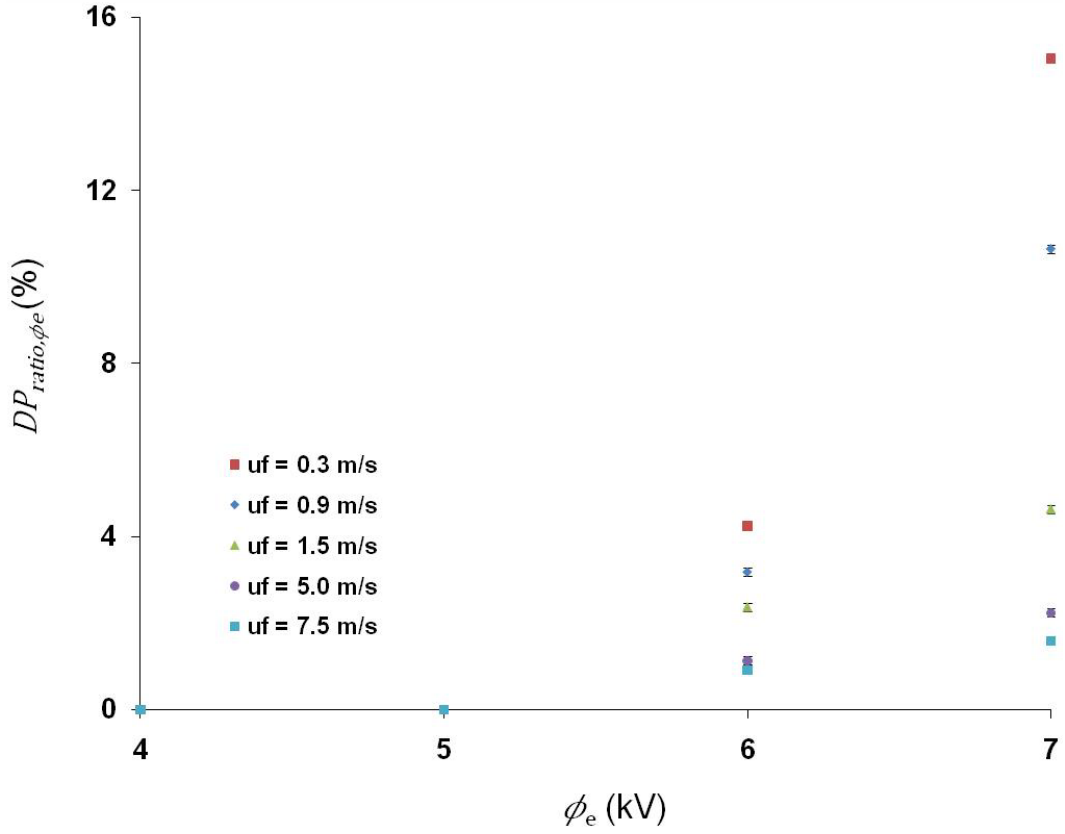

Figure 5-28 Effect of electrostatic force on total pressure drop across the separator (negative polarity, standard conditions)

The electrostatic force created a secondary flow of ions and droplets in the radial direction that participated in the total pressure drop. The pressure drop due to electrostatic force was independent of the flow velocity and was only a function of applied voltage. Therefore, it was the same for each voltage no matter what the velocity was. As a result the effect of electrostatic force on total pressure drop was decreased as the velocity increased. But in general, the pressure drop due to electrostatic force can be neglected.

5.6.6. Comparison between Experimental and Numerical Results

This section presents a comparison study between the numerical results obtained in Chapter 4 against the results presented in this chapter. Figure 5-29 shows the grade efficiency with the droplets diameter for a flow velocity of 0.9 m/s and applied voltage of 4.0 kV.

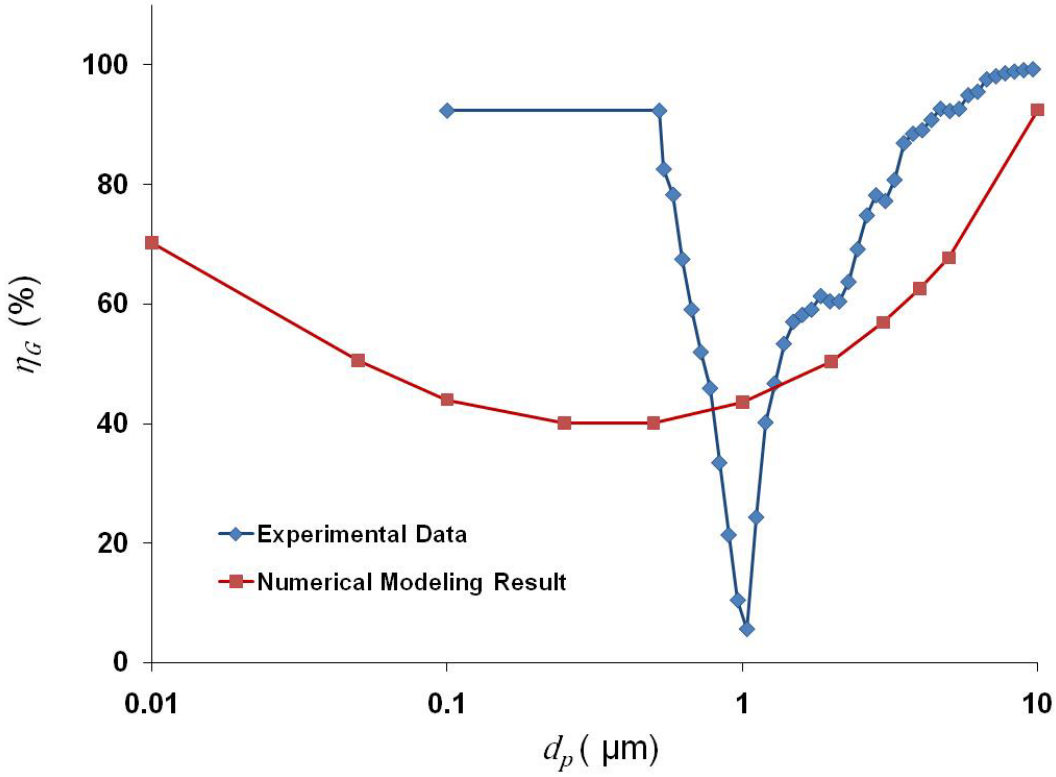

Figure 5-29 Comparison between numerical modeling results and experimental data (ϕ_e=4 kV, u_f=0.9 m/s)

The numerical modeling under predicted the performance of the separator in general, except for small range of droplets size. In contrast, the model over predicted the lowest efficiency of the separation. Based on the model, the lowest efficiency was obtained at diameter size of 0.5 µm where in the experimental data it was at 1.0 µm.

The average efficiency calculated from the model and obtained from the experimental data was 56.3 % and 70.3 %, respectively.

There are few reasons for such difference between the two approaches. First, in spite of the complexity of the governing equations and numerical simulation procedure, this was still a quite simplified model for the actual charging process. For example, the interaction between particles was not considered. The model also assumed uniform surface injection of droplets. It was verified that injection location of droplets affects the separation efficiency greatly.

The higher efficiency of the experimental data may be due to the free surface charge that droplets had before entering the separator, see section (2.2.3.2). In the model the droplets were assumed to have zero charge at the inlet of the separator. Also, when some droplets set on the wire and tube surfaces, they might affect the CVC curve and ionization process. The accuracy of the particle sizer also participated in increasing the difference between the two approaches. Overall, an acceptable agreement between numerical model and experimental results in predicting the trend of the grade efficiency with the droplet size was shown.

5.7. Conclusion

A testing facility was constructed to study the performance of a wire-tube electrostatic separator in removing fine water droplets from an airflow. A parametric study on the performance of electrostatic separators was performed, and the influences of applied potential, emitter polarity and fluid velocity were investigated. Based on the results obtained, increasing the applied voltage directly increases the separation efficiency. Also, separation performance in general was higher with

negative polarity than positive polarity. The electrostatic separation was active and noticeable as the applied voltage was over the onset voltage. As the voltage was increased, the gap difference in the efficiency started to decrease as the applied voltage approached 7.0 kV.

On the other hand, the efficiency decreases as the flow velocity increases. Electrostatic separation can be considered an energy-efficient mechanism. The maximum power consumption used in this study was about 6.0 W, which represented a voltage of 7.0 kV and current of 0.85 mA.

The experimental data was compared against the results obtained by the numerical modeling. In general, the numerical modeling under predicted the performance of the separator. However, the two approaches had an acceptable agreement in predicting the trend of the grade efficiency graph with droplet diameter.

5.8. Summary

This chapter presented in detail the steps taken for testing a wire-tube electrostatic separator. A mixture of air-water droplets was used in the tests. A closed test loop was constructed to test the separator performance. The objective was to conduct a parametric study that showed the effect of applied potential, emitter polarity and flow velocity on the separation efficiency. The pressure drop due to the electrostatic force was verified. Finally, a comparison study between numerical modeling and experimental data was conducted.

CHAPTER 6: AIR-OIL SEPARATION—EXPERIMENTAL WORK AND RESULTS

6.1. Introduction

This chapter investigates the effect of electrostatic separation on removing of fine oil droplets from airflow. The experiment in this chapter is similar to the study conducted in Chapter 5. The reason of repeating the experiment was to check the performance of electrostatic separation with low relative permittivity liquid (ε_p), as in oil. Beside the parameters that were targeted in the previous chapter, the effect of flow temperature (T_f) was highlighted in this study. This parameter was not included in Chapter 5 due to the evaporation of water droplets as explained in section (5.6.1). Therefore, the total parameters addressed in this chapter were applied voltage (ϕ_e), emitter polarity (+,-), air flow velocity ($\mathbf{u}_f$) and temperature (T_f).

The test section had a wire-tube geometry in which the wire was the emitter electrode (charged) and tube was the collector electrode (ground). A different testing facility was constructed for air-oil separation study. The main reason for not using the same air-water test rig was to keep the water loop clean from any oil contamination. Instruments and measurements devices used in the setup will be described, and the testing procedures will be explained in detail. Finally, the results highlighting the performance of the separator will be presented.

6.2. Test Setup

6.2.1. Test Section

The test section that was used in this experiment had the same wire-tube geometry and dimensions as the test section in Chapter 5. The only difference was how it was assembled. The test section consisted of the electrostatic separator, used to separate the fine oil droplets from the air stream. A wire-tube geometry was implemented for the separator design as shown in Figure 6-1. The wire acted as the emitter electrode (charged), while the tube performed as the collector electrode (ground). The wire had a diameter of 0.08 mm and made out of stainless steel. The tube inside diameter was 20 mm and made out of copper. The lengths of wire and tube were both 150 mm.

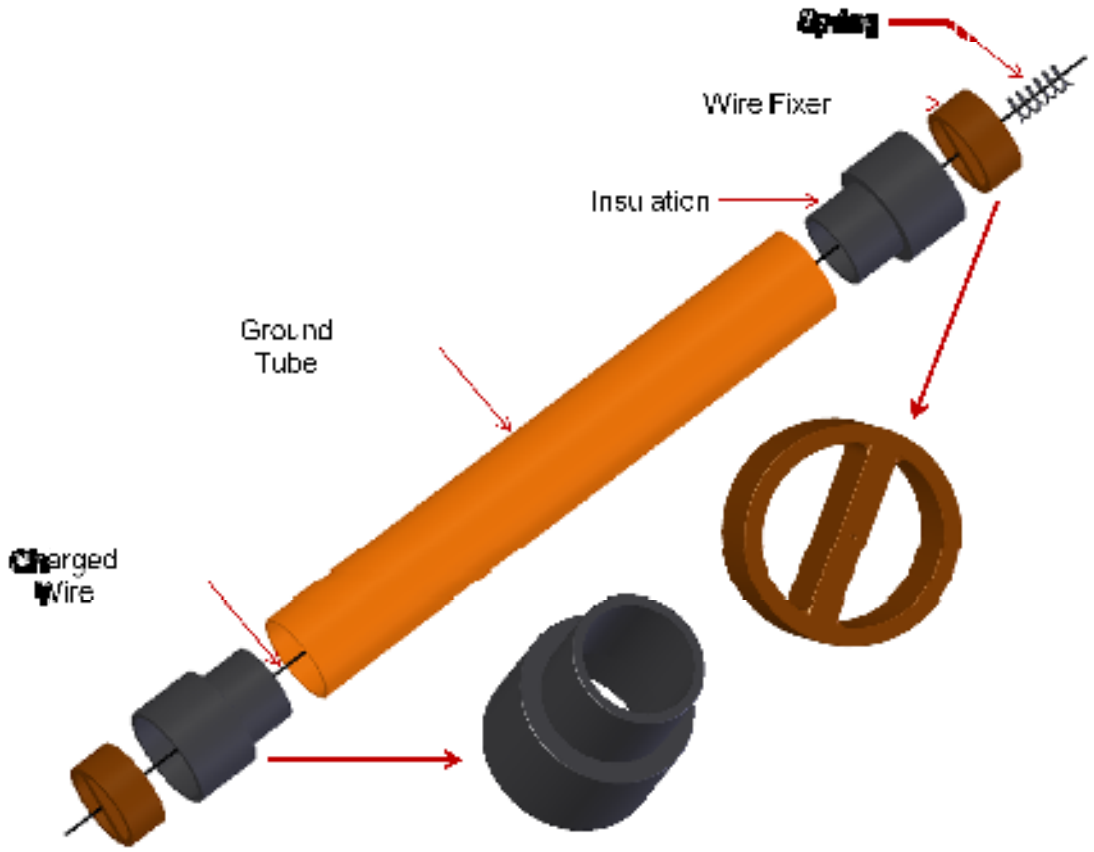

Figure 6-1 Schematic diagram of wire-tube electrostatic separator

Figure 6-1 shows how the wire-tube separator was constructed. Two wire fixers at each end of the tube centered the wire in the middle of the tube. Between each wire fixer and the tube, a polycarbonate fitting was used as insulation between the two electrodes. Since oil is a dielectric fluid, the conductivity was not an issue of how the wire was assembled and there was no need to fix the ends of the wire far from the ground tube. At one end of the wire, a spring kept the wire stretched. A portion of the wire surface area that was not placed inside the copper tubes was insulated. Therefore, the length of the wire that was not insulated was the same as the length of the tube.

6.2.2. Test Loop

An open loop was used for the separator testing. All tubes, fittings and other connections were made of nondegrading material to insure that there was no contamination in the test loop. Also, an air filter removed impurities from the air before the oil droplets were injected. Figure 6-2 shows a schematic sketch of the test loop.

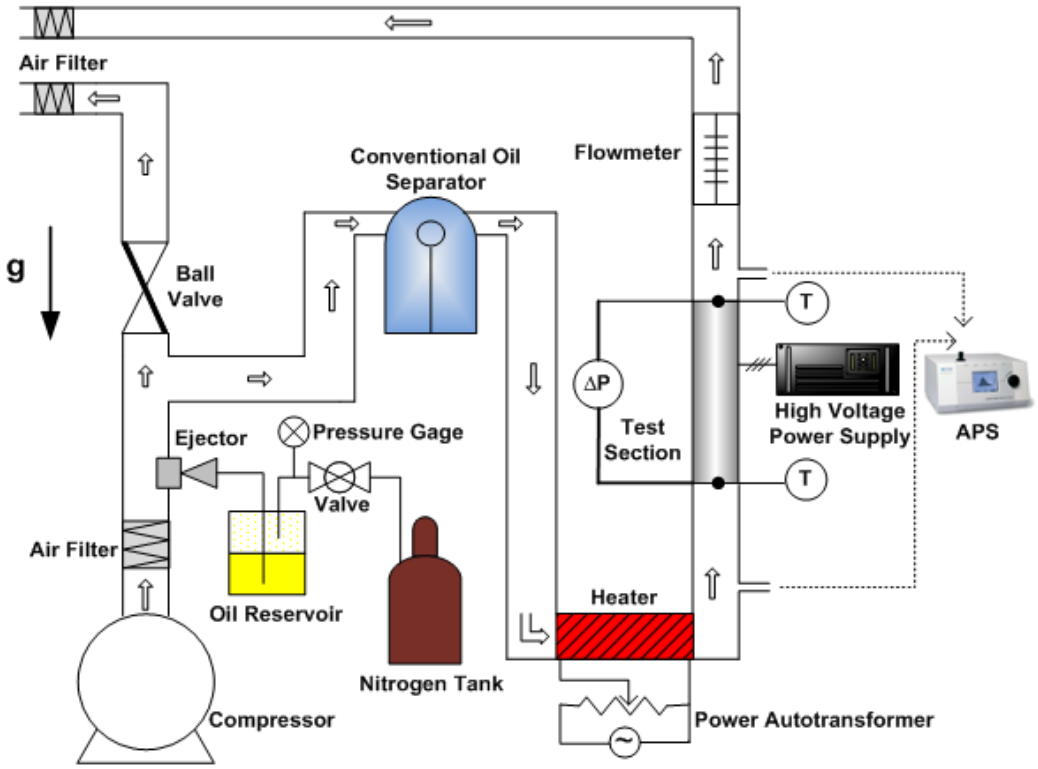

Figure 6-2 Schematic sketch of air-oil separation test loop

The main components of the test loop are listed below:

10. Air compressor

11. Oil reservoir

12. Ejector

13. Nitrogen tank

14. Ball valves

15. Conventional oil separator (Alco Control, Inc., A-F58824)

16. Heater

17. Variable autotransformer

18. Aerodynamic particle sizer (TSI, Inc., 3321)

19. DC high-voltage power supply

- Positive polarity (0-60 kV, Glassman, Inc., ER60P5)
- Negative polarity (0-30 kV, Glassman, Inc., EK30N20)

20. Variable area flowmeter (Omega, Inc., FL-1502A)

21. Thermocouples (Omega, Inc., T-type)

22. Differential pressure transducer (Validyne Engineering, Inc., DP-15)

The air flowed through the filter first to clean it from impurities. Once it passed through the ejector connected to the oil reservoir, the oil droplets were injected to the air flow. The oil reservoir was pressurized to approximately about 70.0 kPa. A ball valve adjusted the airflow rate to the test section, after which the air-oil mixture entered the conventional oil separator to remove the big oil droplets. Then the air and smaller droplets went to the test section, the electrostatic separator, passing through the heater. The oil droplet concentration was measured at the inlet and outlet of the test section. Then the flow exited the test loop. A variable area flowmeter after the test section measured airflow rate. A filter at the exit captured any remaining oil droplets in the airflow. Table 6-1 shows the properties of the oil used in this study.

Table 6-1 Properties of Oil Droplets

Oil type	Alkyl-benzene (synthetic lubricant)
Density (kg/m^3)	ρ_p = 862
Dynamic Viscosity (N.s/m^2)	μ_p = 27 × 10^{-3}
Relative Permittivity	ε_p = 2.2

6.3. Instruments and Measurement Devices

- **Aerodynamic Particle Sizer (APS)**

The purpose of this device was to measure water droplet concentration and size at the inlet and outlet of the electrostatic separator. More details about the APS can be found in section (5.3).

- **Other Equipment and Devices**

The instruments and devices are presented in Table 6-2 along with their specifications, features and operational conditions range. Also the calibration curve of the differential pressure transducer is presented in this section.

Table 6-2 Equipment, Instruments and Measurement Devices

Device	Type	Manufacturer (Model)	Specifications
Differential pressure transducer	Diaphragm	Validyne Engineering, Inc. (DP-15)	• Range: 0-866 Pa • Accuracy: ±0.1 Pa
Thermocouple	T-Type	Omega, Inc.	• Range: -200-350 °C • Error: ±0.5 °C
Flowmeter	Rotameter	Fischer Porter	• Range: 0-0028 m^3/s • Accuracy: ±0.2%
Data acquisition switch unit		Agilent Technologies, Inc. (34970A)	• Thermocouple Accuracy: ±1.0 ^oC • DC voltage Accuracy (10 V): ± (0.0035 % of reading + 0.0005% of range)
High voltage power supply	Positive polarity	Glassman High Voltage, Inc. (ER60P5)	• Output Voltage: 0-60 kV • Output Current: 0-5 mA • Accuracy is 1% of rated + 1% of setting
High voltage power supply	Negative polarity	Glassman High Voltage, Inc. (EK30N20)	• Output Voltage: 0-30 kV • Output Current: 0-20 mA • Accuracy is 0.5% of rated + 0.2% of setting

- **Differential Pressure Transducer Calibration**

The only instrument that needed calibration for the air-oil separation test setup was the differential pressure transducer. The calibration process of the pressure transducer is explained in section (5.5). Figure 6-3 shows the calibration curve for the pressure transducer.

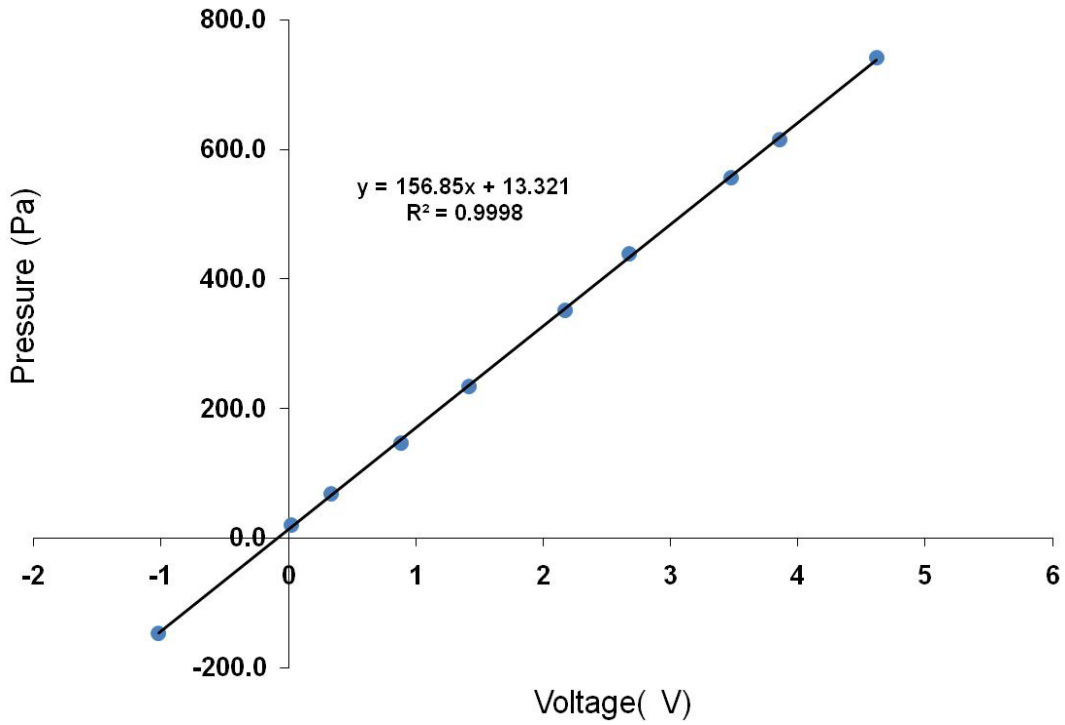

Figure 6-3 Differential pressure transducer calibration curve

6.4. Testing Procedures

The following testing procedures were followed for each test to insure the accuracy and repeatability of the results:

- Turn the data acquisition switch unit on and monitor temperature and pressure output readings;
- Turn the compressor on and adjust the flow rate using the ball valves;
- Pressurize the oil reservoir tank to constant pressure (70 kPa) to get steady oil injection to the air flow;
- Turn the heater on to adjust the temperature;
- Turn the APS on;
- Let the set setup loop reach steady-state conditions in terms of airflow temperature and injected oil droplet concentration;

- Take measurements of oil droplet concentration at the separator inlet;
- Increase voltage gradually and stop just before reaching breakdown voltage;
- Take measurements of oil droplet concentration at the separator for different values of applied voltage once it exceeds the onset voltage;
- Analyze collected data.

6.5. Results and Discussions

The total efficiency (η) will be used to calculate the efficiency of the electrostatic separation as shown in Equation (5-3).

6.5.1. Parametric Study

The study investigated the effect of varied parameters, including applied voltage, emitter polarity, airflow velocity and temperature on the performance of electrostatic separation. The range of selected parameters is shown in Table 6-3. The results will be presented based on the concentration of total weight of droplets at the separator outlet for different values of applied voltage.

Table 6-3 Experiment Varied Parameters

Wire electric potential (kV)	ϕ_e = 0, 1, 2, 3, 4, 5, 6, 7
Emitter Polarity	Positive, Negative
Average air flow inlet velocity (m/s)	$\mathbf{u}_f$ = 1.0, 2.0, 3.0, 4.0, 5.0
Airflow temperature (K)	T_f = 300, 315, 330

6.5.1.1. Effect of Applied Potential

The current-voltage characteristics (CVC) curve for the geometry is presented in Figure 5-22. Figure 6-4 shows the oil droplet concentration obtained by the APS at the inlet of the separator. The mean diameter of droplets was 0.9 µm, which is a suitable size for the purpose of this study. The effect of applied voltage on the concentration of total weight of oil droplets at the outlet is shown in Figure 6-5. The velocity of airflow inside the separator was 1.0 m/s. The results were repeatable to within the APS accuracy.

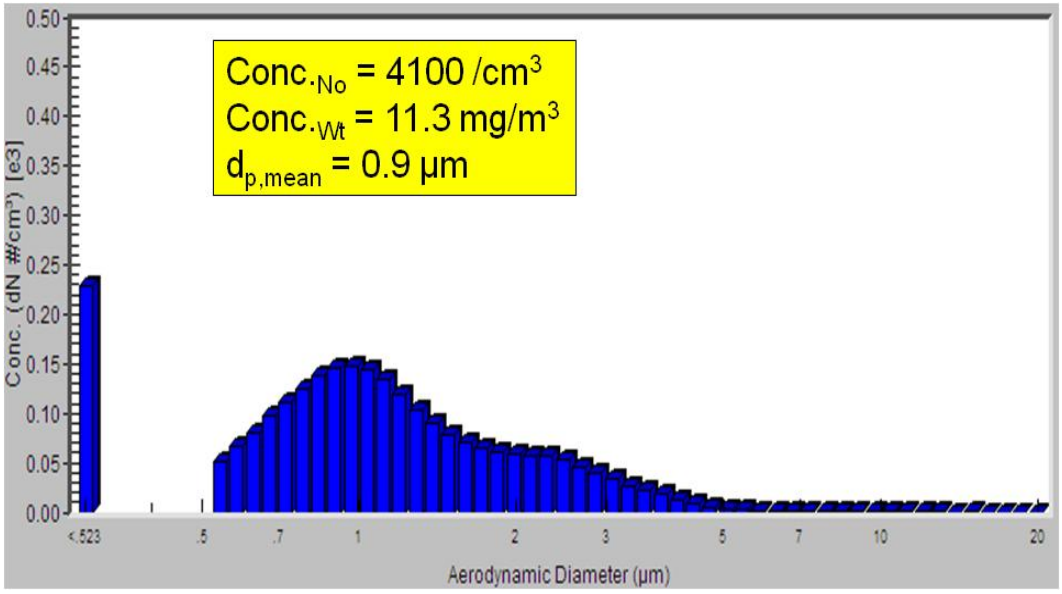

Figure 6-4 Oil droplet concentration at inlet (u_f = 1.0 m/s, standard conditions)

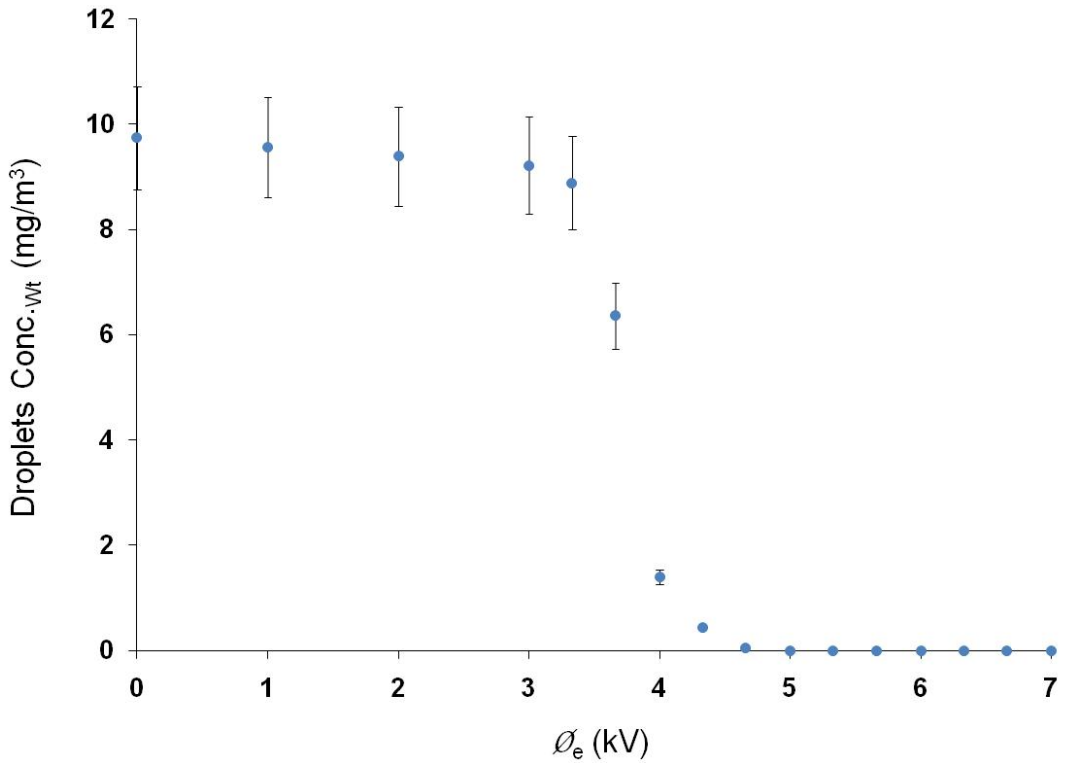

Figure 6-5 Effect of applied voltage on separator performance based on total weight of droplets (u_f = 1.0 m/s, negative polarity, standard conditions)

Although the relative permittivity of oil is low (2.0), the electrostatic separation showed efficient performance on removing of oil droplets from airflow. At a voltage of 5.0 kV, the weight concentration dropped significantly, indicating very high separation performance. The total efficiency, based on Equation (5-3), at applied voltage of 7.0 kV was 99.998 %.

6.5.1.2. Effect of Emitter Polarity

The CVC curve for positive and negative polarity is shown in Figure 5-25. Figure 6-6 shows the effect of polarity on the electrostatic separation. The graph shows droplet total weight at the outlet vs. applied voltage.

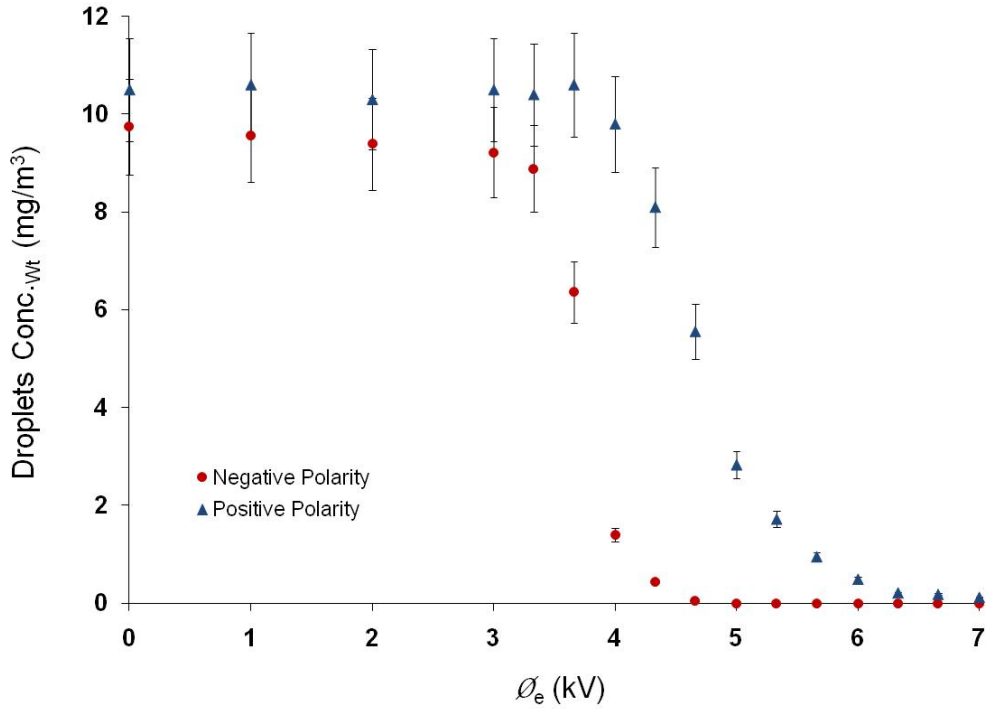

Figure 6-6 Effect of emitter polarity on separator performance based on total weight of droplets (u_f = 1.0 m/s, standard conditions)

The total efficiency based on positive polarity was lower than the negative polarity, also shown in section (5.6.4.2). Overall, the efficiency of electrostatic separation of negative polarity was highly efficient. At a maximum voltage of 7.0 kV the total efficiency was 99.998 % for negative charging, whereas it was 98.965 % for positive charging. The average efficiency dropped from 98.211 % to 74.173 % when polarity was switched from negative to positive.

6.5.1.3. Effect of Flow Velocity

This section investigated the performance of the electrostatic separation under different airflow velocity values. The velocity range for the studied cases was from 1.0 to 5.0 m/s, as shown in Figure 6-7. The test was conducted under standard conditions, and emitter polarity was negative.

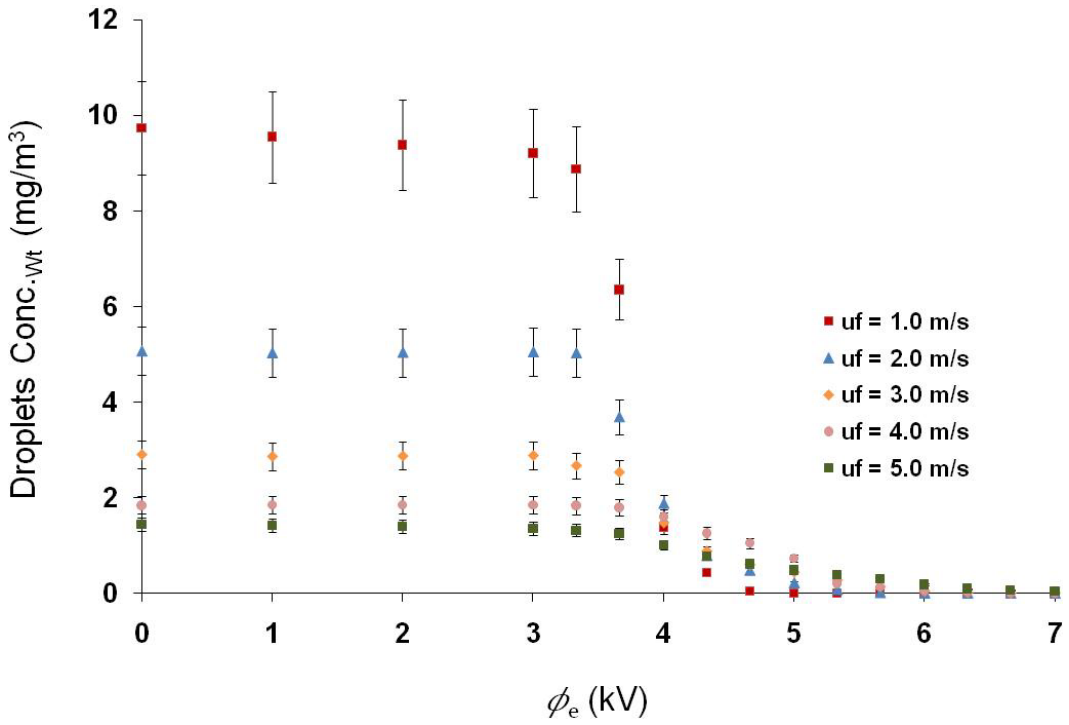

Figure 6-7 Effect of flow velocity on separator performance based on total weight of droplets (negative polarity, standard conditions)

For this study, it was challenging to keep the oil concentration constant while changing the flow rate for all cases. There were attempts to increase oil injection while increasing airflow rate, but the oil concentration at the separator inlet was not changed. This was due to the conventional oil separator. As more oil injected, as big droplets, the conventional oil separator was removing more oil from the flow. Therefore, the oil concentration at the separator inlet dependent more on the airflow rate rather than on the amount of oil injected. As the flow rate increased, the oil concentration decreased.

As shown in the figure, the total efficiency decreased as the velocity was increased. Refer to section (5.6.4.3) for detailed explanation about the effect of velocity on the separation performance. Even though the velocity increased 5 times, the effect of electrostatic separation was noticeable. In the current study as the air

velocity changed from 1 m/s to 5 m/s the separation efficiency decreased from an average of 99.998 % to average of 96.627 %.

6.5.1.4. Effect of Flow Temperature

This study was not conducted on the air-water separation work, as explained in section (5.6.1). It was assumed that the air flow and oil droplets had the same temperature. This assumption is realistic since the droplets had very small size (less than 1 µm). Three studies were conducted with different temperatures: 300, 315 and 330 K. The heater was used to increase the temperature of air. First, the effect of temperature on the CVC curve was assessed, as shown in Figure 6-8.

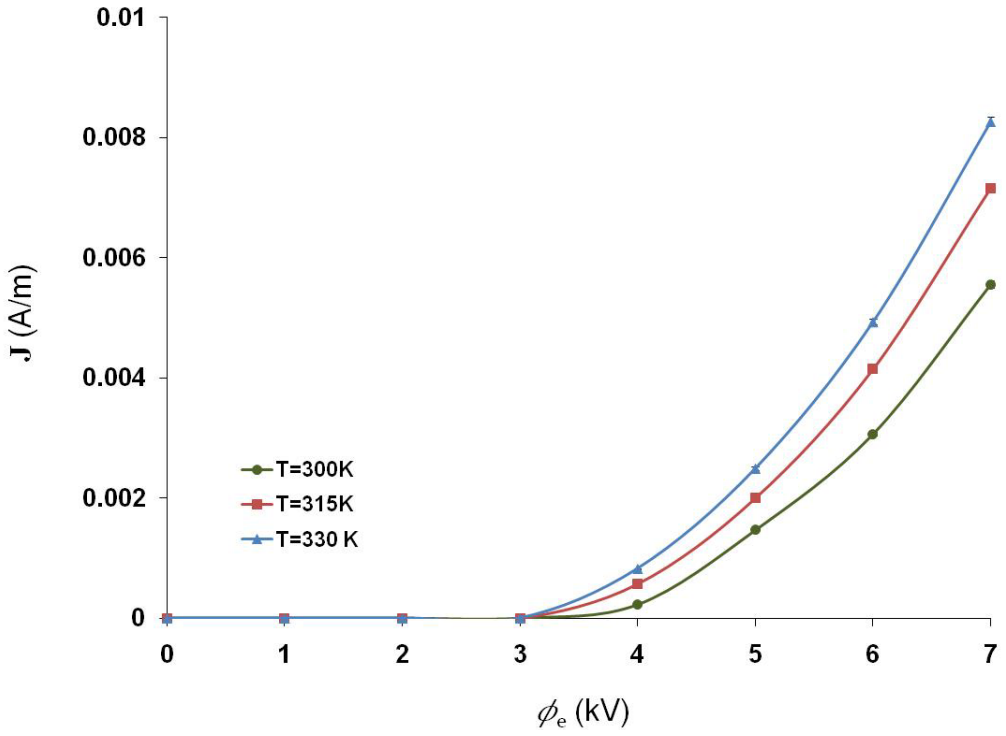

Figure 6-8 Current-voltage characteristics curve for different temperature (negative polarity, standard conditions)

As the temperature increased, the current at each voltage value increased too. The onset voltage started at slightly lower voltage each time the temperature

increased, but it was not a significant difference. At a maximum voltage of 7.0 kV the current increased about 55% when temperature was increased from 300 to 330 K. This could be explained by laying out the relation between temperature and the mean thermal speed of the ions ($\bar{C}_i$). Equation (6-1) shows the exponential relation between ion speed and temperature based on the Maxwell-Boltzmann distribution (Scheeline and Zoellner 1984).

$$\bar{C}_i = \sqrt{\frac{2\ k\ T_i}{m_i}} \qquad \textbf{(6-1)}$$

where k, T_i and m_i are Boltzmann constant, ion temperature, and ion mass, respectively. As the temperature increases, the ion speed increases. This leads to an increase in the current between the electrodes as shown in CVC curve.

The next graph shows the effect of temperature on the separator performance. Figure 6-9 shows the total weight concentration at the separator outlet for different voltage settings.

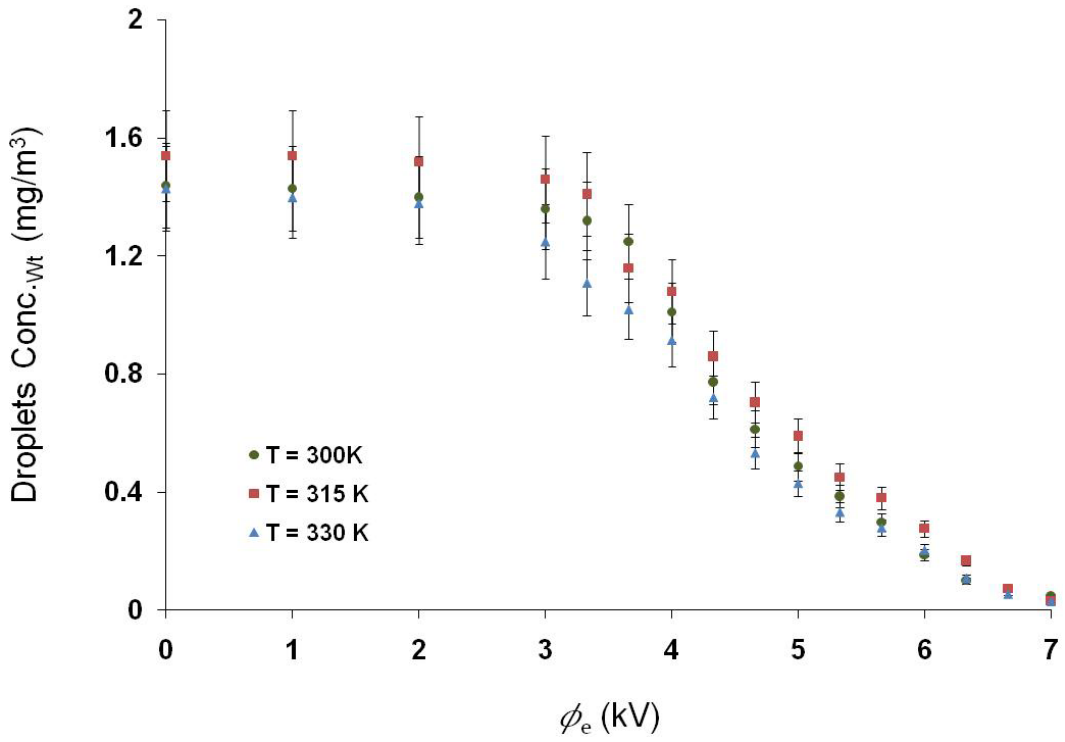

Figure 6-9 Effect of flow temprature on separator performance based on total weight of droplets (negative polarity, u_f = 5.0 m/s)

Based on Figure 6-9, increasing the temperature enhanced the separation performance. This was due to the enhancement of the ionization process that was explained in the CVC curve discussion. More ions lead to better charging and therefore, better separation. The total efficiency at 7.0 kV was 96.27 % and 97.8 % for 300 and 330, respectively, under the specified conditions.

6.5.2. Breakup of Oil Droplets

During the current studies, the oil droplets tended to break as a result of accumulated electric charges on the surface of the droplets. This phenomenon occurs when the electric charge accumulated at the surface of a droplet exceeds the surface tension (γ). This causes the droplet to tear and break up into smaller droplets, as

discussed in section (2.2.3.2). This limit is mathematically predicted by the Rayleigh limit (q_R), Equation (2-10).

The breakup phenomenon was verified by plotting the total number of droplets concentration versus the applied voltage, as in Figure 6-10. The figure also shows the mean diameter of droplets. After the onset voltage, as the voltage increased, the total number of droplets started to increase until a voltage of 5.5 kV. Then it started to decrease as the voltage was increased. The mean diameter of droplets was initially 0.9 µm. As the droplets were breaking up, the mean diameter decreased to 0.65 µm.

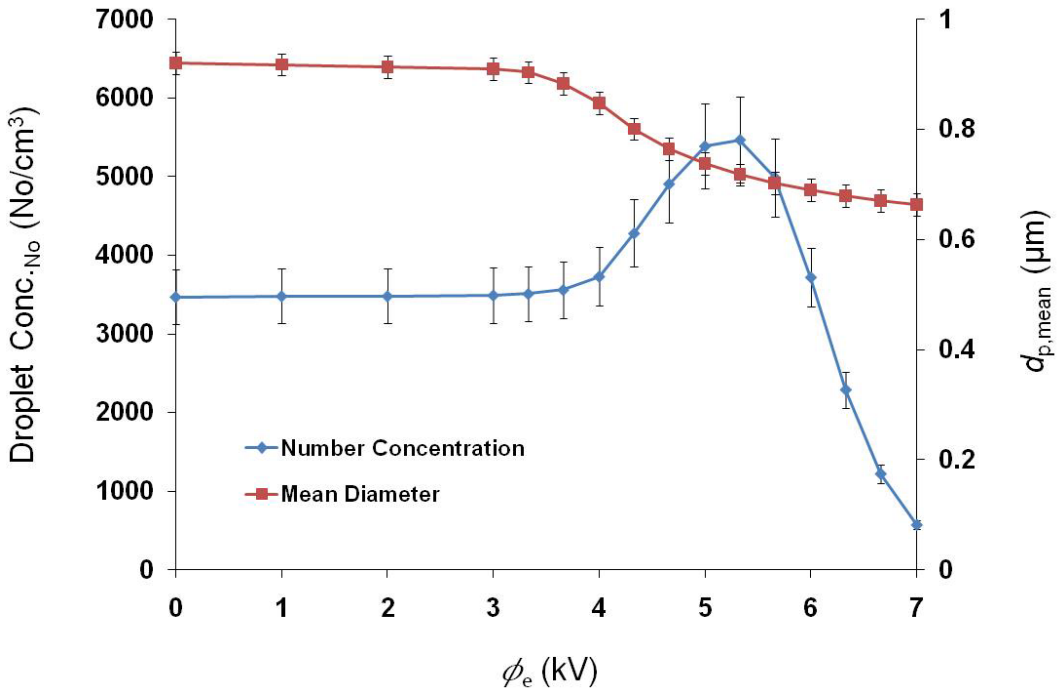

Figure 6-10 Droplet breakup based on droplet mean diameter and total number concentration (negative polarity, u_f = 5.0 m/s, standard conditions)

As the droplets were breaking up, the electrostatic separation was taking place. This was verified by plotting both the total number and weight concentrations versus the applied voltage as in Figure 6-11.

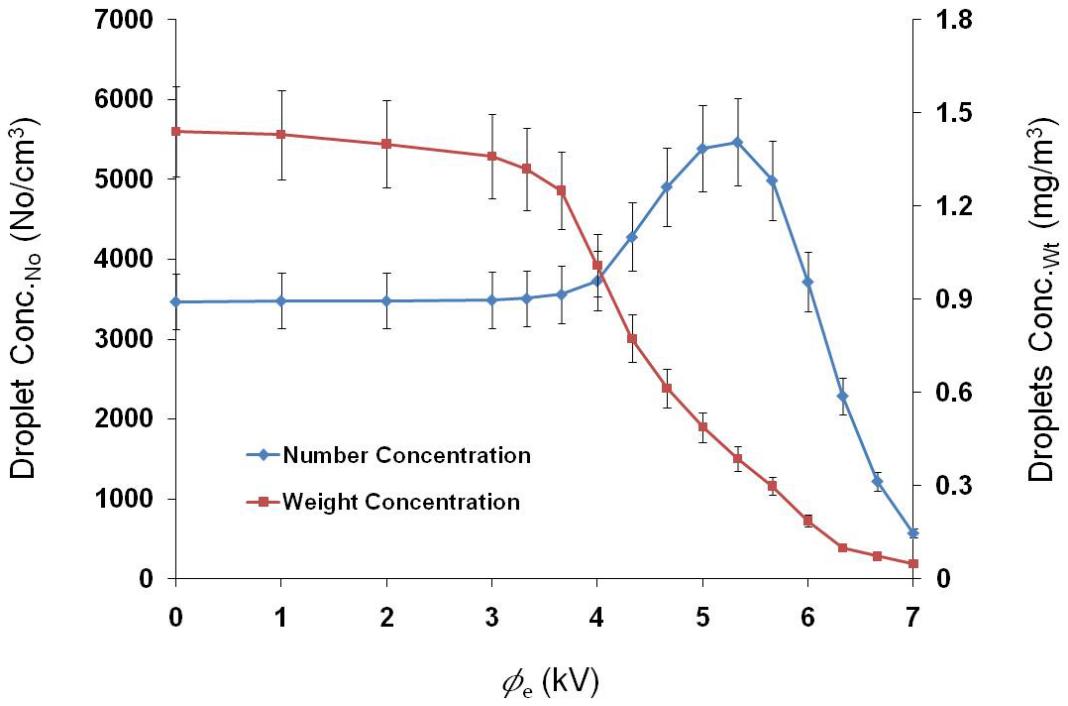

Figure 6-11 Droplet breakup based on droplet total number and weight concentrations (negative polarity, u_f = 5.0 m/s, standard conditions)

The graph shows that the total weight concentration dropped as the applied voltage was increased. Because of the breakup of oil droplets, this was another reason of not using the grade efficiency to evaluate the performance at each range since the breakup and separation were happening simultaneously.

6.5.3. Comparison between Air and Oil Separation

This section presents a comparison case study on the electrostatic separation between water and oil. The major difference between the two liquids is the relative permittivity. Water is a conductive liquid with high relative permittivity, 80, where oil is a dielectric liquid of low relative permittivity, 2.0. Figure 6-12 presents a comparison case between the two liquids under the same electric and fluid conditions. The total efficiency with the applied voltage is presented in the figure.

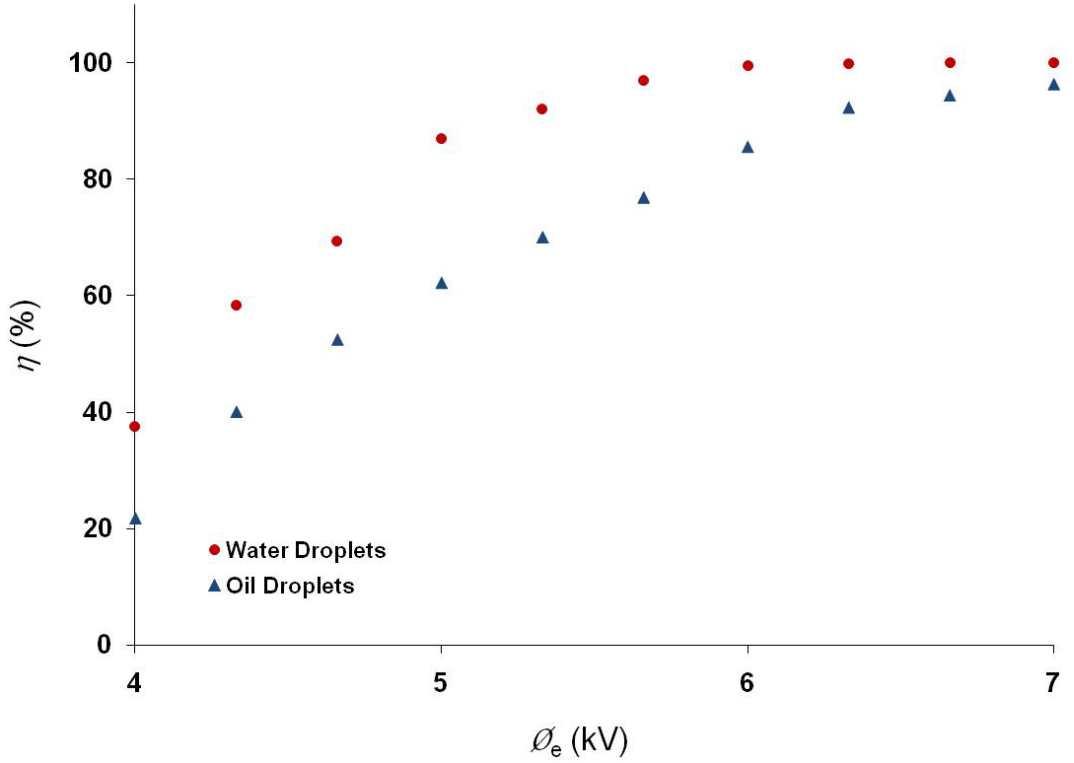

Figure 6-12 Comparison between experimental data on water-air and oil-air separation (u_f=5.0 m/s, standard conditions)

The electrostatic separation was more effective on water than oil. This conclusion was expected because of the higher relative permittivity of water. Although the relative permittivity of oil was less, about 40 times less, electrostatic force was very effective on oil removal from air stream.

Another difference was the breakup of oil droplets. This phenomenon was not observed on the water separation study. The difference in surface tension between the liquids was a major factor in the breakup. The water surface tension is 0.07 N/m where it is 0.02 N/m for oil at room temperature.

6.6. Conclusion

A testing facility was constructed to study the performance of a wire-tube electrostatic separator in removing fine oil droplets from an airflow. The objective of this work was to verify the behavior of low permittivity liquid, oil, under electrostatic charging process and compare it with the water separation conducted in Chapter 5. A parametric study on the performance of electrostatic separators was performed, and the influences of applied potential, emitter polarity, fluid velocity and temperature were investigated.

Although oil has very low relative permittivity compared to water, electrostatic charging was very effective on the separation of oil. The conclusions reached in this study regarding the applied voltage, emitter polarity and flow velocity was the same findings in the water separation. A new study highlighting the effect of flow temperature was conducted in this work. The effect of temperature on the performance of the separator was found to be insubstantial. Also, breakup of oil droplets was observed because of the low surface tension of oil. Electrostatic separation can be considered an energy-efficient mechanism. The maximum power consumption used in this study was about 9.0 W, which represented a voltage of 7.0 kV and current of 1.25 mA.

6.7. Summary

This chapter presented in detail the steps taken for testing a wire-tube electrostatic separator. A mixture of air-oil droplets was used in the tests. An open test loop was constructed to test the separator performance. The objective was to

conduct a parametric study that showed the effect of applied potential, emitter polarity, flow velocity and flow temperature on the separation efficiency.

CHAPTER 7: FIRST GENERATION AIR-WATER ELECTROSTATIC SEPARATOR—DESIGN, TESTING AND RESULTS

7.1. Introduction

This chapter highlights the design and testing of an air-water droplet electrostatic separator, with applications to a number of industries, including in the gas turbine combustor intake for aerospace and power aerospace applications. For aerospace applications the weight and volume of the separator should be minimal, as a common requirement of environmental control systems (ECS) for such systems. A test rig was constructed and the performance of the design was evaluated in a high water concentration environment (up to 27 gr water/ kg dry air). The separator demonstrated high efficiency in separation of submicron droplets as well as the ability to separate large amounts of water droplets different water concentration environment.

The separator design and fabrication will be introduced. The testing was conducted on the same setup which was used in the air-water separation, refer to section (5.2.2). Just few modifications were adopted in the test setup regarding different methods of water droplets production. Finally, the results that highlight the performance of the separator will be presented and discussed.

7.2. Air-Water Separator Design and Fabrication

7.2.1. Design of Emitter and Collector Electrodes

The test section of the setup consisted of the electrostatic separator used to separate water droplets from air. A wire-tube geometry was implemented for the separator design. The wire acted as the emitter electrode (charged), while the tube performed as the collector electrode (grounded). The wire had a diameter of 0.25 mm and was made of gold-plated nickel. The tube had a diameter of 20 mm and was made of perforated copper sheet. The lengths of the wire and tube were both 250 mm.

A perforated surface was used for the collector surface (see Figure 7-1) to ensure that the collected water droplets drained from the separator. In this way, the re-entrainment of collected water droplets was eliminated. The opening area of the perforated tube was about 40% of the total area, and the diameter of the openings on the perforated surface was 3.5 mm.

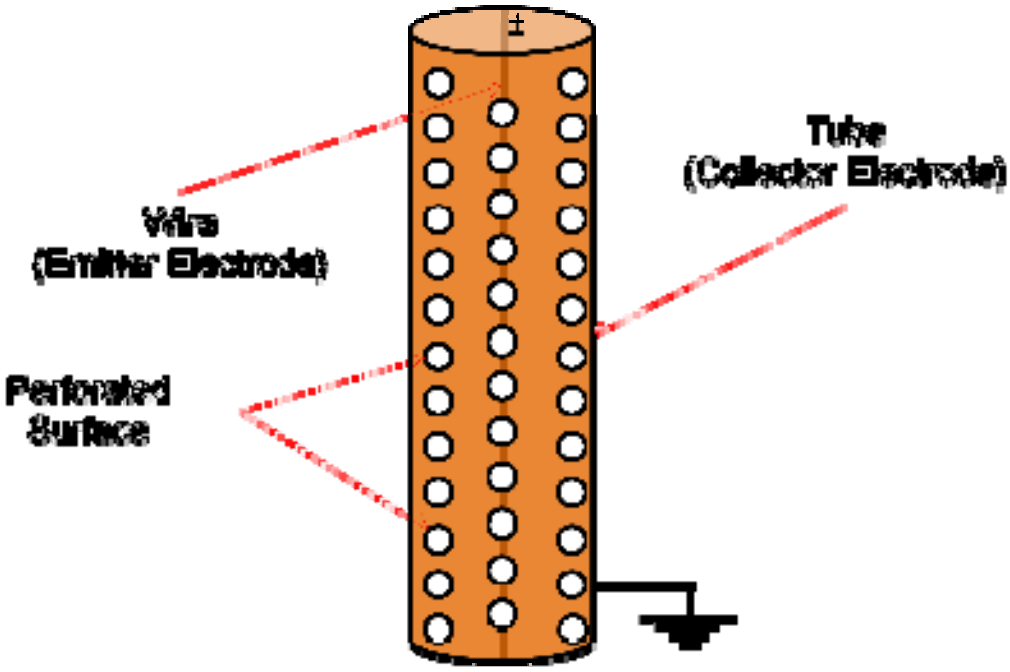

Figure 7-1 Schematic of wire-tube separator

7.2.2. Separator Assembly

The separator was constructed out of seven perforated tubes working in parallel for better performance. Each tube had a wire centered in the middle. A porous media structure was wrapped around each tube to enhance the collection of water droplets and limit their re-entrainment back to the flow. Then, a transparent plastic tube (OD = 76.5 mm, ID = 70.0 mm) was used to house the separator tubes, as shown in Figure 7-2. This caused the collected water droplets to accumulate in the space between the perforated tubes and the separator housing. The collected water was drained to a reservoir during operation through a drainage tube.

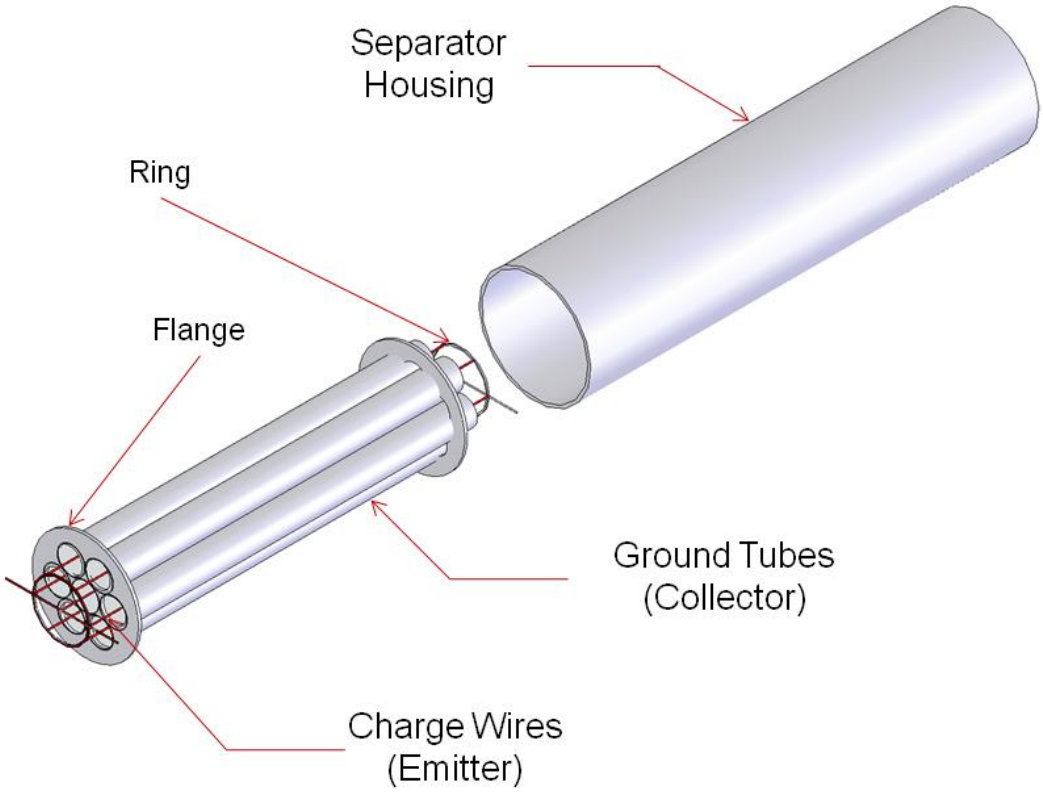

Figure 7-2 Drawing of the electrostatic air-water droplet separator

Two flanges were machined to secure the top and bottom ends of each tube, as depicted in Figure 7-2. Figure 7-3 shows the perforated tubes bundle mounted using the flanges with and without porous media. The diameter of each flange was almost the same as the inner diameter of the plastic housing (OD = 69.5 mm) so that the flanges are fixed inside the housing by friction. An O-ring was used to secure the flanges inside the separator housing.

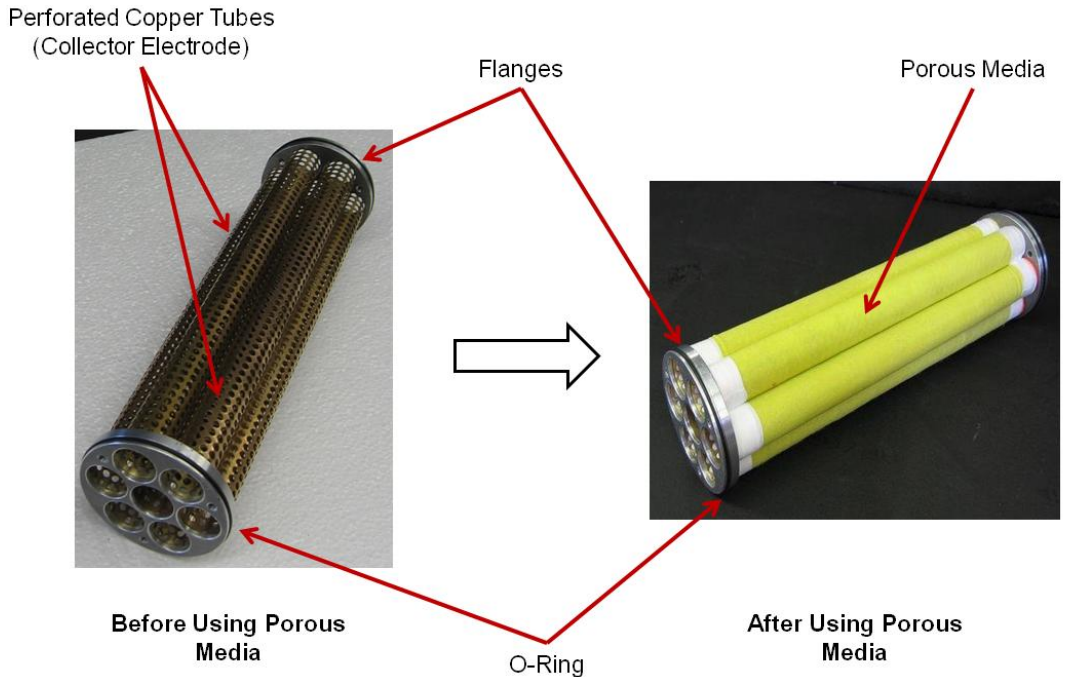

Figure 7-3 Mounting the perforated tubes using flanges

The wires were mounted in the center of each tube to achieve uniform charging along the wires and to avoid premature bridging or sparking between tubes and wires. Two star-shaped rings were molded out of epoxy and fiber, one for the top-side and the other for the bottom, as depicted in Figure 7-4.

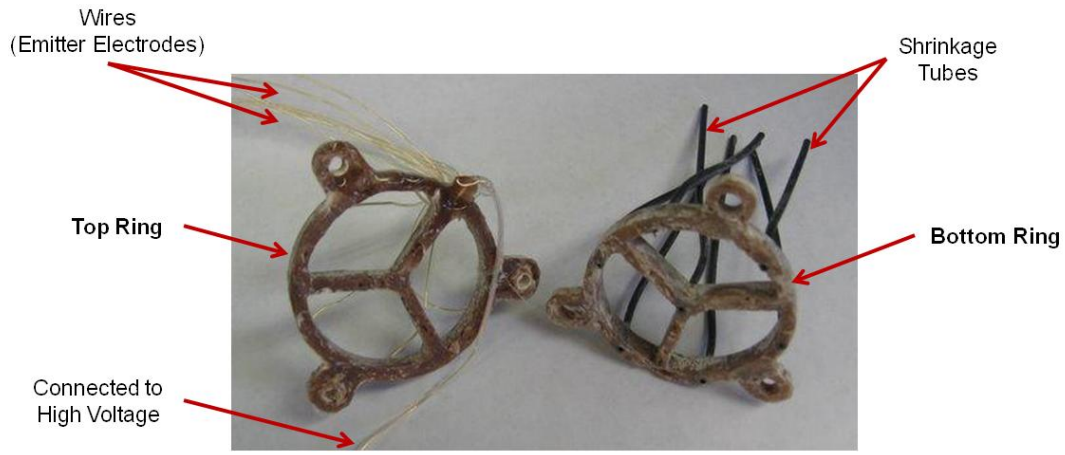

Figure 7-4 Rings made out of fiber and epoxy to secure the wires from the top and bottom

Eight protruding wires were embedded inside the top ring: seven were used as emitter electrodes and one was connected to a high voltage power supply. In the bottom ring, seven shrinkage tubes were partially embedded. These shrinkage tubes were used to fully cover the end connections of the wires while keeping them stretched. If one or more of the wires were not stretched, premature sparking would be likely. A portion of the wires' surface area that was not placed inside the perforated tubes was insulated. Therefore, the length of wires that was not insulated was the same as the length of the tubes. Three nylon threaded rods were used to connect the flanges and rings and hold them together, as shown in Figure 7-5 and Figure 7-6. Note that the top ring was covered with corona dope to improve electrical insulation.

Figure 7-5 The electrostatic air-water droplet separator without housing

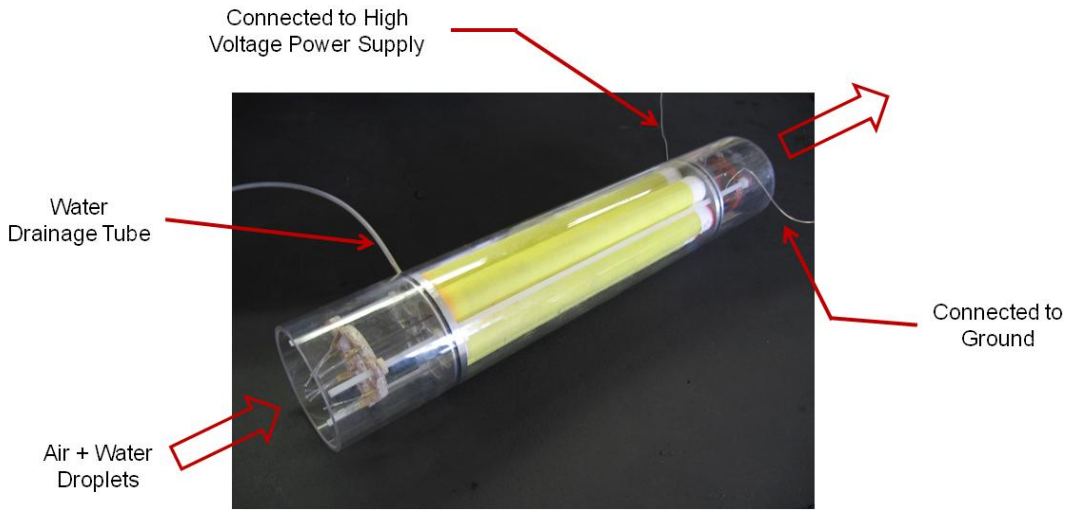

Figure 7-6 The electrostatic air-water droplet separator assembly

7.3. Experimental Setup

The same closed loop setup as in chapter 5 was used in the testing study, refer to section (5.2.2) for more information. Since it was required to test the performance of the separator with different water concentration, few minor medications were done to accommodate the test rig for such requirement. Additional equipments were added o the setup along with the ones already used. These equipments are:

- High pressure head plunger pump, 10 ml/min
- High pressure head plunger pump, 20 ml/min
- Six-jet atomizer (TSI, Inc., 9306)
- Nozzle, 0.1mm orifice diameter (Amfog Nozzle Technologies, Inc.)

First method for droplets generation was the ultrasonic generation. The details of this method were presented in Chapter 5. The second method for droplet generation was the six-jet atomizer (TSI-9306) as shown in Figure 7-10. The specifications for the atomizer are presented in Table 7-1. A nitrogen tank was used

to supply high pressure to the device. The atomizer was connected to the setup through a port just before the separator inlet. The third method used a nozzle with an orifice diameter of 0.1 mm. Two plunge pumps with high pressure heads were used with this nozzle, shown in Figure 7-7. The performance of the separator was tested for each droplets generation method.

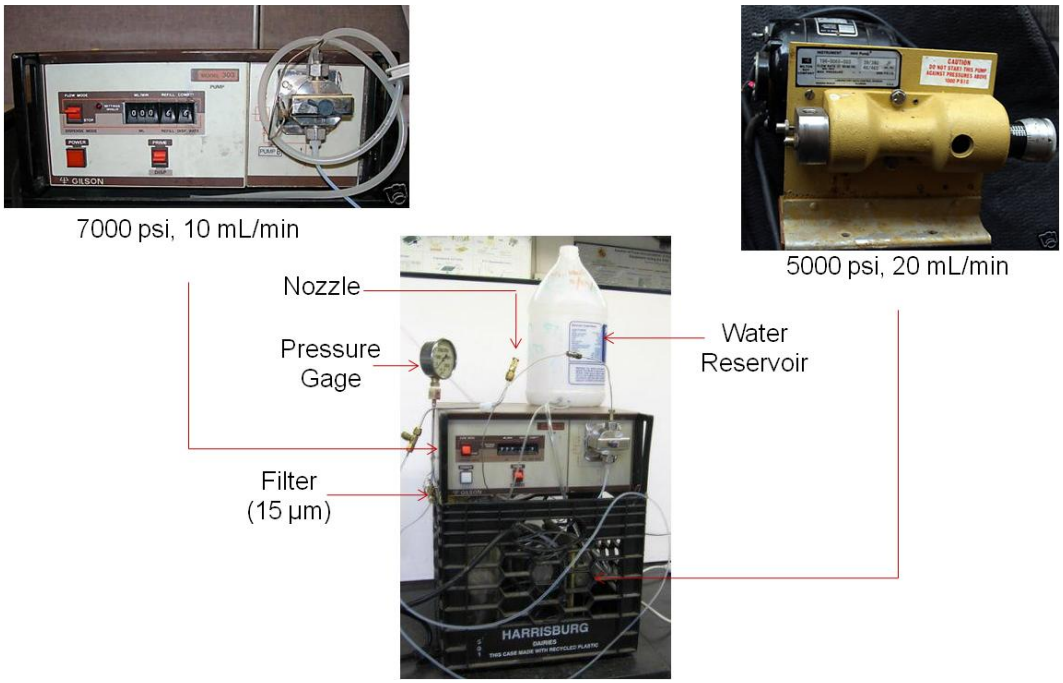

Figure 7-7 Nozzle testing unit

The actual test setup is shown in Figure 7-8, in which the airflow direction is presented by arrows.

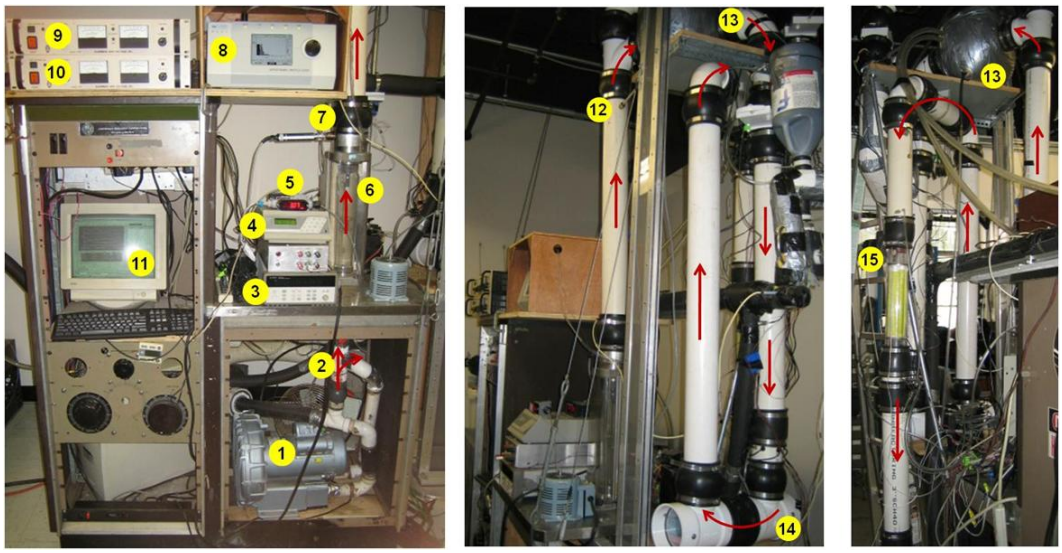

Figure 7-8 Air-water droplet separation test setup, where:

1. Blower	**2. Ball Valves**	**3. DAS Unit**
4. Humidity Sensor Reader	**5. AVT Reader**	**6. Flowmeter**
7. Humidity Sensor Probe	**8. APS Unit**	**9. HV Power Supply (-)**
10. HV Power Supply (+)	**11. Computer**	**12. AVT Probe**
13. HX Vessel	**14. Water Pool**	**15. Electrostatic Separator**

The separator was tested when air flow direction was upward and downward. The goal was to investigate the effect of gravity on the performance. Figure 7-9 shows how the separator was placed during both testing.

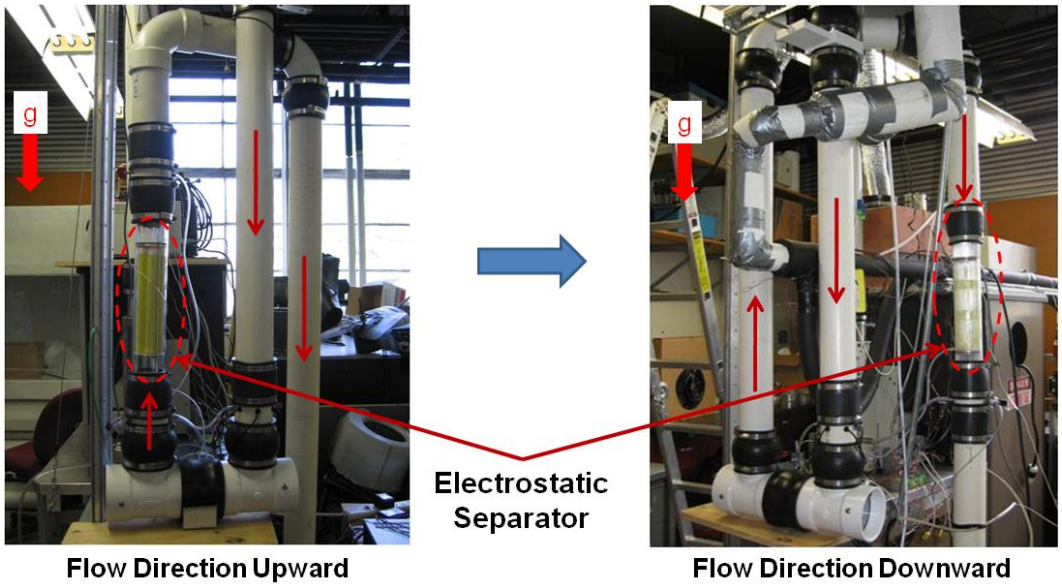

Figure 7-9 Changing flow direction inside the separator

Next part of this section presents the features and operating conditions of the six-jet atomizer that was used as a second method of the production of water droplets.

- **Six-Jet Atomizer (SJA)**

This device was used for one of the three methods adopted in this study to generate water droplets of micron and submicron sizes. The atomizer generates a polydisperse aerosol for different kind of liquids and for different applications. The system has a built-in pressure regulator and pressure gauge, as well as a self-contained dilution system. External controls allow 1-6 particle-generating atomizer jets to be selected, allowing the particle number concentration to be adjusted; see Figure 7-10. Table 7-1 shows the specifications and features of the six-jet atomizer as provided by the vendor (TSI, Inc., 9306).

Figure 7-10 Six-Jet Atomizaer (TSI-9306), adopted from (TSI, Inc. 2009)

Table 7-1 Six-Jet Atomizer (TSI-9306) Specifications and Feaures

Mean droplet diameter for water	0.35 µm
Particle concentration	$> 10^6$ particles/cm^3
Number of jets	6
Maximum inlet pressure	550 k Pa
Maximum outlet pressure	102 k Pa

7.4. Results and Discussion

This part will present the efficiency and performance of the electrostatic separator in removing water droplets from airflow. First, the different methods of water production will be presented.

7.4.1. Generation of Water Droplets

Different sets of tests were conducted to verify the water droplet output in terms of size and concentration from the three different methods used: the ultrasonic generators, the six-jet atomizer, and a nozzle. The aerodynamic particle sizer (APS) is used to measure the droplets concentration. Since it is unfeasible to generate

monodisperse water droplets based on the methods used, then particle weight concentration is used to evaluate the performance of the separator

The results for the measured water droplet concentrations were conducted at the separator inlet. Figure 7-11 presents the droplet concentrations generated by the ultrasonic generators measured at the inlet. The water injection rate, measured by scaling the water reservoir, was 4.5 ml/min. The water concentration measured by the APS for one of the cases was 282 mg/m^3. The big difference between the injected and measured water concentrations was due to the large water droplets produced, which were out of the APS range. The droplets' mean diameter was 3.6 µm.

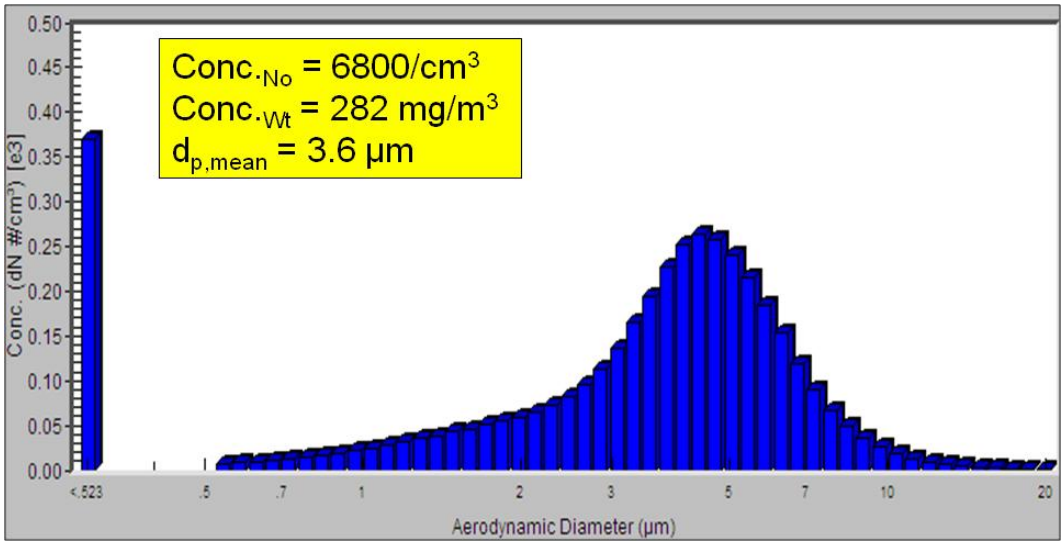

Figure 7-11 Water droplet concentrations generated by ultrasonic generators at the inlet (5 units, $\dot{V}_{air}$= 0.01 m^3/s)

The second method used was the six-jet atomizer. A dry nitrogen tank was used as high-pressure source for the atomizer. The water injection rate was 0.4 ml/min. The weight concentration was 170 mg/m^3, which was smaller than that obtained with ultrasonic generators. The droplets' mean diameter was 3.2 µm, as shown in Figure 7-12.

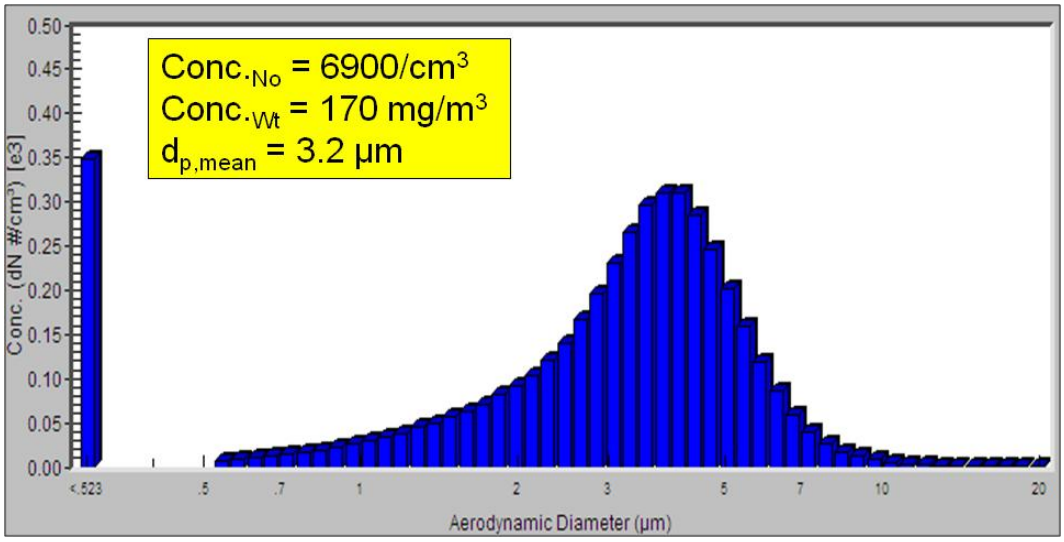

Figure 7-12 Water droplet concentrations generated by six-jet atomizer measure at the inlet (Inlet pressure = 310 kPa, 3 jets, $\dot{V}_{air}$= 0.01 m^3/s)

The last method was the nozzle with an orifice diameter of 0.1 mm. Two water pumps with high head-pressures were used in this testing. The water injection rate was 20 ml/min. When the APS was used to measure the concentration, it did not detect anything. The conclusion reached for the nozzle testing was that it was producing droplets that were too large for the APS range. Therefore, the ultrasonic generation method was used along with the nozzle. The water injected through nozzle provided high water concentration while the ultrasonic generation produced small droplets within the APS range, see Figure 7-13.

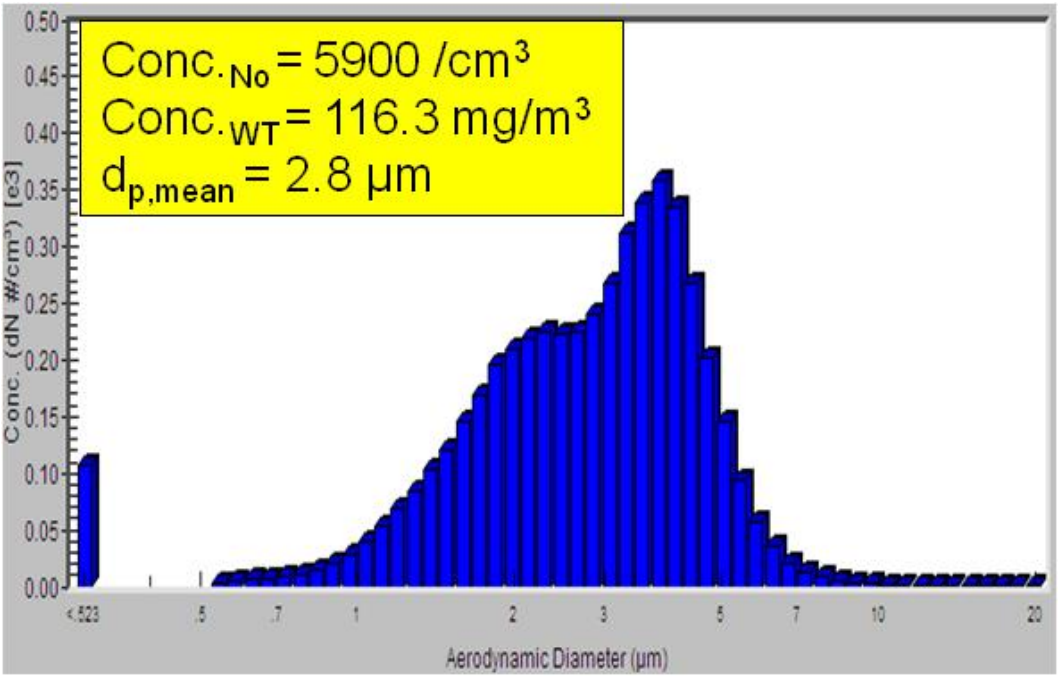

Figure 7-13 Water droplets cenetration generated by nozzle (0.1 mm) and ultrasonic generators measured at the inlet ($\dot{V}_{air}$= 0.01 m^3/s)

The separator performance was checked based on water concentration—low, moderate and high water concentrations. Table 7-2 shows the measured water concentration based on the device used at a fixed airflow rate of 0.01 m^3/s.

Table 7-2 Different Water Concentrations

Concentration Type	Device	Water Injection Rate	Humidity Ratio
Low	Six-Jet Atomizer	0.4 ml/min	0.5 gr water/kg dry air
Moderate	Ultrasonic Generators (5 units)	4.0 ml/min	5.0 gr water/kg dry air
High	Nozzle (0.1 mm)	20 ml/min	27 gr water/kg dry air

For the high water-concentration testing, a combination of the ultrasonic generators and the nozzle was used. As mentioned earlier, the droplets generated by

the nozzle were too big for the APS to measure, and using an additional method that could produce droplets within the APS range would be beneficial to evaluate the separator performance in high water-concentration environments. Therefore, the nozzle was used to provide the high water concentration, and the ultrasonic generators were used to supply the small droplets that could be measured by the APS.

7.4.2. Flow Direction Effect on Separator Performance

The performance of the separator was supposed to be independent of the orientation. However, sparking was initiated between the electrodes during upward flow testing for long time testing. This indicated that the removal of the collected water was not efficient and participated in that sparking. For more details, see section (5.6.3). Therefore, the separator was tested when the flow direction was downward for all cases.

7.4.3. Separation Efficiency

First, the current-voltage characteristics curve (CVC) was plotted for positive and negative polarities for dry air, as shown in Figure 7-14. Since the geometry used was wire-tube, the current was presented as current per unit length. It was mentioned earlier in section (2.1.2) that the CVC could be used to assess the electrostatic separator's performance. So, the higher the value of the corresponding current at fixed voltage, the better the ionization process, which leads to better performance. Therefore, based on results in Figure 7-14, it is expected that the negative polarity electric field can provide better performance compared to the positive polarity field.

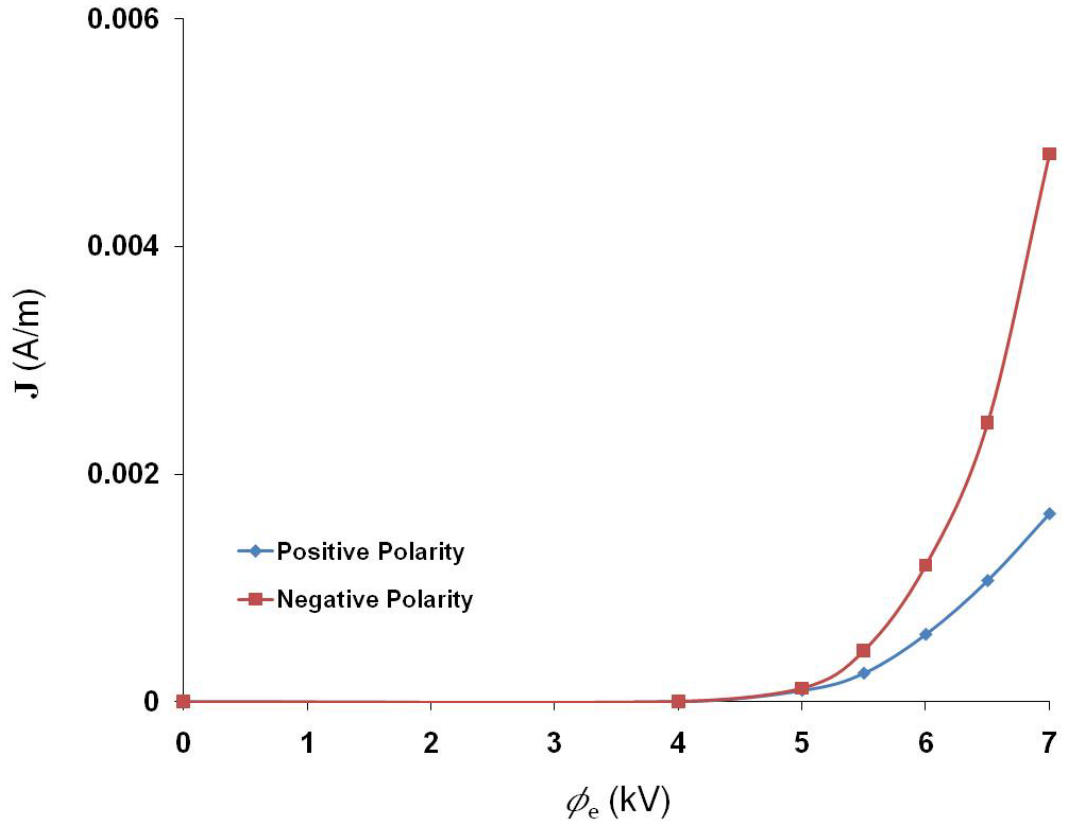

Figure 7-14 Current-voltage characteristics curve where wire length is 250 mm

The efficiency of the separator was evaluated based on two parameters, water concentration and polarity of the emitter electrode. Figure 7-15, Figure 7-16, Figure 7-17 show the water distribution at the outlet with/without applied voltage for low, moderate and high water concentration environments, respectively. The polarity of the emitter was negative.

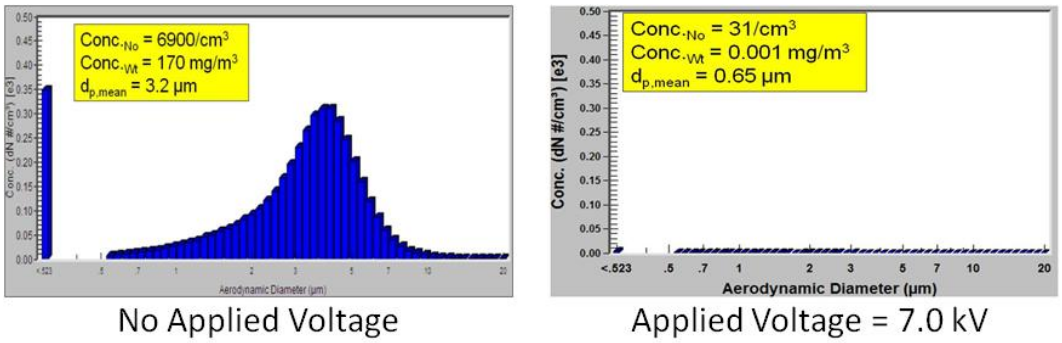

Figure 7-15 Effect of electrostatic separation on water distribution for low water concentration (HR = 0.5 gr water/kg dry air)

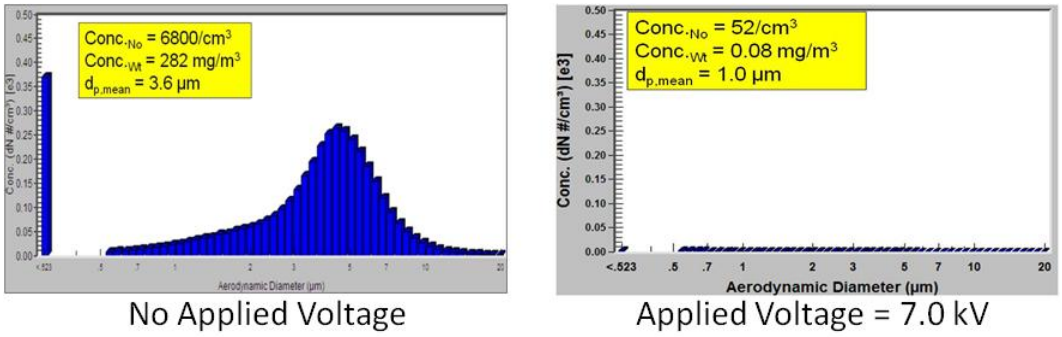

Figure 7-16 Effect of electrostatic separation on water distribution for moderate water concentration (HR = 5.0 gr water/kg dry air)

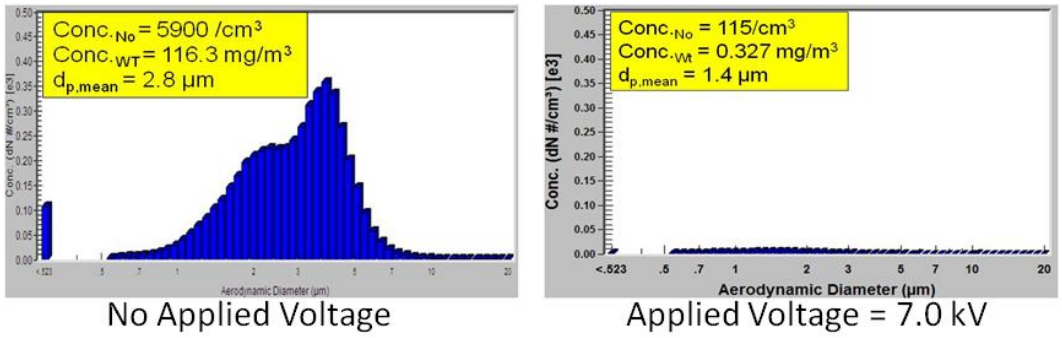

Figure 7-17 Effect of electrostatic separation on water distribution for high water concentration (HR = 27 gr water/kg dry air)

Another way of presenting the results is shown in Figure 7-18. The figure demonstrated the effect of applied voltage on the total weight concentrations of

droplets measured at the separator's outlet for different humidity ratio. The polarity of the emitter was negative.

One should mention that the concentration of water measured by the APS does not correspond accurately to the mass flow rate of injected water to the system. The APS measurements showed much lower droplet weight concentrations, based on Figure 7-18, than the actual injected water concentration. This is due to the APS size range limitation. It can measure droplets between 0.1-20 μm. Any droplet above this is not detected. Therefore, the performance of the APS was evaluated based on the water concentration at the separator outlet. For each case of different water injections, the weight concentration at the outlet was measured starting from no electricity and gradually increasing the applied voltage until the maximum voltage was reached. For all three cases of different water injections, the flow rate of air was kept at a fixed value of 0.01 m^3/s. Figure 7-19 represents the efficiency based on the total number concentration of the droplets.

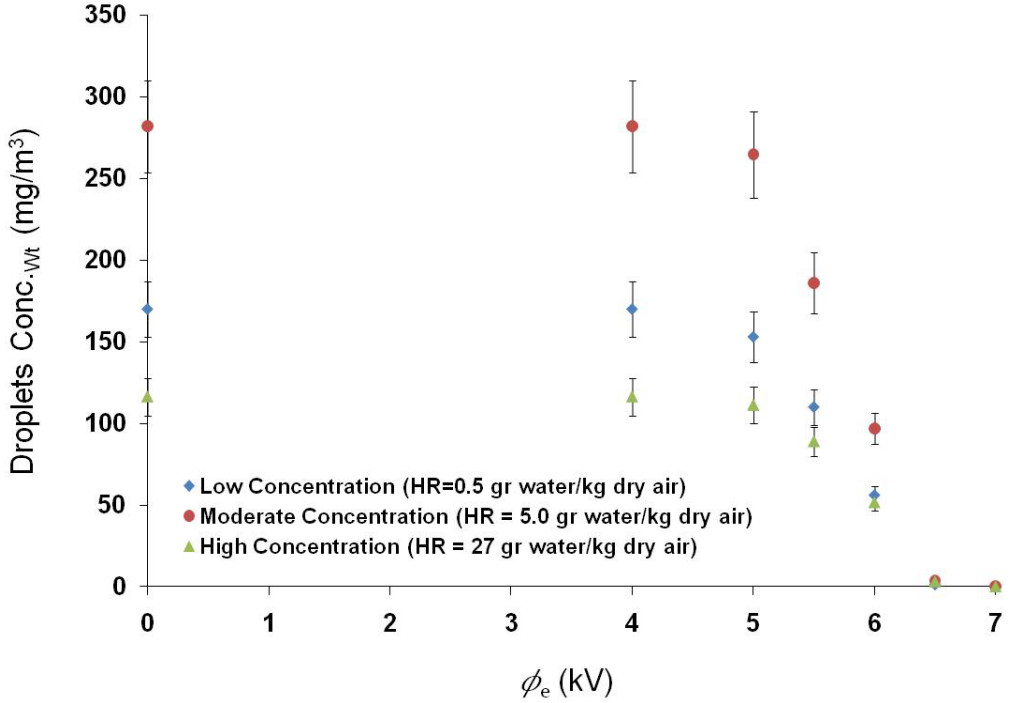

Figure 7-18 Effect of water concentration on separator performance based on total weight of droplets ($\dot{V}_{air}$= 0.01 m^3/s, negative polarity)

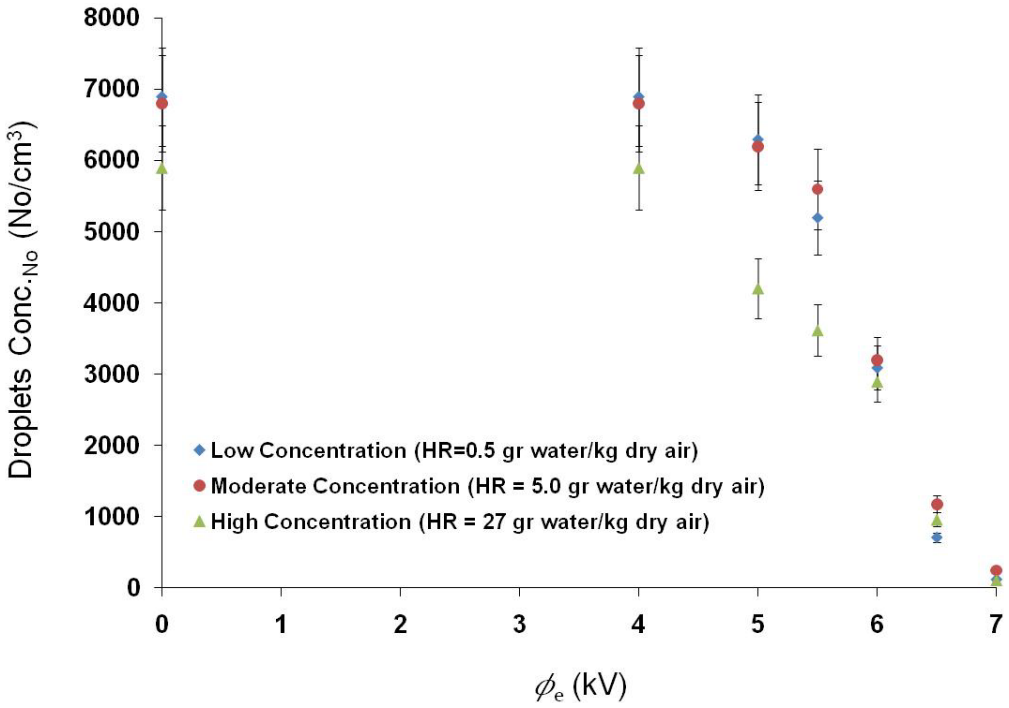

Figure 7-19 Effect of water concentration on separator performance based on total number of droplets ($\dot{V}_{air}$= 0.01 m^3/s, negative polarity)

The total efficiency calculated based on Equation (5-3) showed high separation efficiency attained at a maximum applied voltage of 7.0 kV. At this voltage, the efficiency was 99.99, 99.85 and 99.72% for low, moderate and high water concentrations, respectively.

According to the graph, the measured droplet weight concentration for a humidity ratio of 27 gr water/kg dry air was the lowest. This can be explained by the large droplet size that the nozzle produced. Large droplets lead to a higher possibility of collisions between droplets. Once these large droplets collide with smaller ones produced by the ultrasonic generators, agglomeration occurs between the droplets, creating larger droplets. Since the APS could measure droplets only up to 20 μm, then these droplets were out of the APS range.

Next the study investigated the effect of emitter polarity on the separator performance. Figure 7-20 and Figure 7-21 show a comparison between positive and negative charging for low water concentration (HR = 0.5 gr water/kg dry air). The total weight and number of droplets were plotted for different voltage settings.

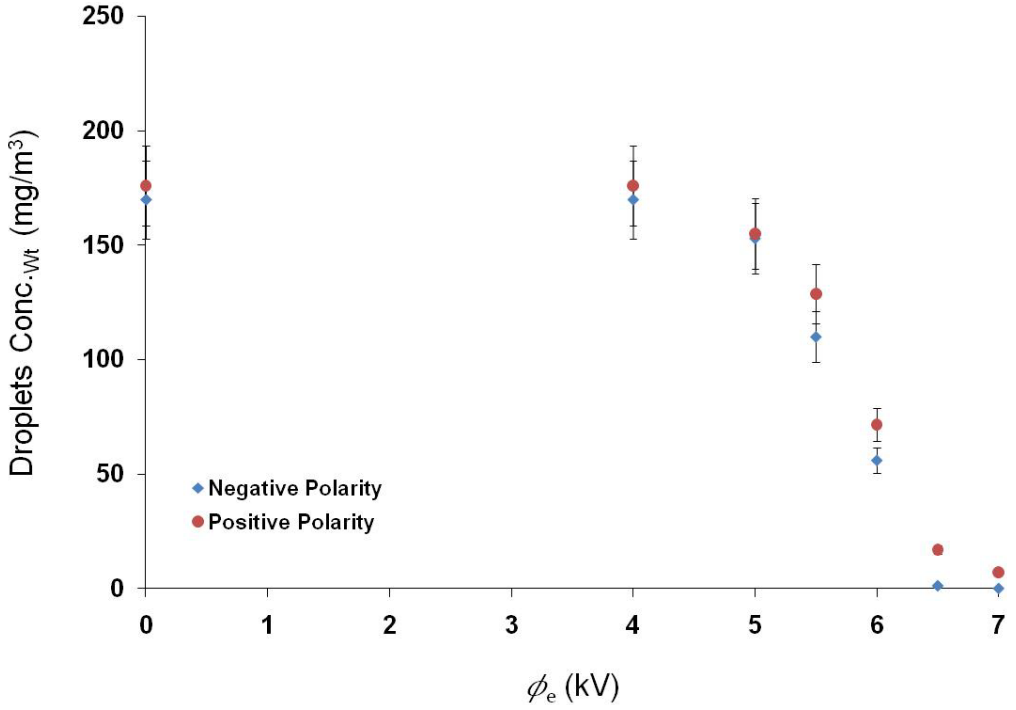

Figure 7-20 Effect of emitter polarity on separator performance based on total weight of droplets ($\dot{V}_{air}$ = 0.01 m^3/s, HR = 0.5 gr water/kg dry air)

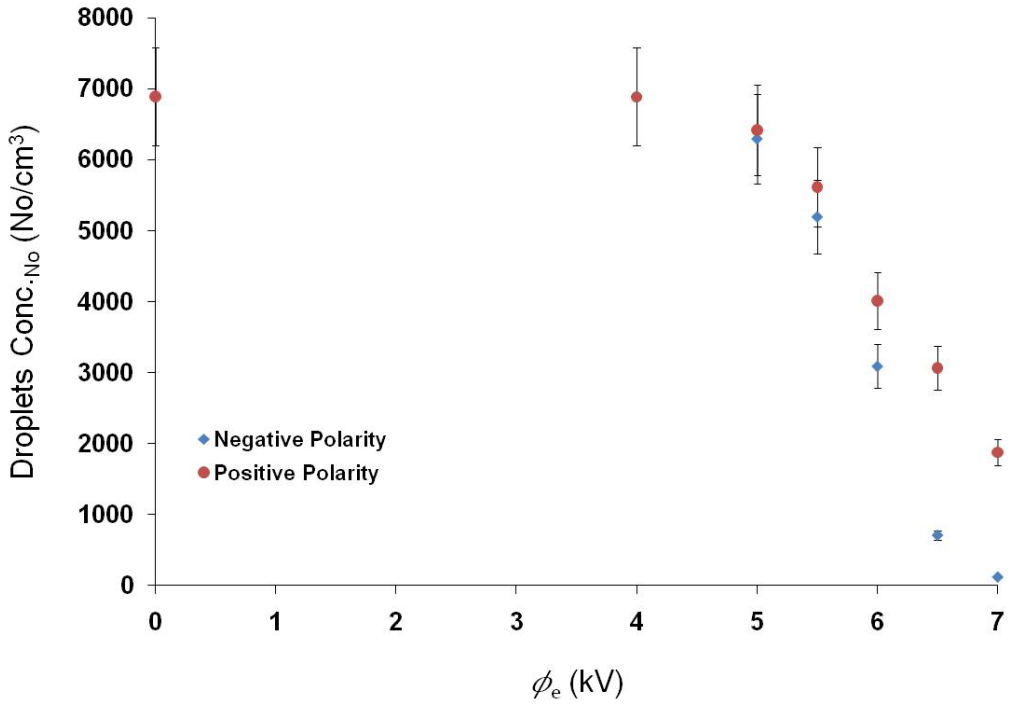

Figure 7-21 Effect of emitter polarity on separator performance based on total number of droplets ($\dot{V}_{air}$= 0.01 m^3/s, HR = 0.5 gr water/kg dry air)

At the maximum voltage, 7.0 kV, the total separation efficiency was 99.99 % and 95.98 % for negative and positive charging, respectively. As mentioned in section (2.1.2.1), negative polarity charging ionized more gas molecules than positive charging. That is the reason why negative charging is preferred over the positive charging in industrial application.

7.4.4. Pressure Drop

The pressure drop across the separator was measured using the differential pressure transducer. The pressure drop due to the secondary motion of ions across the flow in the radial direction was not significant. The total pressure drop measured across the separator was less than 200 Pa at 10 m/s, flow rate of 0.02 m^3/s, (see Figure 7-22).

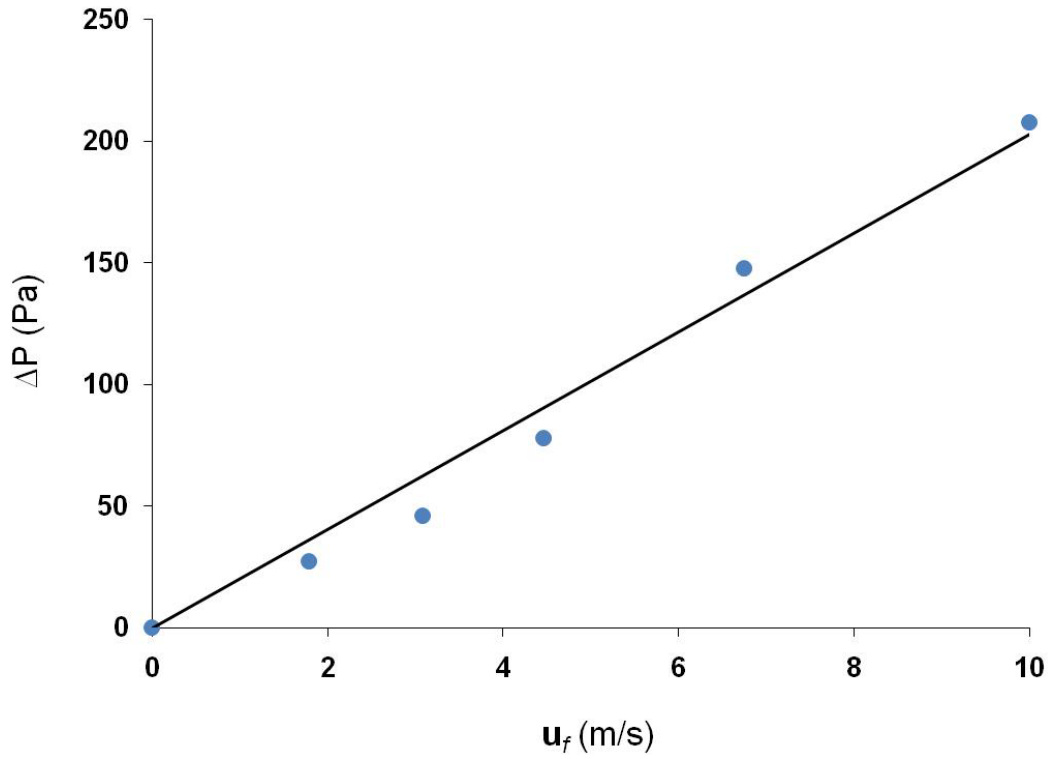

Figure 7-22 Total pressure drop across the electrostatic separator

7.5. Conclusion

The electrostatic separator design, based on wire-tube geometry, performed well in separating water droplets from airflow. The efficiency was near 100% for different water concentrations (HR = 0.5, 5 and 27 gr water/kg dry air) at 7.0 kV for negative charging. The separator performance was highly efficient with positive charging (η = 95.98 % at 7.0 kV), but overall the negative charging attained higher efficiency.

Beside its high performance in separating water droplets from airflow, two other advantages can be added to the electrostatic separator: low power consumption and pressure drop. The maximum output power used was only 9.0 W at 7.0 kV for negative charging. The total pressure drop of the separator is due to two parameters: geometrical design and electrostatic forces. It was verified experimentally that the pressure drop due to the electrostatic forces was not significant and could be neglected. The total pressure drop of the separator was about 200 Pascal at flow velocity of 10 m/s, which is considered very low.

7.6. Summary

This chapter presented the design and manufacturing of a working air-water electrostatic separator prototype. The separator design was based on a wire-tube geometry. A closed test loop was constructed to test the separator performance. The effects of water concentration and emitter polarity were evaluated.

CHAPTER 8: CONCLDING REMARKS AND RECOMMENDED FUTUTRE WORK

8.1. Introduction

This dissertation presented a numerical modeling and three experimental studies on the separation of fine liquid droplets from a gas stream. The field of separation of fine liquid droplets from gas stream has a wide range of applications in HVAC and refrigeration systems, as well as in aerospace applications. Based on a comprehensive literature search, few studies were found in literature highlighting the electrostatic separation of fine liquid droplets. This was due to the measurement complexity of fine droplets and also the behavior of droplets during the electrical charging process (Bürkholz 1989). This chapter summarizes major findings of the present study, while also offers recommendations for future work in this area.

8.2. Concluding Remarks

From an overview of the research conducted in this study the following summary and concluding remarks can be deduced:

- The theoretical fundamentals and definitions of particles charging based on corona discharge were presented along with the relevant equations
- A comprehensive literature survey on the separation of droplets based on conventional methods and electrostatic separation was conducted.
- A user-defined custom code simulating the ionization and charging process of particles in gas flow was developed. It was used in conjunction

with a commercial CFD code Fluent (version 6.2, Lebanon, NH) to track particles and predict the efficiency of electrostatic separation under different electric field and flow conditions.

- A numerical work highlighting a parametric study on the effect of electric field and flow conditions on separation performance was conducted.
- Two test rigs were designed and built to evaluate the effect of electrostatic charging on the separation of droplets. The relevant instruments were also discussed.
- First generation prototype of air-water separator was designed and tested.
- Two different liquids with different relative permittivity values were used as droplets material to investigate the effect of relative permittivity on the separation performance.
- An experimental work highlighting a parametric study of the effect of electric field and flow conditions on separation performance was conducted.
- Experiments were performed by applying DC voltages to the prototypes while particles concentration at inlet and outlet were measured under different electric field and flow conditions.
- A comparison case between numerical modeling results and experimental data was presented. It showed that the numerical modeling results qualitatively showed acceptable agreement with the experimental data in terms of the trend of grade efficiency based on droplets size

- The results demonstrated high dependency of the separation performance on the applied voltage, emitter polarity and flow velocity. However, the effect of flow temperature was found to be insignificant.
- Based on the obtained results through the numerical and experimental approaches, electrostatic separation was shown to be a potential solution for removing of fine droplets from gas stream.
- It was shown through the experimental work of air-water and air-oil separation that electrostatic separation removed droplets from air stream efficiently. For example a high efficiency of 99.999 % was reached in the case of water separation. The droplets diameter was in the range of micron and submicron size. This high efficiency is nearly impossible with conventional separation technologies.
- The experimental results show better separation performance with negative polarity. The droplets weight concentration dropped significantly once ionization starts with negative polarity. A comparison case between the two polarities showed that total efficiency was 78.56 % for negative charging where it was less than 1 % for positive charging at 4.0 kV and flow velocity of 0.9 m/s. Once the applied voltage was increased to 7.0 kV, the total efficiency was 99.999 % and 99.534 % for negative and positive polarities, respectively.
- The study highlighting the effect of relative permittivity showed better performance of water separation than oil separation as expected. However, the oil separation shows also high efficiency even though the relative

permittivity difference is 40 times less in oil. At flow velocity of 5 m/s and negative charging the total efficiency was 96.267 % for oil and 99.999 % for water.

- The pressure drop across the air-water prototype was very low; only 200 Pa was measured at flow velocity of 10 m/s. This can be added as an advantage of electrostatic separation against conventional technologies.
- The maximum power consumption was only 12.0 W at 7.0 kV and 1.25 mA.

8.3. Recommended Future Work

- **Model particles tracking in turbulent flow**

Since turbulent flow regime is widely common in industry, it will be an interesting study to model the tracking of particles in turbulent flow. Fluent CFD code (version 6.2, Lebanon, NH) has two models for particle tracking in turbulent flow, Stochastic and Cloud models. This type of modeling involved many adjustments starting from meshing the geometry mesh building to the selection of the proper tracking model along with its settings. Figure 8-1 presents an example of how model selection would affect the results. Therefore additional work to identify an optimum model will be beneficial.

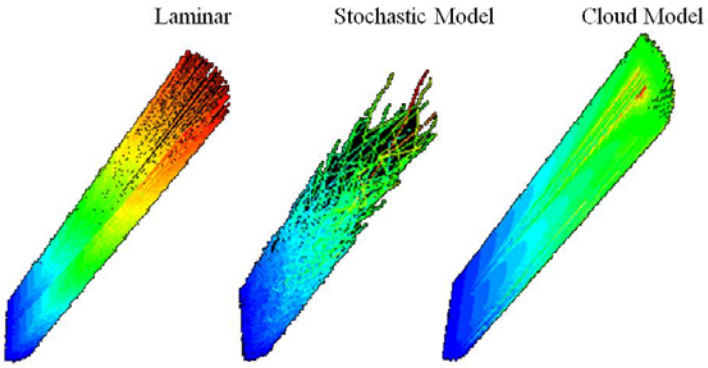

Figure 8-1 Modeling particles tracking in laminar and turbulent flow

- **Model droplets breakup**

As shown in the case of oil droplets separation, droplets were breaking up due to the high surface charge compared to their surface tension. There are a number of numerical works focused in this area. However, the mechanism of break up is far from fully understood.

- **Calculate or predict the free surface charge**

It was highlighted in the literature review that droplets may have some charge before entering the separator which is known as "free surface charge", see section (2.2.3.2). This factor might participate in the difference between experimental and numerical results that were conducted in this study.

- **Use dimensionless numbers to predict the performance**

Dimensionless numbers that were presented in section (2.4.2) can be used for characterizing and analysis of the electrostatic separation phenomenon. An example is presented in Figure 8-2 which shows the dimensionless radial displacement (r*) with the dimensionless resident time of a particles inside the computational domain

(t*). The particle is collected once it reaches the collector surface. In this case particles of size 0.01 and 3.0 µm reach the collector surface indicating their collection. The dimensionless equation can be analyzed to check which terms are more dominant in the charging process. The dominant terms can be selected and studied to evaluate the separation performance.

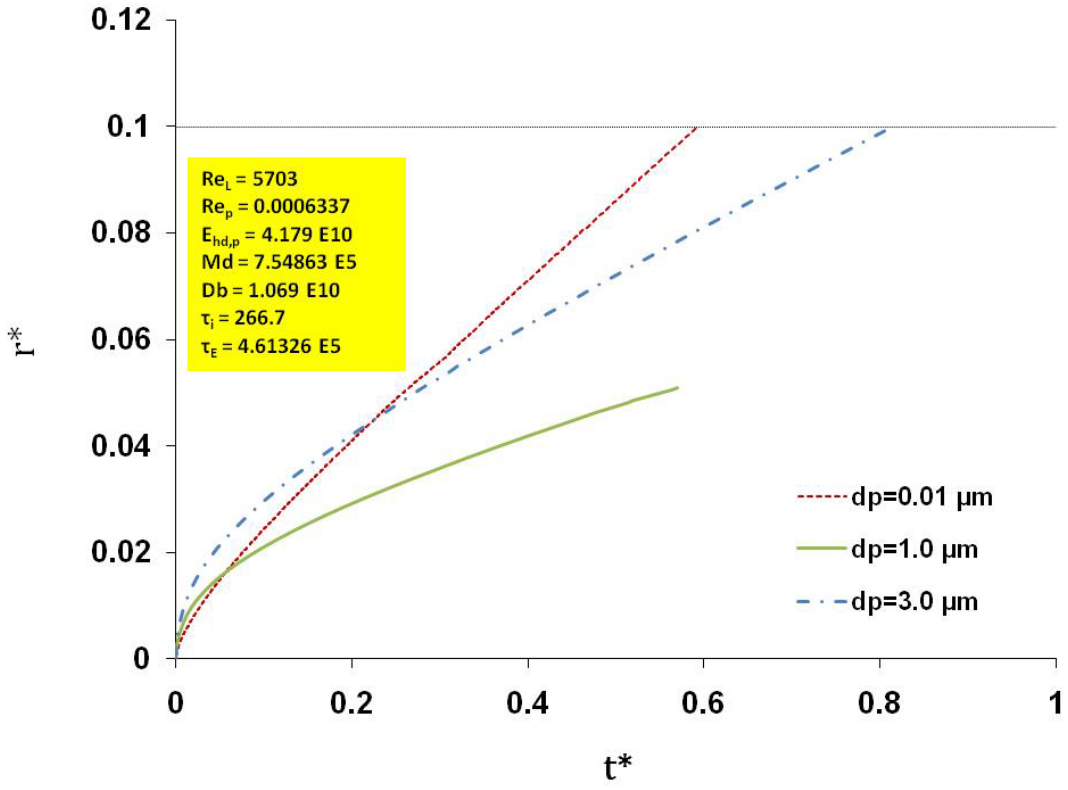

Figure 8-2 Using dimensionless numbers to predict separation performnace

- **Improve the removal and drainage of collected water**

The design should be independent of gravity or flow orientation. Therefore, the removal of collected water is very essential for continuous testing. One of the solutions is to increase the area openings at the collector surface or use a porous surface. In the current design, the open area on the collector surface was about 40% of the total area. In contrast, increasing the openings might also affect the current-

voltage characteristics and lower the ionization performance of the separator. Therefore, a study should be conducted to identify the optimum opening area in the collector surface.

- **Test of different electrode designs**

The presented work covered only wire-tube geometry arrangement. Although the design showed high performance in the separation of droplets, still it has plenty of room for improvement. Testing the design with different electrode geometries can identify an optimum electrode design, thus additional improvement. Some of the designs can be wire-plate or saw-plate.

- **Conduct an optimization study for optimum design**

An optimization study can be conducted to come up with an optimum design. Some of the parameters that can be considered beside the efficiency are the area of collection plates, weight and power consumption. The volume and weight of the design is limited in environmental control systems (ECS), particularly for the aerospace applications.

- **Test different gas-droplets mixture**

As mentioned in literature review section, separation of fine liquid droplets from gas streams is required by many industrial applications. One of the applications is the separation of oil droplets from CO_2 in HVAC and refrigeration industry (Yun, et al. 2007).

REFERENCES

Abbas, M. A., and J. Latham. "'The Instability of Evaporating." *Journal of Fluid Mechanics* 30, no. 4 (1967): 663-670.

Air Cleaninf Equipment, Inc. *Oil Mist and Smoke Applications.* 2007. http://www.aircleaningequipment.com/oilmistsmoke.html (accessed May 2007).

Arendt, P, and H Kallmann. "The Mechanism of Charging Mist Particles." *Z. Phys.* 35 (1926): 421.

ASHRAE. *ASHRAE Handbook, HVAC Systems and Equipments.* Atlanta, GA: American Society of Heating, Refrigerating and Air-Conditioning Engineers, Inc, 2008.

Bologa, An M, H R Paur, H Seifert, and J Handte. "Influence of Particle Concentration on Corona Discharge in CAROLA Collector of Oil Droplets." *Industry Applications Conference, 39th IAS Annual Meeting, IEEE.* 2004. 1572-1576.

Brown, S. C. *Basic Data of Plasma Physics.* New York: Technology Press, M.I.T. and Wiley, 1959.

Bürkholz, A. *Droplet Separation.* Weinheim: VCH Verlagsgesellschaft, 1989.

Calvert, S. "Guidelines for Selecting Mist Eliminators." *Chem. Eng.* 85, no. 5 (1978): 109-112.

Chang, J., et al. "On-Set of EHD Turbulence for Cylinder in Cross flow Under Corona Discharges." *Journal of Electrostatics* 64, no. 7-9 (July 2006): 569-573.

Chen, J., and J. Davidson. "Ozone Production in the Negative DC Corona: The Dependence of Discharge Polarity." *Plasma Chem. and Plasma Process.* 23, no. 1 (2003): 83-102.

Cottrell, Frederick G. "The Electrical Precipitation of Suspended Particles." *The Journal of Industrial and Engineering Chemistry* 8, no. 3 (1911): 542-550.

Davis, E. J., and M. A. Bridges. "The Rayleigh Limit Charge revisited: light Scattering from Exploding Droplets." *Journal of Aerosol Science* 25, no. 6 (1994): 1179-1199.

De Juan, L., and J. Fernandez De La Mora. "Charge and Size Distributions of Electrospray Drops." *J. Colloid Interface Sci.* 186, no. 2 (1997): 280-293.

Deutsch, W. "Bewegung und Ladung der Elektricitatstrager im Zylinder Kondensator." *Annalen der Physik* 68 (1922): 335.

Doyle, A., D. R. Moffett, and B. Vonnegut. "Behavior of Evaporating Electrically Charged Droplets." *Journal of Colloid Science* 19 (1964): 136-143.

Dwyer, Inc. 2009. http://www.dwyer-inst.com/ (accessed 2009).

Feng, J Q. "An Analysis of Corona Currents Between Two Concentric Cylindrical Electrodes." *Journal of Electrostatics* 4 (1999): 37-48.

Gaugain, J. M. "On the Disrurptive Discharge." *Ann. chim. et phys.* 64 (1862): 175.

Gomez, A., and K. Tang. "Charge and Fission of Droplets in Electrostatic Sprays." *Physics of Fluids* 6 (1994): 404-414.

Goo, Jae Hark, and Jin Won Lee. "Stochastic Simulation of Particle Charging and Collection Characteristics for a Wire-Plate Electrostatic Precipitator of Short Length." *Journal of Aerosol Science* 28, no. 5 (July 1997): 875-893.

Hairston, P., F. Dorman, G. Sem, and J. Agarwal. Apparatus for Measuring Particle Sizes and Velocities. U.S.A./Minnesota Patent 5,561,515. October 1, 1996.

Heidenreich, S., and F. Ebert. "Condensational Droplet Growth as a Preconditioning Technique for the Separation of Submicron Particles from Gases." *Chemical Engineering and Processing* 34 (1995): 235-244.

Hinds, W C. *Aerosol Technology: Properties, Behavior and Measurement of Airborne Particles.* Los Angeles, California: John Willy & sons Inc, 1999.

Hohlfeld, M. "Das Niederschlagen des Rauches durch elektricitat." *Archiv. fur die gesammte Naturlehre* 2 (1824): 205.

IEEE-DEIS-EHD Technical Committee. "Recommended International Standard for Dimensionless Parameters Used in Electrohydrodynamics." *IEEE Transactions on Dielectrics & Electrical Insulation* 10, no. 1 (2003): 3-6.

Key, M. "http://www.redicontrols.com/pdf_files/news_OAM-RSESJournalColorArticle.pdf." November 2002. (accessed August 1, 2008).

Kihm, K D. "Effects of Nonuniformities on Particle Transport in Electrostatic Precipitators." Ph.D. thesis, Standford University, Stanford, 1987.

Lei, Hong, Lian-Ze Wang, and Zi-Niu Wu. "EHD Turbulent Flow and Monte-Carlo Simulation for Particle Charging and Tracing in a Wire-Plate Electrostatic Precipitator." *Journal of Electrostatics* 66, no. 3-4 (March 2008): 130-141.

Liu, Benjamin Y. H., and Hsu-Chi Yeh. "On the Theory of Charging of Aerosol Particles in an Electric Field." *Journal of Applied Physics* 39, no. 3 (1968): 1396.

Loeb, L. B., and J. M. Meek. *The Mechanism of the Electric Spark.* Stanford Univ. Press, 1941.

Loeb, Leonard B. *Electrical Coronas: Their Basic Physical Mechanisms.* First Edition. University of California Press., 1965.

Macky, W. A. "Some Investigations on the Deformation and Breaking of Water Drops in Strong Electric Fields." *Proceedings of the Royal Society of London* 133, no. 822 (1931): 565-587.

Millikan, R. A. *Electrons (+ and -), Protons, Photons, Neutrons, Mesotrons and Cosmic Rays.* First edition. Cambridge University, 1935.

Morsi, S A, and A J Alexander. "An Investigation of Particle Trajectories in Two-Phase Flow Systems." *Journal of Fluid Mechanics* 55, no. 2 (September 1972): 193-208.

Nahrwold, R. "Electricity in Air." *Ann. phys.* 5 (1878): 460.

Ohadi, M M, S S Li, J M Webber, S W Kim, and R L Whipple. "Humidity, Temperature and Pressure Effects in an Electrostatically Enhanced Heat Exchanger." *Scientia Iranica* 1, no. 1 (1994): 97-110.

Parker, K R. *Applied Electrostatic Precipitation.* London: Chapman & Hall, 1997.

Pauthenier, M M, and M Moreau-Hanot. "La Charge des Particulates Spheriques Dans un Champ Ionise." *Journal de Physique et le Radium* 3 (1932): 590.

Peek, F W. *Dielectric Phenomena in High Voltage Engineering.* McGraw-Hill, 1929.

Qunis, H, G Ahmadi, and J B McLaughlin. "Bownian Diffusion of Submicrometer Particles in the Viscous Sublayer." *Journal of Colloid and Interface Science* 143, no. 1 (1991): 266-277.

Rayleigh, J. W. "On the Equilibrium of Liquid Conducting Masses Charged with Electricity." *Phil. Mag.* 5, no. 14 (1882): 184-186.

Richardson, C. B., A. L. Pigg, and R. L. Hightower. "On the Stability Limit of Charged Droplets." *Proc. R. Soc. A* 422 (1989): 319-328.

Riehle, C. "Bewegung und Abscheidung von Partikeln im Elektrofilter." Doctorate Thesis, University of Karlsruhe, 1929.

Rohmann, H. "Messung der Grosse von Schwebeteilchen." *Z. Phys.* 17 (1923): 253.

Scharge, D S, J M Shoemaker, and J McQuillen. "Passive Two-Phase Fluid Separation." *AIAA 36th Aerospace Sciences Meeting & Exhibit. AIAA-98-0731.* Reno, 1998.

Scheeline, A., and M. Zoellner. "Thomson Scattering as a Diagnostic of Atmospheric Pressure Discharge." *Society for Applied Spectroscopy* 38, no. 2 (1984): 245-258.

Schweizer, J. W., and D. N. Hanson. "Stability Limit of Charged Drops ." *J. of Colloid Interface Science* 35 (1971): 417-423.

Shoushtari, A. "Experimental and Computational Analysis of an Electrohydrodynamic Mesopump for Spot Cooling applications." PhD Thesis, 2004.

Shrimpton, J. S. "Dielectric Charged Drop Break-up at Sub-Rayleigh Limit Conditions." *IEEE Transactions on Dielectrics and Electrical Insulation* 12, no. 3 (2005): 573-578.

Soldati, Alfredo. "Cost-Efficiency Analysis of a Model Wire-Plate Electrostatic Precipitator via DNS Based Eulerian Particle Transport Approach." *Aerosol Science and Technology* 37, no. 2 (Febreuary 2003): 171-182.

Sugita, H, T Nakazawa, L Jiao-Long, and X Tao. "Study on the Behavior of Droplet in Air-Water Separator." *Journal of the Japan Institution of Marine Engineering* 38, no. 2 (2003): 72-80.

Taflin, D. C., T. L. Ward, and E. J. Davis. "Electrified Droplet Fission and the Rayleigh Limit." *Langmuir* 5, no. 2 (1989): 376-384.

Talaie, M R. "Mathematical Modeling of Wire-Duct Single-Stage Electrostatic Precipitators." *Journal of Hazardous Materials* 124, no. 1-3 (September 2005): 44-52.

Talaie, M R, J Fathikaljahi, M Taheri, and P Bahri. "Mathematical Modeling of Double-Stage Electrostatic Precipitators Based on a Modified Eulerian Approach." *Aerosol Science and Technology* 34, no. 6 (June 2001): 512-519.

Taylor, Geoffrey. "Disintegration of Water Drops in an Electric Field." *Proceedings of the Royal Society of London* 280, no. 1382 (1964): 383-397.

TeGrotenhuis, W, and V Stenkamp. "Normal Gravity Testing of a Microchannel Phase Separator for In-situ Resource Utilization." Battelle Memorial Institute, Richland, 2001.

Temprite, Inc. *http://www.temprite.com/downloads/oilCarryOverandSludge.pdf.* 2007. (accessed May 20, 2007).

Tomimatsu, K. "Advanced Gas Cleaning System." *Proc. Institute of Electrostatics*, 1999: 55-58.

Townsend, J. S. "On ionization produced by the motion of positive and negative ions ." *Philosophical Magazine* 6, no. 33 (1903): 358-361.

TSI, Inc. *www.TSI.com.* 2009. http://www.tsi.com/uploadedFiles/Product_Information/Literature/Spec_Sheets/3321.pdf (accessed 2009).

White, H J. *Industrial Electrostatic Precipitation.* Portland, Oregon: Addison-Wesley Publishing Company Inc, 1963.

Wikipedia. *Wikipedia, The Free Encyclopedia.* 2008. http://en.wikipedia.org/wiki/Electrohydrodynamic (accessed March 2008).

Wilson, C. T. R., and G. I. Taylor. "The Bursting of Soap-Bubbles in a Uniform Electric Field." *Proc. Cambridge Philos. Soc.* 22 (1925): 728.

Xu, D., et al. "Discharge Characteristics and Applications for Electrostatic Precipitation of Direct Current: Corona with Spraying Discharge Electrodes." *Journal of Electrostatics* 57 (2003): 217-224.

Yun, Rin, Yunho Hwang, and Reinhard Radermacher. "Convective gas cooling heat transfer and pressure drop characteristics of supercritical CO2/oil mixture in a minichannel tube." *International Journal of Heat Transfer* 50, no. 23-24 (November 2007): 4796-4804.

Zeleny, J. "Instability of Electrified Liquid Surfaces." *Phys. Rev.* 10 (1917): 1-16.

Zeleny, J. "On Discharges from Points in Gases, with Special Regard to So-Called Dark Discharges." *Phys. Rev.* 24 (1924): 255-271.